Quasar Outflows: Their Scale, Behavior and Influence in the Host Galaxy

Carter W. Chamberlain

Dissertation submitted to the Faculty of the
Virginia Polytechnic Institute and State University
in partial fulfillment of the requirements for the degree of

Doctor of Philosophy
in
Physics

Nahum Arav, Chair
John Simonetti
Duncan Farrah
Eric Sharpe

March 23, 2016
Blacksburg, Virginia

Keywords: Observational Astrophysics, Quasar Outflows, AGN Feedback

Quasar Outflows: Their Scale, Behavior and Influence in the Host Galaxy

Carter W. Chamberlain

(ABSTRACT)

Quasar outflows are a major candidate for Active Galactic Nuclei (AGN) feedback, and their capacity to influence the evolution of their host galaxy depends on the mass-flow rate ($\dot{M}$) and kinetic luminosity ($\dot{E}_{\rm k}$) of the outflowing material. Both quantities require measurement of the distance (R) to the outflow from the central source as well as physical conditions of the outflow, which can be determined using spectral observations of the quasar. This thesis presents spectral analyses leading to measurements of R, $\dot{M}$ and $\dot{E}_{\rm k}$ for three different quasar outflows.

Analysis of LBQS J1206+1052 revealed multiple diagnostic spectral features that could each be used to independently determine R. These diagnostics yielded measurements that were in close agreement, resulting in a robust outflow distance of 840 pc from the central source. This measurement is much larger than predicted from radiative acceleration models ($\sim 0.01-0.1$ pc), suggesting that outflows appear much farther from the central source than is generally assumed.

The outflow in SDSS J0831+0354 was found to carry a kinetic luminosity of $10^{45.7}$erg s^{-1}, which corresponds to 5.2 per cent of the Eddington luminosity of the quasar. This outflow

is one of the most energetic outflows to date and satisfies the criteria required to produce AGN feedback effects.

A variability study of NGC 5548 revealed an obscuring cloud of gas that shielded the outflow components, dramatically lowering their ionization state. This resulted in the appearance of absorption from the rare element Phosphorus, as well as from sparsely-populated energy levels of C III and Si III. These spectral features allowed for an accurate determination of R and for constraints on the ionization phase to be obtained. The latter constraints were used to develop a self-consistent model that explained the variability of all six outflow components during five observing epochs spanning 16 years.

Attribution

This thesis is comprised of three published papers for which I am either the first- or second-author.

Chapter 2 previously appeared as: Chamberlain C., Arav N., 2015, MNRAS, 454, 675

Chapter 3 previously appeared as: Chamberlain C., Arav N., Benn C., 2015, MNRAS, 450, 1085

Chapter 4 previously appeared as: Arav N., Chamberlain C., Kriss G. A., Kaastra J. S., Cappi M., Mehdipour M., Petrucci P.-O., Steenbrugge K. C., Behar E., Bianchi S., Boissay R., Branduardi-Raymont G., Costantini E., Ely J. C., Ebrero J., Di Gesu L., Harrison F. A., Kaspi S., Malzac J., De Marco B., Matt G., Nandra K. P., Paltani S., Peterson B. M., Pinto C., Ponti G., Pozo Nuñez F., De Rosa A., Seta H., Ursini F., De Vries C. P., Walton D. J., Whewell M., 2015, A&A, 577, A37

Contents

List of Figures

List of Tables

Chapter 1

Introduction

It is generally assumed that a supermassive black hole (SMBH) resides in the center of every galaxy. Material from the host galaxy falls into an accretion disc surrounding the SMBH, and due to the highly relativistic nature of such an object, approximately 10 per cent of the rest mass of the inflowing material is radiated away as energy. This phenomenon, when active, can be over 100 times more luminous than all the stars in the host galaxy combined. The source of this intense radiation is referred to as an active galactic nucleus (AGN).

Energy released from the AGN must travel through the host galaxy before escaping and can transfer energy and momentum to the surrounding material along the way. This process, called AGN feedback, has important applications in the context of cosmology as the enormous power of the AGN could potentially influence the evolution of the host galaxy. For example, AGN feedback could cause heating of cold gas clouds throughout the galaxy, preventing gravitational collapse the clouds and effectively halting star formation. AGN feedback could also halt the accretion of new material onto the AGN itself, choking off the fuel source thereby throttling the growth rate of the SMBH. The extreme instance of this case occurs during the aptly-named "blowout" stage of galaxy merging, wherein the AGN unbinds much of the surrounding gas from the galaxy, which then begins to fade into a red elliptical galaxy. Even beyond the boundaries of the galaxy, AGN are supposed to cause chemical enrichment

of the intergalactic medium (IGM) and to play a role at even farther scales by impeding cooling flows in the intracluster medium (ICM).

Although this mechanism is used frequently, the dominant agent that carries energy and momentum into the surrounding environment is still debated. Radiation-driven winds are the simplest type of outflow and would seem a logical choice since the AGN is very luminous across the entire spectrum. However, photons couple very poorly to baryonic matter, and are relatively inefficient at transferring momentum to the host galaxy.

Poloidal jets of highly relativistic gas emitted from the AGN certainly transmit a large amount of energy, but the narrow opening angle of this collimated beam limits the volume of surrounding gas with which the jet can interact. Furthermore, a jet would not affect the galaxy bulge isotropically, contrary to observations, unless the jets change direction in a non-standard way (i.e. precession of the jet would still only affect an annulus of the bulge).

The most plausible candidate for AGN feedback are broad absorption line (BAL) outflows, which are detected as blueshifted (in the quasar rest-frame) absorption troughs in 20-40 per cent of quasars. These ubiquitous outflows are presumed (from their detection rate) to cover $\sim$20-40 per cent of the solid angle around the quasar. Such a wide opening angle allows for efficient interaction with the surrounding environment. This is the type of outflow that will be studied in this thesis.

Simulations utilizing AGN feedback have shown that an outflow has the capability of producing the aforementioned feedback effects if its kinetic luminosity $\dot{E}_{\rm k}$ is at least 0.5 per cent to 5 per cent of the Eddington luminosity $L_{\rm Edd}$ of the quasar. The kinetic luminosity, defined as the kinetic energy of the gas divided by the dynamical time of the outflow, is dependent on several properties of the outflow such as velocity, density and distance R to the outflow from the central source. The calculation of $\dot{E}_{\rm k}$ and its dependent measurements will be thoroughly investigated in this thesis; here simply note that $\dot{E}_{\rm k}$ requires a measurement of R. Distances in many fields of astronomy are notoriously difficult to measure, often requiring intricate and indirect approaches (e.g. "standard candles" for cosmological distances, parallax for local

stars). Outflow distances are likewise challenging yet necessary measurements to obtain, and several methods have been employed to do so.

The simplest way to measure the size of an outflow would be to directly image it. However, the AGN of even nearby galaxies are too compact to be spatially resolved using modern telescopes. Such a method can only be utilized for outflows that are far away from the central source and have thus become disconnected from the AGN.

Scientific study of these outflows is therefore performed using spectral observations within the line-of-sight to the AGN. This sightline is masked by any outflowing gas moving directly towards the observer, resulting in absorption features in the observed spectrum.

Quasars are known to be highly variable, and in some cases, if the outflow is observed repeatedly, the absorption features can change in depth over multiple observing epochs. This variability can be interpreted as an outflow moving across the line-of-sight, resulting in a partial eclipse as the outflow transits the emission source. By assuming a certain size of the emission source, one can estimate the angular distance traveled during the time period between two observations, leading to a value for the angular velocity of the outflow. Further assuming that the outflow is in Keplerian motion and follows a perfectly circular orbit, another simple calculation yields the radius of the orbit (i.e. R). This thesis presents an alternative interpretation of trough variability which results from changes in the ionization structure of the outflowing gas, instead of transverse motion across the line-of-sight.

Even if the absorption features do not vary, or if observations are made only during a single epoch, R can still be indirectly determined provided that certain diagnostic absorption lines (i.e. from excited states) are present in the spectrum. This method is the main technique used throughout this thesis and will be thoroughly explained therein.

This thesis is composed of three manuscripts, each presenting the analysis for a different quasar. Chapter 2 details the analysis of the outflow from LBQS J1206+1052. This analysis found a reliable measurement for the location of the outflow and demonstrates the robustness of the same methods used in subsequent chapters. Chapter 3 studies the outflow from SDSS

J0831+0354. This study resulted in one of the most energetic outflows measured to date. Chapter 4 explains the latest research on the outflows from NGC 5548. This famous object exhibited substantial variability in both the emission source and the outflow, allowing the dynamics of the system to be thoroughly studied. Chapter 5 concludes the thesis with a revision of the general assumptions regarding quasar outflows.

Chapter 2

Large Scale Outflow in Quasar LBQS J1206+1052: HST/COS Observations

2.1 Abstract

Using two orbits of HST/COS archival observations, we measure the location and energetics of a quasar outflow from LBQS J1206+1052. From separate collisional excitation models of observed N III/N III* and Si II/Si II* troughs, we measure the electron number density n_e of the outflow. Both independent determinations are in full agreement and yield $n_e = 10^{3.0}$ cm^{-3}. Combining this value of n_e with photoionization simulations, we determine that the outflow is located 840 pc from the central source. The outflow has a velocity of 1400 km s^{-1}, a mass flux of $9M_\odot$ yr^{-1} and a kinetic luminosity of $10^{42.8}$ erg s^{-1}. The distance finding is much larger than predicted from radiative acceleration models, but is consistent with recent empirical distance determinations.

2.2 Introduction

Quasar outflows are detected in $\sim 60\%$ of quasar spectra as absorption troughs that are blueshifted in the rest-frame of the quasar (Hewett & Foltz, 2003; Ganguly & Brotherton, 2008; Knigge et al., 2008; Dai, Shankar & Sivakoff, 2008). These outflows are often invoked as agents for Active Galactic Nuclei (AGN) feedback, which requires the outflowing gas to have a kinetic luminosity between 0.5 (Hopkins & Elvis, 2010) and 5 (Scannapieco & Oh, 2004) per cent of the Eddington luminosity ($L_{\rm Edd}$) of the quasar. A crucial parameter needed to calculate this kinetic luminosity is the distance R to the outflow from the central source, which can be inferred from excited-state absorption combined with photoionization modeling (e.g. Korista et al., 2008).

Our group (de Kool et al., 2001, 2002b,a; Moe et al., 2009; Bautista et al., 2010; Dunn et al., 2010; Arav et al., 2012; Borguet et al., 2012b,a, 2013; Edmonds et al., 2011; Arav et al., 2013; Chamberlain, Arav & Benn, 2015; Arav et al., 2015) and others (Hamann et al., 2001; Gabel et al., 2005b; Aoki et al., 2011; Lucy et al., 2014) have determined R for ~ 20 quasar outflows using excited-state troughs. This method requires absorption troughs from at least two energy levels of the same ion, usually the ground state and one excited state. Several investigations (Hamann et al., 2001; de Kool et al., 2001, 2002b,a; Korista et al., 2008; Moe et al., 2009; Dunn et al., 2010; Aoki et al., 2011) used excited-state diagnostics from singly-ionized ions. Outflows exhibiting absorption from exclusively singly-ionized species are a minority (20% of BALQSOs, Dai, Shankar & Sivakoff, 2012); the majority of outflows show absorption from only higher-ionization ions. This difference in the frequency of detection between singly- and multiply-ionized absorption troughs motivated our S IV/S IV* surveys (Dunn et al., 2012; Borguet et al., 2012a, 2013; Chamberlain, Arav & Benn, 2015) that measured several energetic outflows using excited-state absorption from the triply-ionized ion S IV. Arav et al. (2013) measured the energetics of HE 0238-1904 using excited states of triply-ionized O IV/O IV*, and Arav et al. (2015) obtained distance diagnostics for NGC 5548 using excited states from two doubly-ionized ions (C III and Si III). In this paper, we

present a similar application of the excited-state method to an outflow showing absorption from two doubly-ionized ions (N III and Si II).

The plan of this paper is as follows. In Section 2.3, we present the HST/COS observations of LBQS J1206+1052, identify the absorption features of the outflow and measure the ionic column densities from their respective troughs. We perform a photoionization analysis in Section 2.4.1 and 2.4.2 and we constrain the metallicity of the gas in Section 2.4.3. In Section 2.4.4 we derive the electron number density n_e of the outflow via collisional excitation modeling. The distance and energetics are calculated in Section 2.4.5 and we discuss the robustness of the measurements in Section 2.5. We summarize our results in Section 2.6.

2.3 Observations and spectral fitting

LBQS J1206+1052 (J2000: RA=12 09 24.079, DEC=+10 36 12.06, z=0.395549) was observed with HST/COS in May 2010 as part of Proposal ID 11698 (PI Putman) for an exposure time of 4840 s using the G130M grating. The reduced data was downloaded from the Mikulski Archive for Space Telescopes (MAST) and the four exposures were co-added to produce the final extracted one-dimensional spectra shown in Figure 2.3. A gap between the CCD chips occurs at $\lambda_{obs} \sim 1295$Å while geocoronal emission from O I* appears at $\lambda_{obs} \sim 1305$Å. The SDSS spectrum observed in March 2003 will be discussed in Section 2.3.6.

2.3.1 Spectral fitting

Absorption troughs associated with H I, C III, N III, O III, O VI, Si II and S VI ionic species are identified in Figure 2.3. The kinematic structure of the absorption is similar among the different ions, allowing us to use the template-fitting technique commonly used in BAL quasar studies (e.g. Arav et al., 1999b; de Kool, Korista & Arav, 2002; Moe et al., 2009; Borguet et al., 2012a, and references therein) to analyze absorption that is self-blended

Figure 2.1: Portion of the COS G130M data of LBQS J1206+1052. Absorption troughs associated with the quasar outflow are shown in blue for resonance transitions and in red for excited transitions. Transitions from the Lyman series (in the outflow rest-frame) are shown as green vertical lines. The unabsorbed emission model (see Section 2.3.2) is shown as a solid red line. A gap between the CCD chips occurs at $\lambda_{\rm obs} \sim 1295$Å while geocoronal emission from O I* appears at $\lambda_{\rm obs} \sim 1305$Å.

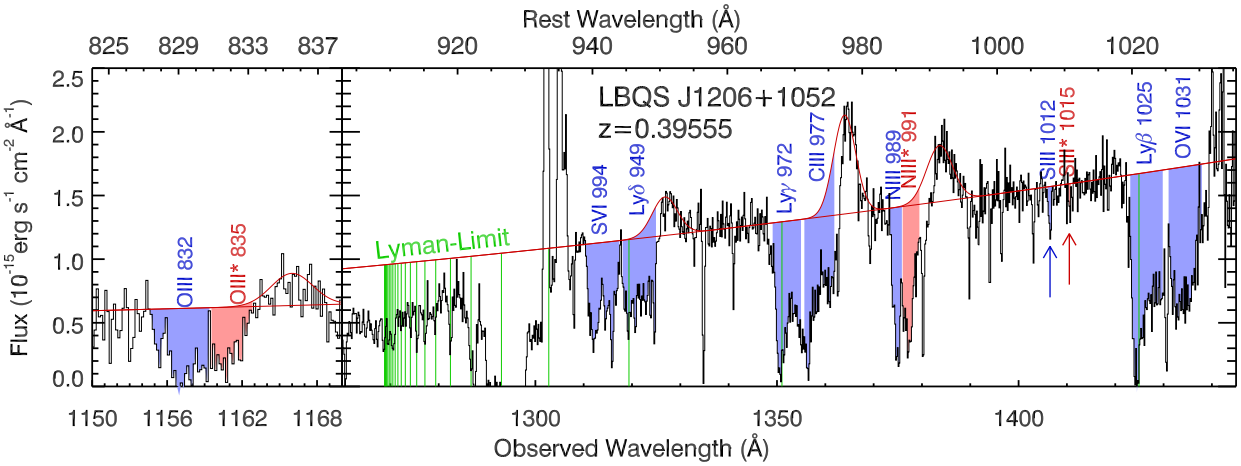

or in low S/N regions of the spectrum. The deepest portion of the absorption is at a velocity $v = -1400$ km s^{-1} blueshifted relative to the QSO rest frame and has a width of ~ 1800 km s^{-1}.

2.3.2 Unabsorbed emission model

We model the continuum emission of the spectrum using a power-law of the form $F(\lambda) = F_{1100}(\lambda/1100)^{\alpha}$, where $F_{1100} = 9.80 \times 10^{-14}$erg s^{-1}cm^{-2}Å^{-1} is the observed flux at 1100Å (rest-frame) and $\alpha \simeq 4.8$. De-reddening the spectrum using $E(B-V) = 0.021$ (Schlegel, Finkbeiner & Davis, 1998) results in $\alpha \simeq 4.6$ and increases the flux by 30%.

The Broad Emission Line (BEL) doublet transitions were modeled as Gaussians that fit any features protruding above the continuum power-law. Each BEL cannot be fit in its entirety since the absorption troughs associated with the outflow lie on the blue side of their corresponding BELs. We therefore fit the red wing of each BEL and note that the uncertainty in the corresponding blue wings have only a small effect on the column density

Table 2.1: List of lines used for excited-state modelling.

Ion	E_i^a	λ (Å)	f^b
N III	0	989.799	0.122
N III	174	991.511	0.0122
N III	174	991.577	0.110
O III	0	832.929	0.107
O III	113	833.715	0.0266
O III	113	833.749	0.0800
O III	306	835.059	0.00107
O III	306	835.092	0.0160
O III	306	835.289	0.0894
S III	0	1012.495	0.0425
S III	298	1015.502	0.0141
S III	298	1015.567	0.0106
S III	298	1015.779	0.0176

[a]Lower energy level in cm^{-1}
[b]Oscillator strength

measurements.

2.3.3 N III Absorption troughs

The absorption troughs from the ions in Figure 2.3 (e.g. Lyβ) exhibit a profile that is skewed towards the red side of the trough (i.e. has a "tail" extending to longer wavelengths). To parameterize the shape and depth of this profile while maintaining phenomenological flexibility, we fit the optical depth of line i from energy level j with the function

$$\tau_{ij}(v) = \frac{N_j f_i \lambda_i}{3.8 \times 10^{14}} \mathcal{P}(v) \quad \text{where} \tag{2.1}$$

$$\mathcal{P}(v) = \frac{1}{A} \frac{e^{s(v-v_1)/\sigma}}{1+e^{(v-v_1)/\sigma}} + \frac{A_g}{A} e^{-\frac{(v-v_o)^2}{2\sigma_g^2}} \quad (\mathrm{km\ s^{-1}})^{-1} \tag{2.2}$$

$$\text{with} \quad v_1 = v_o + \sigma \ln(1/s - 1) \quad \text{and}$$

$$A = \pi\sigma \csc(\pi s) + A_g \sigma_g \sqrt{2\pi}$$

$$\text{note that} \int_{-\infty}^{\infty} \mathcal{P}(v)\, \mathrm{d}v = 1$$

and where v_o is the velocity of the peak of the function, σ controls the "broadness" of the function, s determines the direction and extent of the "tail" (where $0 < s < 1$, and forms a blue or red tail for $s < 0.5$ or $s > 0.5$, respectively), N_j is the total ionic column density (cm^{-2}) of the respective energy level j, f_i is the dimensionless oscillator strength and λ_i is the rest wavelength in Angstroms of the line i. A_g and σ_g control the amplitude and width of the Gaussian portion of the template. The Gaussian profile in Equation (2.2) was included to accentuate the narrow peak of the absorption seen in the N III and other ionic troughs.

We fit the same template using a chi-squared minimization routine to the N III λ989 and N III* λ991 lines, allowing the shape and scale parameters to vary. The N_j for the ground and excited states are also varied. The right side of Figure 2.3.3 shows the best fit to the N III/N III* lines, corresponding to ionic column densities of $\log N_{\mathrm{N\,III}} = 15.44 \pm 0.02$ cm^{-2} and $\log N_{\mathrm{N\,III^*}} = 15.32 \pm 0.02$ cm^{-2}.

2.3.4 O III Absorption troughs

The O III absorption troughs have significantly lower S/N and are more self-blended than those of N III. We use the same absorption template given in Section 2.3.3 and fix the shape parameters to the N III solution. Using the n_e derived from N III (see Section 2.4.4) gives us the predicted optical depth ratio between the O III lines, leaving the total column density of O III as the sole parameter varied in the fit. Figure 2.3.3 shows that this fit provides an acceptable match to the data.

2.3.5 Other Absorption troughs

We identify absorption troughs associated with the outflow from the entire Lyman series, with the exception of Lyα (outside of our wavelength coverage), Lyϵ (contaminated with O I* geocoronal emission) and Ly6 (falls in the gap between the CCD chips). The depths of Lyβ and Lyγ are similar throughout the trough, indicating that the absorption is saturated

Figure 2.2: Best-fit of the O III and N III ground and excited lines using the absorption template from Section 2.3.3. Multiple lines arising from the same energy level share the same color and the combined absorption from all levels is represented as a solid black line. The spectrum is normalized via dividing the measured flux by the modeled continuum (see Section 2.3.2 and the red line in Figure 2.3). We remove the associated absorption system near 1380Å since it is much narrower and probably not part of the outflow (note that the system is seen in other lines as well).

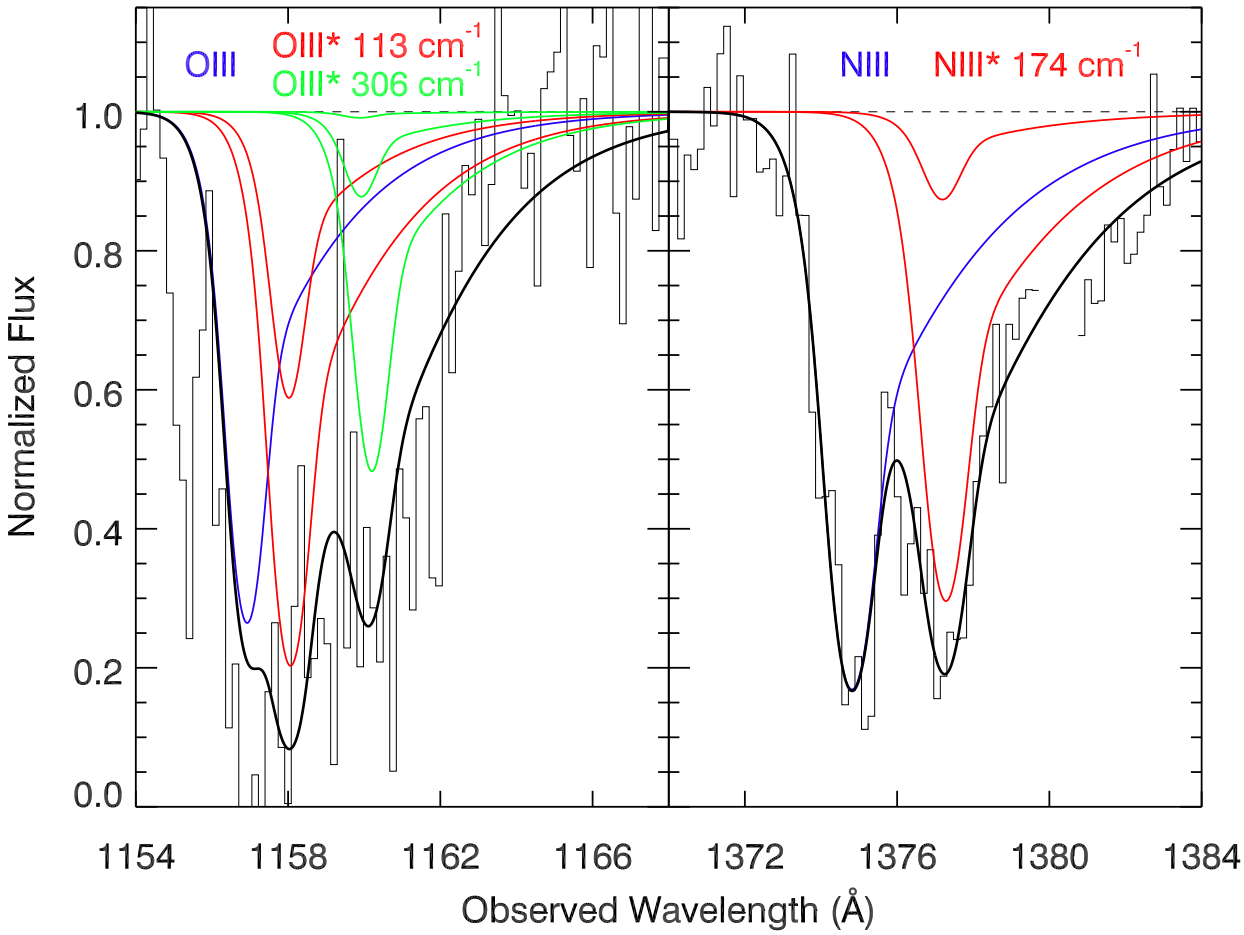

(Borguet et al., 2012a). The formation of a Lyman-limit spectral feature (see Figure 2.3) is another indication of this saturation. Ly11 (918.13Å) is the weakest line (and thus the least saturated) of the Lyman series detected in our data before blending becomes apparent. We therefore measure the Apparent Optical Depth (AOD, which assumes $I(v) = e^{-\tau(v)}$ where I is the normalized residual intensity and τ is the optical depth) of Ly11 as the lower limit to the H I ionic column density.

The Lyman-limit feature is optically thin and due to the data deficiencies (see Section 2.3) close to the Lyman-limit, we derive a conservative upper limit to the H I ionic column density from the normalized residual intensity at the bound-free transition (1 Ryd in the outflow rest-frame). For an estimated normalized residual intensity of one-half, the corresponding AOD optical depth is $\tau = 0.7$, leading to an ionic column density of $\log(N_{\rm H\,I}) = 17.06$ cm^{-2} using the relation $\tau = a_\nu N_{\rm H\,I}$ where a_ν is the photoionization cross section for H I.

For the remaining ions, we measure the AOD of the lines integrated over the velocity range of the Lyδ trough (the only H I trough whose wings are not blended with troughs of other ions) and report the ionic column densities in Table 2.2. To account for systematic errors in absorbed emission model, we increased the uncertainty to 0.1 dex for cases where the statistical error is less than 0.1 dex.

We normally treat AOD measurements from singlet lines as lower limits due to the possibility of non-black saturation, especially in the case of ions from abundant elements such as O VI. However, since the O VI and S VI troughs are shallower than the Lyβ and Lyγ troughs, we assume that O VI and S VI are not saturated and treat their AOD column densities as measurements. This assumption is also valid for all of the ions we measure since their singlet troughs are shallower than Lyβ. We note that the shape and depth of the C III trough is similar to the saturated Lyβ trough, and therefore we treat the C III measurement as a lower limit in Section 2.4.2.

We also detect absorption from Si II λ1012 and Si II* λ1015 which is narrow and shallow but kinematically associated with the deepest portion of the outflow absorption (i.e. at

Table 2.2: Ionic column densities for the LBQS J1206+1052 outflow.

Ion	$\log(N_{\rm obs})^a$ ($\rm cm^{-2}$)	$\log(N_{\rm mod})^b$ ($\rm cm^{-2}$)
H I	$16.90 - 17.06$	17.04
C III	> 14.95	16.15
N III	15.68 ± 0.1	15.68
O III	16.26 ± 0.15	16.45
O VI	15.55 ± 0.1	15.74
S III	15.09 ± 0.2	14.71
S VI	15.27 ± 0.1	14.99

[a]Each value is the sum of all energy levels (ground plus excited) for that ion.
[b]The ionic column densities predicted by our best-fit CLOUDY model (see Section 2.4.2).

$v = -1400$ km s^{-1}). We measure AOD column densities for the ground and excited levels of $\log N_{\rm Si\,II} = 14.76 \pm 0.08$ cm^{-2} and $\log N_{\rm Si\,II^*} = 14.70 \pm 0.1$ cm^{-2} respectively. The ratio between these two column densities is yet another diagnostic for finding $n_{\rm e}$ and will be used in Section 2.4.4. The absence of absorption troughs from the second excited energy level of Si II* (833 cm^{-1}) is consistent with the $n_{\rm e}$ solution of Section 2.4.4.

2.3.6 The SDSS spectrum

LBQS J1206+1052 was observed as part of the Sloan Digital Sky Survey (SDSS) in March 2003. The SDSS spectrum shows absorption from Mg II that is kinematically similar to the troughs seen in the COS spectrum. We also identify several lines from a metastable He I* level, but they are kinematically disconnected by 600 km s^{-1} from the Mg II troughs. However, ionic column densities extracted from He I* and Mg II would not be applicable to our photoionization analysis in Section 2.4.1 since the SDSS and COS observations differ by seven years.

2.4 Modelling

2.4.1 Photoionization analysis

To determine the photoionizaton structure of the outflow, we ran simulations using version c13.02 of CLOUDY (Ferland et al., 2013) with varying total hydrogen column density $N_{\rm H}$ and ionization parameter

$$U_{\rm H} = \frac{Q_{\rm H}}{4\pi R^2 n_{\rm H} c} \tag{2.3}$$

where $Q_{\rm H}$ is the rate of hydrogen-ionizing photons from the central source, R is the distance to the outflow from the central source, $n_{\rm H}$ is the hydrogen number density ($n_{\rm e} \simeq 1.2 n_{\rm H}$ in highly ionized plasma) and c is the speed of light. To visualize the photoionization solution, we identify the locus of these models that match (within the 1-σ uncertainties) the measured column density (from Table 2.2) for a particular ion. These loci of models are represented as colored contours in phase space, shown in Figure 2.4.1. No single solution is an exact match for our set of measurements and we find the solution with the least discrepancy by performing a chi-squared minimization. For a detailed explanation of this method, see Arav et al. (2013).

2.4.2 Photoionization solution

The upper and lower limits on the H I ionic column density obtained from the Lyman-Limit measurements constrain the solution to a relatively narrow (spanning 0.3 dex in $N_{\rm H}$) band in phase space (see Figure 2.4.1). The minimum χ^2 solution is satisfied inside the H I band, between the O VI and S VI contours and between the parallel N III, O III and Si II contours.

For two elements (oxygen and sulphur), we obtain ionic column densities from multiple ionization stages of the same element. Since the relative ratio of ions from the same element depends solely on the ionization parameter, the contours for these pairs of ions (O III and O VI, Si II and S VI) would cross at a $U_{\rm H}$ that is independent of abundance scaling between

Figure 2.3: Phase plot showing the photoionization solution. Each colored contour represents the locus of models ($U_{\rm H}$, $N_{\rm H}$) which predict a column density consistent with the observed column density for that ion. The bands which span the contours are the 1-σ uncertainties in the observations. The black "X" at the crossing point of the bands is the ionization solution for this outflow ($\log(U_{\rm H}) = -1.82, \log(N_{\rm H}) = 20.46$) and is surrounded by the 1-σ confidence level (solid black line).

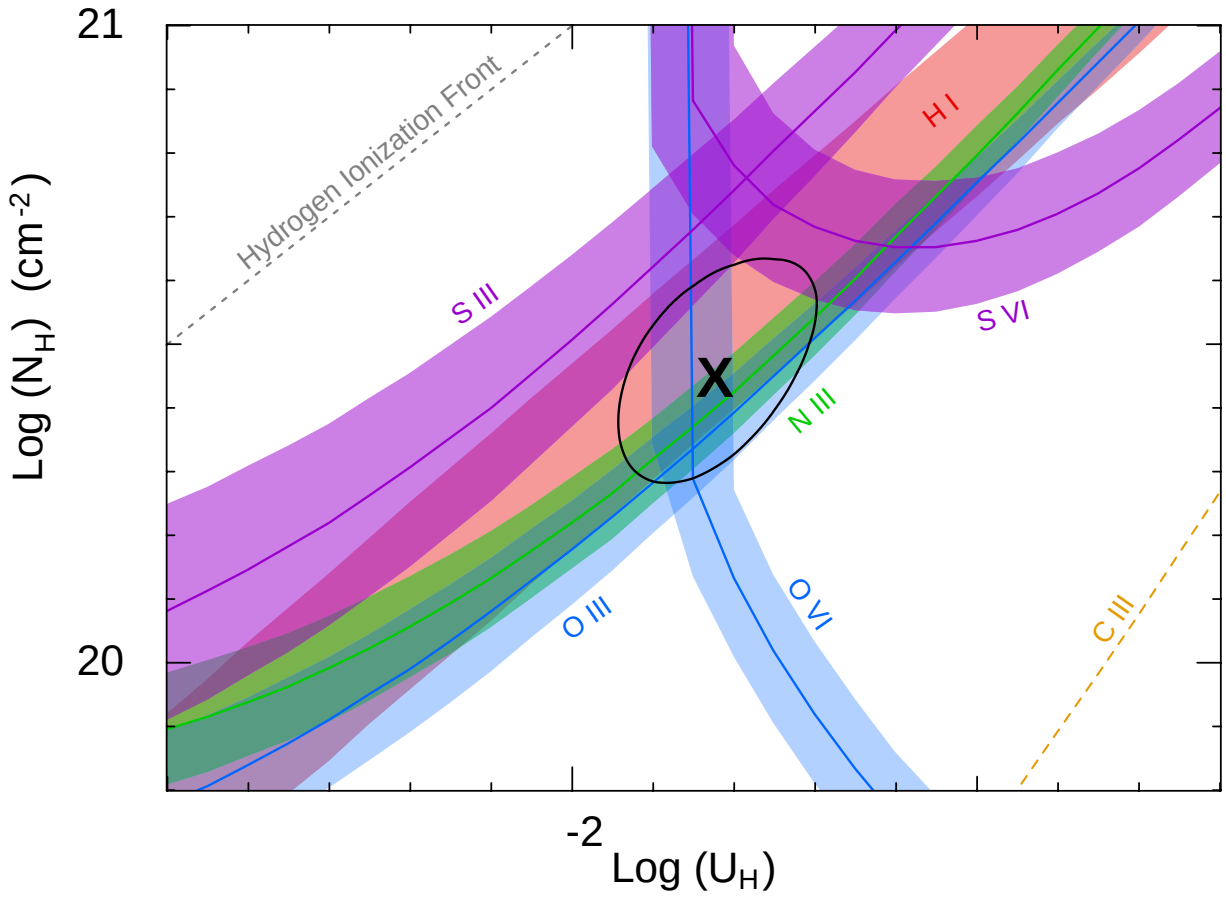

elements (i.e. metallicity). Figure 2.4.1 shows that the Si II and S VI contours cross at approximately the same $U_{\rm H}$ as the O III and O VI contours cross at $U_{\rm H} \simeq -1.8$.

The best-fit solution we obtain for this outflow is $\log(U_{\rm H}) = -1.82 \pm 0.12$ and $\log(N_{\rm H}) = 20.46 \pm 0.17$ cm^{-2}, using the UV-soft Spectral Energy Distribution (SED) described in Arav et al. (2013) and assuming solar metallicity. The other SEDs considered in Arav et al. (2013) vary the solution by no more than 0.3 dex and 0.2 dex in $U_{\rm H}$ and $N_{\rm H}$ respectively. We calculate $Q_{\rm H}$ by scaling the SED shape to the measured (de-reddened) continuum flux and integrating over the energy range > 1 Ryd (see Dunn et al. 2010), resulting in $Q_{\rm H} = 3.4 \times 10^{55}$ s^{-1} for the UV-soft SED.

The ionic column densities predicted by the best-fit solution are given in the second column of Table 2.2. A comparison between the observed and predicted column densities show that all ions, with the exception of C III, agree to within a factor of two. The ions that are overpredicted by the solution (N III and O III) can therefore be saturated by no more than a factor of two.

2.4.3 Metallicity constraints

Using the same method as Arav et al. (2013), we constrain the metallicity of the gas to be close to solar. If all metal abundances relative to hydrogen drop by a factor of three ($Z = \frac{1}{3}$Z$_\odot$) or increase by a factor of two ($Z = 2$Z$_\odot$), then the H I column density will be over- or under-predicted respectively.

2.4.4 Collisional excitation modelling

The excited states of N III, O III and Si II are populated by collisional excitation, a process that is dependent on the electron number density $n_{\rm e}$ and is relatively insensitive to temperature (the temperature variation for these ions is similar to fig. 8 of Borguet et al. 2013). Predictions of the populations of the excited and ground states for values of $n_{\rm e}$ are calcu-

lated using the Chianti 7.1.3 atomic data base (Landi et al., 2013), then compared with the observations to determine n_e. For a detailed explanation of this method, see Korista et al. (2008).

Figure 2.4.4 shows the theoretical population ratios for N III*/N III and Si II*/Si II as a function of n_e. The temperature used for the collisional excitation models was the electron temperature from our best-fit CLOUDY model from Section 2.4.2 (14 000 K). A factor of two deviation from this temperature changes the critical n_e by no more than 0.13 dex. The measured ratios (and their uncertainties) are also shown in Figure 2.4.4 and the n_e inferred from both ions are in close agreement. For highly ionized plasma, $n_e \simeq 1.2 n_H$, thus we determine $\log(n_H) = 2.95 \pm 0.06$ cm^{-3} using the stricter N III measurement of $\log(n_e) = 3.03 \pm 0.06$ cm^{-3}.

For O III and O III*, the n_e was fixed to the value from the N III solution since a) heavy blending of the O III troughs made it difficult to determine the relative depth of the individual lines and b) low S/N caused line template modeling of the blend to fit the data with a wide range of model parameters. O III was therefore used to support the n_e measurement from N III by demonstrating that the n_e solution yields a kinematically-related absorption profile that fits the observed trough.

2.4.5 Distance and energetics

Since $U_H \propto R^{-2} n_H^{-1}$ (see Equation (2.3)), measurement of both U_H and n_H allows for the calculation of R (see Borguet et al. 2013 for discussion). Using the values for Q_H, U_H and n_H derived in the previous sections, we find that the outflow is located a distance of $R = 840 \pm 60$ pc from the central source.

Assuming a simple outflow geometry of a thin, partially filled spherical shell, knowledge of N_H and R allows us to calculate the mass-flow rate ($\dot{M}$) and kinetic luminosity ($\dot{E}_k$) of the outflow (see Borguet et al., 2012b, for discussion)

$$\dot{M} = 4\pi R \Omega \mu m_p N_H v \tag{2.4}$$

Figure 2.4: Electron number density n_e and distance R to the outflow from the central source. The theoretical ratios between the ground and excited state populations for N III and Si II are dependent on n_e and are plotted in blue and red, respectively. The n_e value determined from the measured ratio of N III*/N III closely agrees with the value determined additionally and independently using Si II*/Si II. The ionization parameter U_H allows the conversion from n_e to R which is shown on the top axis (see Section 2.4.5).

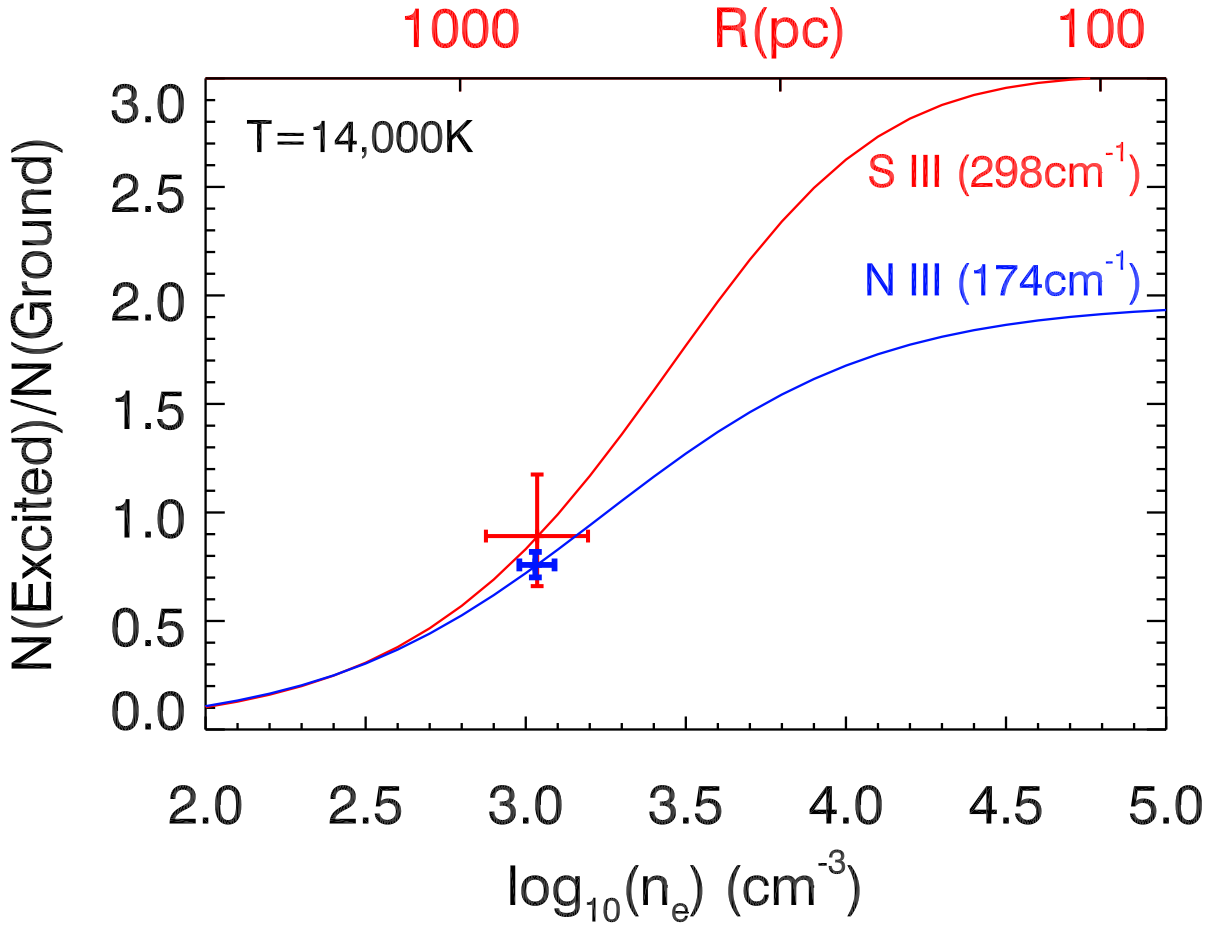

$$\dot{E}_{\rm k} \;=\; 2\pi R\Omega\mu m_p N_H v^3 \tag{2.5}$$

where Ω is the global covering fraction (of 4π steradians) of the outflow, $\mu = 1.4$ is the mean atomic mass per proton, m_p is the mass of the proton and v is the radial velocity of the outflow. Using the values derived in the previous sections and adopting $\Omega = 0.2$ for the typical detection rate of C IV outflows, we find $\dot{M} = 9 \pm 3$ M$_\odot$ yr^{-1} and $\dot{E}_{\rm k} = 10^{42.78\pm0.15}$ erg s^{-1}.

We determine an Eddington luminosity of $L_{\rm Edd} = 10^{47.75}$ erg s^{-1} from the mass of the SMBH, which we determine using the virial mass estimator from equation (5) of Vestergaard & Peterson (2006). The continuum luminosity at 5100Å (rest-frame) and FWHM (full width at half-maximum) of the Hβ BEL are required for the mass estimate, and we measure these quantities from the SDSS spectra. The kinetic luminosity we measure for this outflow corresponds to $\dot{E}_{\rm k} = 10^{-5} L_{\rm Edd}$, which is insignificant in the context of AGN feedback (see Introduction).

2.5 Discussion

2.5.1 Robustness of the $n_{\rm e}$ measurement

LBQS J1206+1052 provides a self-consistent measurement of the electron number density $n_{\rm e}$ of the outflowing gas. This self-consistency is due to the simultaneous detection of multiple ions with excited states conducive to our method of determining $n_{\rm e}$. Such multiple-detection was previously seen in Moe et al. (2009); Dunn et al. (2010) using singly-ionized species. In NGC 5548 (Arav et al., 2015, their fig. 4), excited-state measurements of C III and Si III also yielded consistent $n_{\rm e}$. The analogous ions in LBQS J1206+1052 are N III and Si II, and the $n_{\rm e}$ inferred from these measurements fully agree. The column density ratio of N III*/N III is firmly below 1.0 (0.76±0.06, based on the measurements given in Section 2.3.3), eliminating the possibility of saturation in the excited trough discussed in Borguet et al. (2013) occurring

for troughs with a 1:1 ratio or larger in depth. We also note that a significantly higher $n_{\rm e}$ would require a deeper O III* 306 cm^{-1} absorption than observed (see Figure 2.3.3).

2.5.2 Robustness of $U_{\rm H}$ and R measurements

The distance R to the outflow from the central source was extracted from the determination of $U_{\rm H}$ and $n_{\rm e}$. Even if $n_{\rm e}$ is determined both accurately and precisely, a poorly-constrained $U_{\rm H}$ will result in an unreliable measurement of R. As we discuss in Section 2.4.2, the $U_{\rm H}$ of the outflow was determined to within 0.12 dex precision and is also independent of the metallicity of the gas. The choice of SED has a greater effect on the accuracy of $U_{\rm H}$, but this only shifts the solution by up to 0.3 dex among the three SEDs considered in Arav et al. (2013), which changes R by up to 0.15 dex.

The Mg II column density measured from the SDSS spectrum is underpredicted by our 2010 photoionization solution by a large factor. This discrepancy can be explained if the ionization parameter was 0.4 dex lower during the 2003 epoch.

2.5.3 Contrasting distance determination with theoretical wind models

The outflow of LBQS J1206+1052 is located farther from the central source than is assumed for line-driven winds launched from the accretion disc ($\sim$ 0.01 pc, Murray et al., 1995). The outflow distance is also greater than that of outflows originating from the obscuring torus ($\lesssim$ 30 pc, Krolik & Kriss, 2001). Our distance measurement of $R = 840$ pc for this outflow most closely agrees with the kiloparsec-scale "in situ" trough formation model of Faucher-Giguère & Quataert (2012).

2.6 Summary

We present the analysis of the outflow from LBQS J1206+1052 using data obtained with HST/COS.

The data show absorption troughs from N III, O III, Si II and the excited states of those ions. We used the ratio of the excited column density to ground for two separate ions (N III and Si II) to calculate a self-consistent electron number density of $\log(n_e) = 3.03 \pm 0.06$ cm^{-3} using collisional excitation modeling.

Ionic column densities were extracted from the absorption troughs of H I, C III, O VI and S VI and were used to determine the photoionization solution of $\log(U_H) = -1.82 \pm 0.12$ and $\log(N_H) = 20.46 \pm 0.17$ cm^{-2}. The photoionization parameter was used with the electron number density to derive a distance of $R = 840 \pm 60$ pc to the outflow from the central source.

The mass flux and kinetic luminosity of the outflow was determined to be $\dot{M} = 9 \pm 3$ M$_\odot$ yr^{-1} and $\dot{E}_k = 10^{42.78 \pm 0.15}$ erg s^{-1} respectively. This outflow has insufficient $\dot{E}_k$ to provide significant AGN feedback (Scannapieco & Oh, 2004; Hopkins & Elvis, 2010). The concurrent use of excited states from two different ions, combined with a well-constrained photoionization solution, demonstrates the reliability of this method for determining outflow distances.

Acknowledgements

We acknowledge support from NSF grant AST 1413319 and from NASA STScI grants GO 11686 and GO 12022. The data presented in this paper were obtained from the Mikulski Archive for Space Telescopes (MAST).

Chapter 3

Strong candidate for AGN feedback: VLT/X-shooter observations of BALQSO SDSS J0831+0354

3.1 Abstract

We measure the location and energetics of a S IV BALQSO outflow. This ouflow has a velocity of 10,800 km s^{-1} and a kinetic luminosity of $10^{45.7}$erg s^{-1}, which is 5.2% of the Eddington luminosity of the quasar. From collisional excitation models of the observed S IV/S IV* absorption troughs, we measure a hydrogen number density of $n_{\rm H}$=$10^{4.3}$ cm^{-3}, which allows us to determine that the outflow is located 110 pc from the quasar. Since S IV is formed in the same ionization phase as C IV, our results can be generalized to the ubiquitous C IV BALs. Our accumulated distance measurements suggest that observed BAL outflows are located much farther away from the central source than is generally assumed (0.01-0.1 pc).

3.2 Introduction

Broad absorption line (BAL) outflows are detected as absorption troughs that are blueshifted in the rest-frame spectrum of 20–40% of quasars (Hewett & Foltz, 2003; Ganguly & Brotherton, 2008; Knigge et al., 2008; Dai, Shankar & Sivakoff, 2008). From their detection rate, we deduce that these outflows cover on average ∼20–40% of the solid angle around the quasar. Such large opening angles allow for efficient interaction with the surrounding medium. As shown by simulations, the mass, momentum and especially the energy carried by these outflows can play an important role in the evolution of galaxies and their environments (e.g. Scannapieco & Oh, 2004; Levine & Gnedin, 2005; Hopkins et al., 2006; Cattaneo et al., 2009; Ciotti, Ostriker & Proga, 2009, 2010; Ostriker et al., 2010; Gilkis & Soker, 2012; Choi et al., 2014). Theoretical studies show that such interactions can provide an explanation for a variety of observations: the self-regulation of the growth of the supermassive black hole and of the galactic bulge, curtailing the size of massive galaxies, and the chemical enrichment of the intergalactic medium. These processes are part of the so-called AGN feedback (e.g. Silk & Rees, 1998; Di Matteo, Springel & Hernquist, 2005; Germain, Barai & Martel, 2009; Hopkins, Murray & Thompson, 2009; Elvis, 2006; Zubovas & Nayakshin, 2014, and references therein).

The importance of quasar outflows to AGN feedback depends on the mass-flow rate ($\dot{M}$) and kinetic luminosity ($\dot{E}_{\rm k}$) of the outflowing material. An $\dot{E}_{\rm k}$ value of at least 0.5% (Hopkins & Elvis, 2010) or 5% (Scannapieco & Oh, 2004) of the Eddington luminosity ($L_{\rm Edd}$) is deemed sufficient to produce the aforementioned feedback effects. A crucial parameter needed to determine $\dot{E}_{\rm k}$ is the distance R to the outflow from the central source. Lacking spatial image information, we deduce R from the value of the ionization parameter ($U_{\rm H}$, see Section 3.5) once the hydrogen number density ($n_{\rm H}$) of the gas is known. Our group has determined $n_{\rm H}$ (leading to R, $\dot{M}$ and $\dot{E}_{\rm k}$) for several quasar outflows (e.g. Moe et al., 2009; Dunn et al., 2010; Bautista et al., 2010; Aoki et al., 2011; Borguet et al., 2012b) by utilizing absorption lines from excited states of singly-ionized species (e.g. Fe II* and Si II*).

Table 3.1: Physical properties of energetic quasar outflows.

Object	v (km/s)	R (pc)	$\dot{M}$ ($M_\odot$/yr)	Log $\dot{E}_k$ (erg/s)	$\dot{E}_k/L^d_{\rm Edd}$ (%)
SDSS J0831+0354[1]	-10800	110[a]	135	45.7	5.2
SDSS J1106+1939[2]	-8250	320[a]	390	46.0	12
HE 0238-1904[3]	-5000	3400[b]	140	45.0	0.7
SDSS J0838+2955[4]	-5000	3300[c]	300	45.4	2.3
SDSS J0318-0600[5]	-4200	6000[c]	120	44.8	0.13

R from: [a]high-ionization S IV*/S IV; [b]high-ionization O IV*/O IV; [c]low-ionization Si II*/Si II
[d]See Section 3.6.1 for $L_{\rm Edd}$ determination.
References. (1) this work; (2) Borguet et al. 2013; (3) Arav et al. 2013; (4) Moe et al. 2009; (5) Dunn et al. 2010.

Absorption troughs from singly-ionized species classify an outflow as a LoBAL. The lower detection rate of LoBALQSO in spectroscopic surveys (3–7%) compared with 20–40% for C IV BALQSO (Dai, Shankar & Sivakoff, 2012) raises the question of whether the determinations obtained for these objects are representative of the ubiquitous high-ionization C IV BALQSO (see Dunn et al., 2010). The most straightforward way to avoid such uncertainty is to observe outflows that show absorption lines from excited states of ions with a similar ionization potential to that of C IV. The optimal ion for ground-based observations is S IV (see discussion in Dunn et al., 2012; Arav et al., 2013).

To realize this, we conducted a survey using VLT/X-shooter between 2012 and 2014 aimed at finding quasar outflows showing absorption from S IV λ1062.66 and the excited state S IV* λ1072.97. Of the 24 objects observed, two objects (SDSS J1106+1939 and SDSS J1512+1119) have been published (Borguet et al., 2013, hereafter Paper I). SDSS J1106+1939 yielded the most energetic S IV BAL outflow to date with $\dot{E}_{\rm k}$=$10^{46.0}$ erg s^{-1} (see Section 3.6.3 for further discussion), whereas the SDSS J1512+1119 outflow has $\dot{E}_{\rm k} \lesssim 10^{43.8}$ erg s^{-1}. In this paper, we present the analysis of an outflow from SDSS J0831+0354, which exhibits similar properties to that of SDSS J1106+1939. This includes the presence of P V and S IV/S IV* troughs, thereby allowing us to determine the distance and energetics (see Section 3.6.1) of

the SDSS J0831+0354 outflow. Table 3.1 summarizes the current state of the field by listing the energetics of prominent outflows analyzed by our group.

The plan of this paper is as follows. In Section 3.3 we present the VLT/X-shooter observations of SDSS J0831+0354. In Section 3.4 we identify the absorption troughs of the outflow and measure the ionic column densities which are used to determine the number density (Section 3.4.4) and the photoionization solution (Section 3.5). In Section 3.6 we determine the outflow distance and energetics and compare them to outflows from other objects. We summarize our method and findings in Section 3.7.

3.3 Observations and data reduction

SDSS J0831+0354 (J2000: RA=08 31 26.15, DEC=+03 54 08.0, z=2.0761) was observed with VLT/X-shooter ($R \sim$ 6000–9000, see Paper I for instrument specifications) as part of our program 92.B-0267 (PI: Benn) in January 2014 with a total integration time of 10640s.

We reduced the SDSS J0831+0354 spectra in a similar fashion to those of SDSS J1106+1939 (detailed in Paper I): we rectified and wavelength calibrated the two-dimensional spectra using the ESO Reflex workflow (Ballester et al., 2011), then extracted one-dimensional spectra using an optimal extraction algorithm and finally flux calibrated the resulting data with the spectroscopic observations of a standard star observed the same day as the quasar. The one-dimensional spectra were then coadded after manually performing cosmic-ray rejection on each spectra. We present the reduced UVB+VIS spectrum of SDSS J0831+0354 in Figure 3.4.1.

3.4 Spectral fitting

Absorption troughs associated with H I, C IV, N V, Mg II, Al III, Si III, Si IV, P V and S IV/S IV* ionic species are seen in the spectrum (see Figure 3.4.1). The high velocity (v=−10800

km s^{-1}) and width (3500 km s^{-1}) of the C IV trough satisfies the definition of a BAL outflow (i.e. $v_{\rm max} > 5000$ km s^{-1} and width > 2000 km s^{-1}, see Weymann, Carswell & Smith, 1981). The balnicity index of the C IV trough is 1100 km s^{-1} (see Weymann et al., 1991).

3.4.1 Unabsorbed Emission Model

We correct the spectrum for galactic extinction ($E(B-V) = 0.025$; Schlegel, Finkbeiner & Davis, 1998) using the reddening curve of Cardelli, Clayton & Mathis (1989). We then fit the continuum with a cubic spline resembling a power law of the form $F(\lambda) = F_{1100}(\lambda/1100)^{\alpha}$, where $F_{1100} = 1.58 \times 10^{-16}$erg s^{-1}cm^{-2}Å^{-1} is the observed flux at 1100Å (rest-frame) and $\alpha \simeq -1.16$. We model the broad emission lines (BEL) with a sum of one to three Gaussians, which does not significantly affect the column density extraction for most ions since the high velocity of the outflow (v=-10800 km s^{-1}) shifts the BALs far from the wings of their corresponding BELs. However, the S IV and S IV* BALs lie within the O VI BEL, which we model by scaling the C IV BEL template to match the peak emission of the S IV BAL region.

3.4.2 The blended troughs

We model the optical depth of the absorption troughs with three Gaussians

$$\tau(v) = \sum_{i=1}^{3} \tau_i \exp\left[\frac{-(v-v_i)^2}{2\sigma_i^2}\right] \qquad \text{FWHM} = 2\sqrt{2\ln 2}\,\sigma \tag{3.1}$$

with the same centroid and width in all the observed ionic troughs. Our first Gaussian (v_1=−12,100 km s^{-1}, FWHM=1460 km s^{-1}) is chosen specifically to match the blue wing of the Si IV λ1393.75 line, as well as the blue wing of the Al III λ1854.72 line. The second Gaussian (v_2=−10,800 km s^{-1}, FWHM=940 km s^{-1}), which represents the majority of the absorption, targets the Si IV and P V doublets. A third Gaussian (v_3=−10,000 km s^{-1}, FWHM=590 km s^{-1}) is needed to match the red wing of the Al III λ1862 line, as well as the red wing of the C IV and N V blends. These three Gaussians form the template used

Figure 3.1: VLT/X-shooter spectrum of the quasar SDSS J0831+0354 (z=2.0761). We label the ionic absorption troughs associated with the outflow, and represent the unabsorbed emission model with the red dashed line (see Section 3.4.1). Narrow absorption from intervening systems appear throughout the spectrum, and terrestrial absorption from molecular O_2 in our atmosphere is seen near 6850Å and 7600Å observed frame, but none of these features affect the analysis presented here.

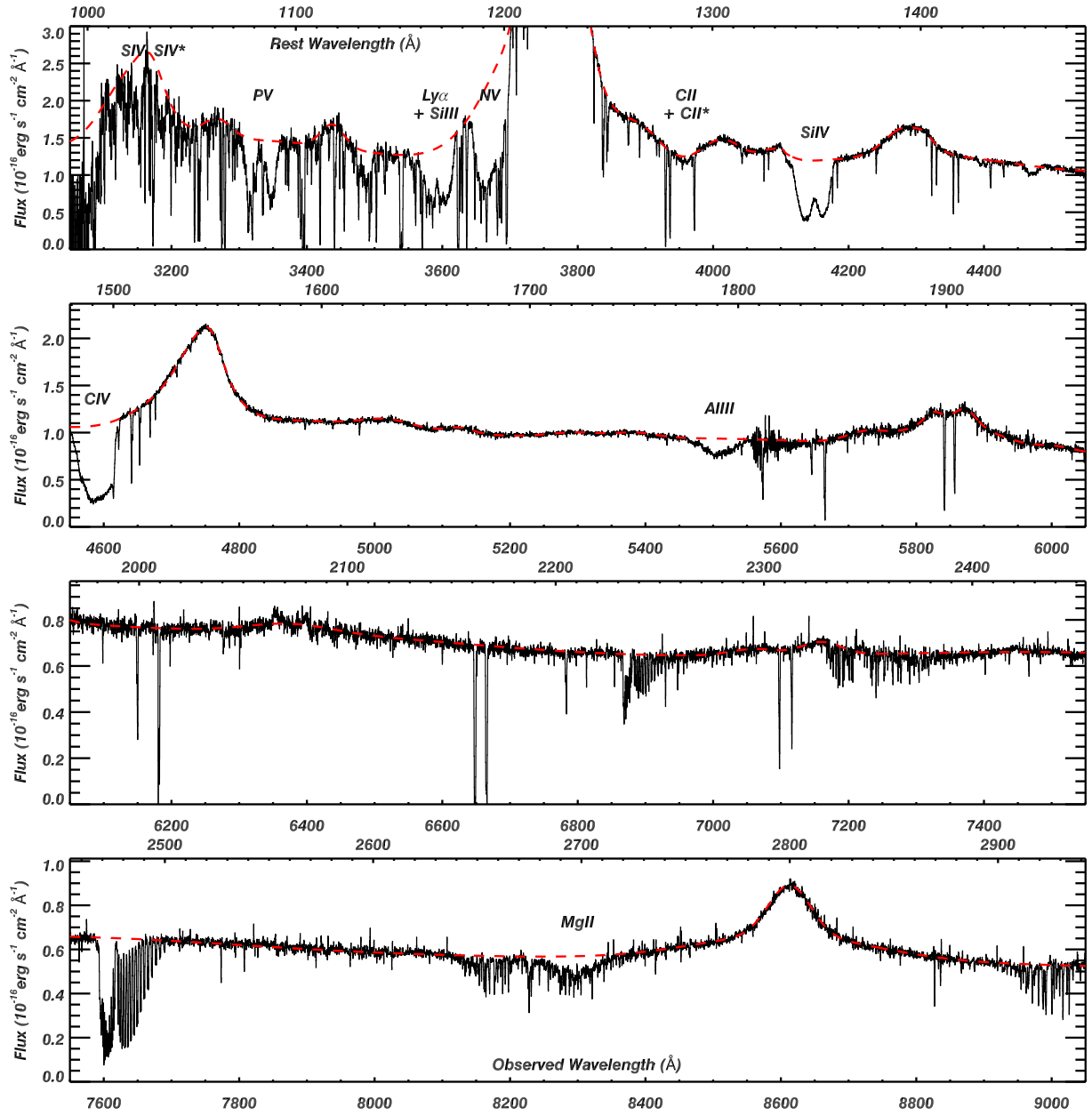

to extract the column density (following the same procedure as Paper I) from the observed troughs of all ions except for P V and Si III, which will be discussed in the next section. For the three-Gaussian template, we use a covering factor ($C_{\rm ion}$) that is constant throughout the trough (i.e. for all three Gaussians), and varies only between ions. For a description of the partial covering (PC) model, see Arav et al. (2008). For ions detected by a singlet, we take the apparent optical depth (AOD) measurement as a lower limit.

3.4.3 Velocity-dependent covering: P V and Si III

Although the central Gaussian of our template (see Section 3.4.2) can be used to model the P V and Si IV doublet troughs, the ratio between the red and the blue components of each doublet approaches 1:1. This suggests that the troughs are strongly influenced by the velocity-dependent partial covering of the emission source (see Borguet et al., 2012a; Arav et al., 1999a). Due to the presence of Lyα forrest intervening troughs, we proceed by modeling the normalized flux of the doublets with a smooth function. For phenomenological flexibility, we built a function from the product of two logistic functions (hereafter logistic fit)

$$I(v) = 1 - \frac{A}{\left(1 + e^{w_b(v-v_b)}\right)\left(1 + e^{w_r(v-v_r)}\right)} \tag{3.2}$$

where A is the maximum depth of the logistic fit, v_b and v_r are the velocities of the blue and red wing half-maximums respectively ($v_b \leq v_r$), and w_b and w_r are the slope/variance of the blue and red wings respectively ($w_b < 0 < w_r$). This function is particularly suited to fitting asymmetric troughs.

We model each P V doublet component (normalized and in velocity-space) using a logistic fit, and determine the velocity-dependent covering fraction and optical depth solution (using Equation (3) of Dunn et al., 2010). Integrating this optical depth over the trough yields the P V column density for the partial covering model given in Table 3.4.4.

Si III is a singlet, thus we cannot determine a covering model for this ion. Therefore, we

Figure 3.2: Fits to the absorption troughs observed in the X-shooter spectrum of SDSS J0831+0354. Each trough is fit by scaling the optical depths of three template Gaussians whose centroid and width are fixed among the ions (see Section 3.4.2). The Gaussian templates for each transition are shown in the same color (red or blue), and the combined absorption from blended lines is represented as a black solid line. The first row of plots show the apparent optical depth (AOD) fits to Si III (and H I), Mg II and Al III. Due to the influence of non-black saturation in the Si IV and P V troughs (see text), we show the velocity-dependent partial covering (PC(v)) fit to those ions. The plot in the lower-right shows the PC(v) fit to the S IV and S IV* troughs in velocity space. The fits are spanned by shaded contours representing the upper and lower errors assigned to the fits.

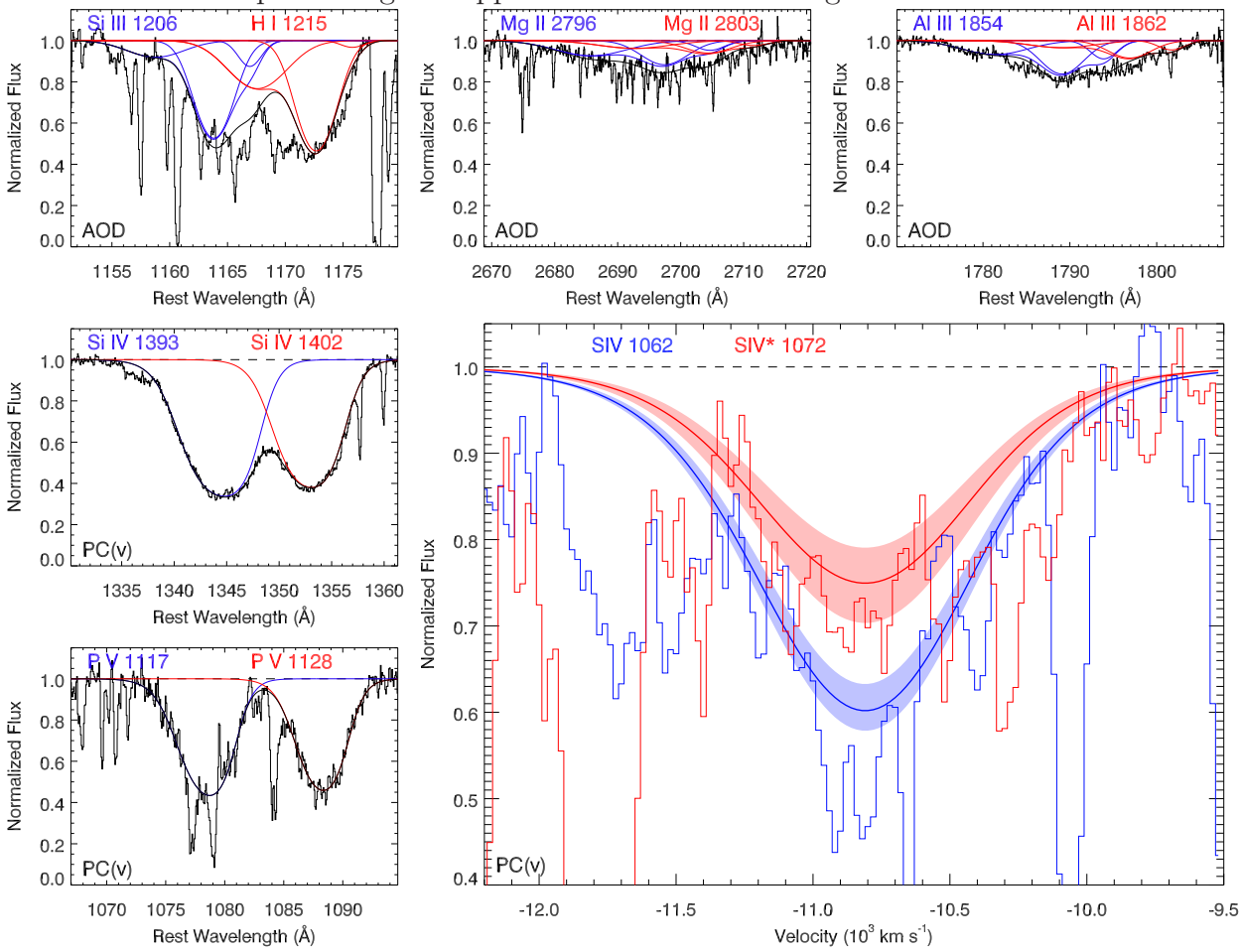

use the covering factor of Si IV as a proxy to extract the Si III PC column density given in Table 3.4.4, since Si IV is the next ionization stage of the same element. The lower error of 0.11 dex for the adopted Si III measurement includes systematic errors in continuum placement and blending of the intervening Lyα forest. We note that, by coincidence, the difference between the PC measurement and the apparent optical depth (AOD) measurement is also 0.11 dex.

3.4.4 The density-sensitive troughs: S IV and S IV*

The column densities from S IV and its excited state S IV* play an essential role in our analysis: the ratio of level populations between S IV* and S IV is dictated by collisional excitation, which depends on n_e and is relatively insensitive to temperature (see Figure 8 of Paper I).

As in the case of Si III, S IV λ1062.66 and S IV* λ1072.97 are both singlets (the lines arise from different energy levels with a priori undetermined populations), thus a velocity dependent covering solution cannot be determined from these two lines alone. Therefore, we follow the same method as with Si III, using the velocity-dependent covering template of Si IV to model the S IV/S IV* troughs with the PC(v) method.

We begin this method by modeling the S IV/S IV* troughs using a logistic curve that closely resembles the central Gaussian of the three Gaussian template. This resemblence ensures that the S IV absorption model is kinematically related to the other ionic troughs in the outflow. The logistic curve was fit to the S IV troughs by scaling the amplitude until it fit the broad absorption features in the spectrum while excluding the narrow Lyα troughs. To assign the upper and lower errors to this fit we again scale the depth of the logistic template until the resulting template clearly over- or under-predicts significant portions of the broad absorption trough. The quality of this fit and of the stated errors can be judged in the lower right panel of Figure 3.4.2.

The optical depth of the fit (and its errors) was translated to S IV/S IV* column density measurements using the same procedure as in Si III (i.e. adopting the velocity-dependent covering solution for Si IV). These column densities are reported in the fourth column of Table 3.4.4. A similar value (differing by only 0.05 dex) was obtained with the P V velocity-dependent covering template, demonstrating the robustness of this method.

To obtain the AOD column density, we follow the same procedure as the PC(v) modeling, instead using the central Gaussian of the three Gaussian template described in Section 3.4.2. For completion, we also apply the *constant* partial covering template of Si IV to the S IV/S IV* absorption (using the central Gaussian as the optical depth template), and report the PC column density in the third column of Table 3.4.4.

We deduce the n_e of the outflow by comparing the S IV*/S IV column density ratio to predictions (see Figure 3.4.4) made with the Chianti 7.1.3 atomic database (Landi et al., 2013). Using the column densities for S IV and S IV* reported in Table 3.4.4 and the electron temperature found for our best-fit Cloudy models from Section 3.5 (9000 K, a weighted average for S IV across the slab), we find $\log(n_e) = 4.42^{+0.26}_{-0.22}$ cm^{-3} by averaging the two absorption models (reported in Table 3.4.4) and adding their errors in quadrature.

3.5 Photoionization analysis

We use photoionization models in order to determine the ionization equilibrium of the outflow, its total hydrogen column density (N_H), and to constrain its metallicity. The ionization parameter

$$U_H \equiv \frac{Q_H}{4\pi R^2 c n_H}, \tag{3.3}$$

(where Q_H is the source emission rate of hydrogen ionizing photons, R is the distance to the absorber from the source, c is the speed of light, and n_H is the hydrogen number density) and N_H of the outflow are determined by self-consistently solving the ionization and thermal balance equations with version c08.01 of the spectral synthesis code Cloudy, last described

Figure 3.3: Density diagnostic using the S IV*/S IV ratio for the SDSS J0831+0354 outflow, presented in the same manner as Paper I: we plot the S IV*/S IV theoretical ratio versus electron number density and overlay our measured value (for two absorber models, AOD and velocity-dependent PC(v)) to determine the number density and its errors.

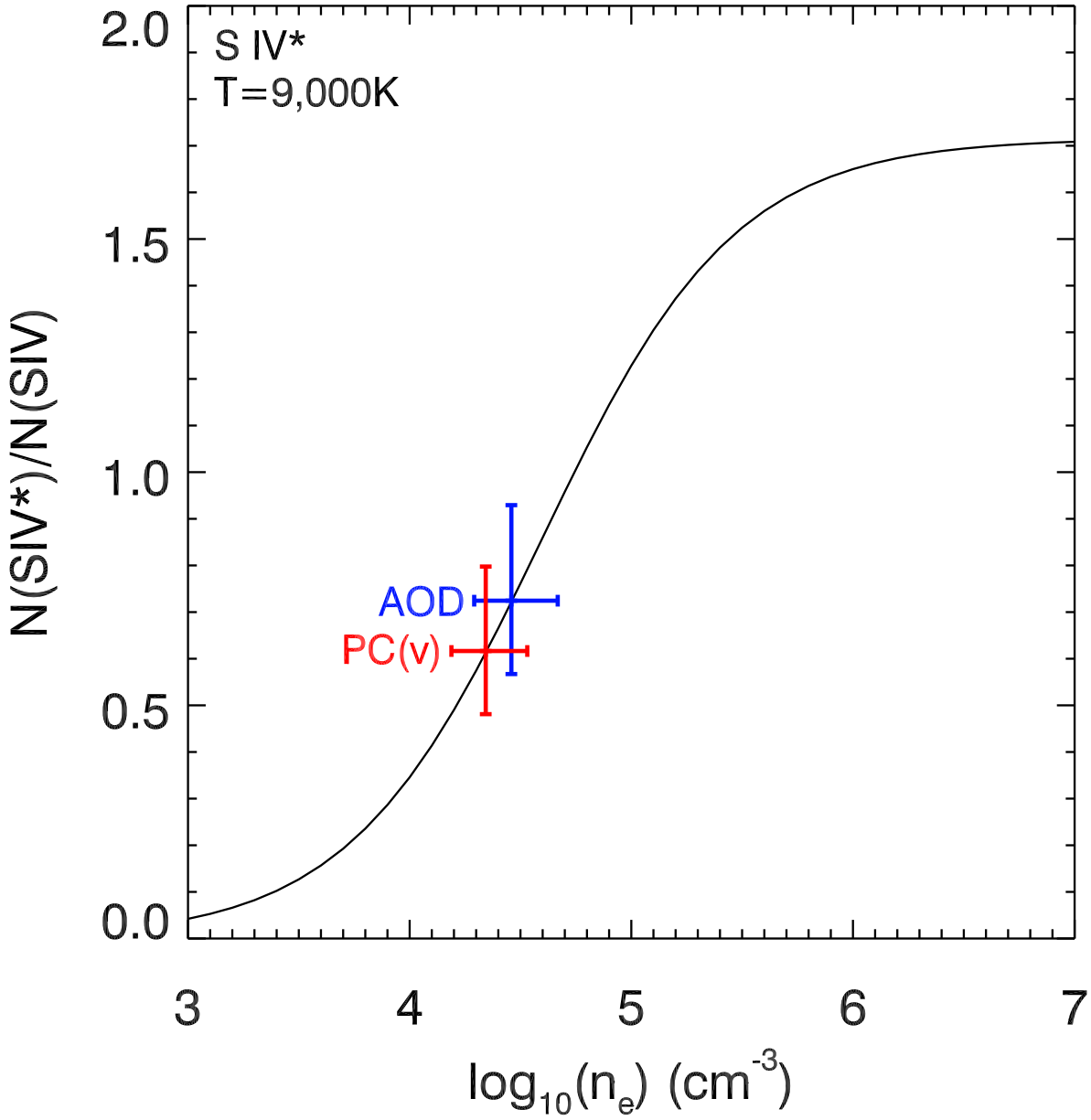

Table 3.2: SDSS J0831+0354 log column densities (cm^{-2}) for the three absorption models AOD, PC and PC(v) (velocity-dependent covering). Upper limits are shown in red and lower limits are in blue.

Ion	AOD	PC	PC(v)	Adopted[a]
H I	>14.96	>15.17	—	>15.17
He I*	<15.14	—	—	<15.14
C II	<14.46	—	—	<14.46
C IV	>15.50	>15.65	—	>15.65
N V	>15.60	>15.79	—	>15.79
Mg II	>13.78	$13.87^{+0.13}_{-0.13}$	—	$13.87^{+0.13}_{-0.13}$
Al II	<13.07	—	—	<13.07
Al III	>14.10	$14.27^{+0.13}_{-0.13}$	—	$14.27^{+0.13}_{-0.13}$
Si III	>14.27	>14.35	>14.38	$>14.38^{b}_{-0.11}$
Si IV	>15.17	>15.44	>15.40	>15.40
P V	>15.18	$15.33^{+0.05}_{-0.05}$	$15.47^{+0.15}_{-0.10}$	$15.47^{+0.15}_{-0.10}$
S IV	>15.53	$15.48^{+0.07}_{-0.10}$	$15.60^{+0.04}_{-0.05}$	$15.60^{+0.04}_{-0.05}$
S IV*	>15.35	$15.40^{+0.07}_{-0.12}$	$15.39^{+0.10}_{-0.10}$	$15.39^{+0.10}_{-0.10}$

[a]Adopted value for photoionization modelling (see text).
[b]We use the difference between the Si III AOD and PC measurements as a lower error on the Si III lower limit.

Table 3.3: Number density measurements. The values correspond to the horizontal error-bars in Figure 3.4.4.

	AOD	PC(v)	Adopted
$\log(n_e)$	$4.47^{+0.21}_{-0.18}$	$4.36^{+0.19}_{-0.16}$	$4.42^{+0.26}_{-0.22}$

in Ferland et al. (2013). We assume a plane-parallel geometry for a gas of constant $n_{\rm H}$ and initially choose solar abundances and the UV-Soft SED which is a good representation of radio-quiet quasars (described in Section 4.2 of Dunn et al., 2010, other SEDs and metallicities will be explored in Section 3.5.2 here). For the chosen SED and metallicity, we generate a grid of models by varying $N_{\rm H}$ and $U_{\rm H}$. Ionic column densities ($N_{\rm ion}$) predicted by the models are tabulated and compared with the measured values in order to determine the models that best reproduce the measured $N_{\rm ion}$. For a more elaborate description of this method, see Borguet et al. (2013); Arav et al. (2013).

3.5.1 Photoionization solution

In Figure 3.5.1, contours where model predictions match the measured $N_{\rm ion}$ are plotted in the $N_{\rm H}-U_{\rm H}$ plane. Note that Figure 3.5.1 presents models for two different metallicity values ($1{\rm Z}_\odot$ and $4{\rm Z}_\odot$, see discussion in Section 3.5.2). The ionic column densities used in the photoionization modelling are listed in the last column of Table 3.4.4, consisting of the PC measurements where available and with PC(v) prioritized over PC. In Figure 3.5.1, we show only the ions which dominate the solution; the lower limits (H I, C IV, N V and Si IV) and upper limits (He I*, C II and Al II) are trivially satisfied by the contraints of Al III and S IV. The Mg II contour lies between the Al III and S IV contours, and is thus also satisfied.

For $Z = 1{\rm Z}_\odot$, the P V contour requires a higher $N_{\rm H}$ than the S IV contour in regions also satisfied by the Si III lower limit (above the dashed line in Figure 3.5.1). This over-prediction of the S IV column density will be discussed in Section 3.6.2. The solution is also influenced by the Al III contour which lies parallel to S IV. This results in a poor fit ($\chi^2_{\rm red}$=10.6), since no models can simultaneously predict the observed S IV and Al III column denisties.

Figure 3.4: Phase plot showing the photoionization solution using the UV-Soft SED for gas with one and four times solar metallicity. Each colored contour represents (for one of the two metallicities) the locus of models (U_H, N_H) which predict a column density consistent with the observed column density for that ion. The bands which span the contours are the 1-σ uncertainties in the measured observations. The dashed line indicates the Si III lower limit. For each metallicity, the black "X" is the best ionization solution and is surrounded by the χ^2 contour (see text).

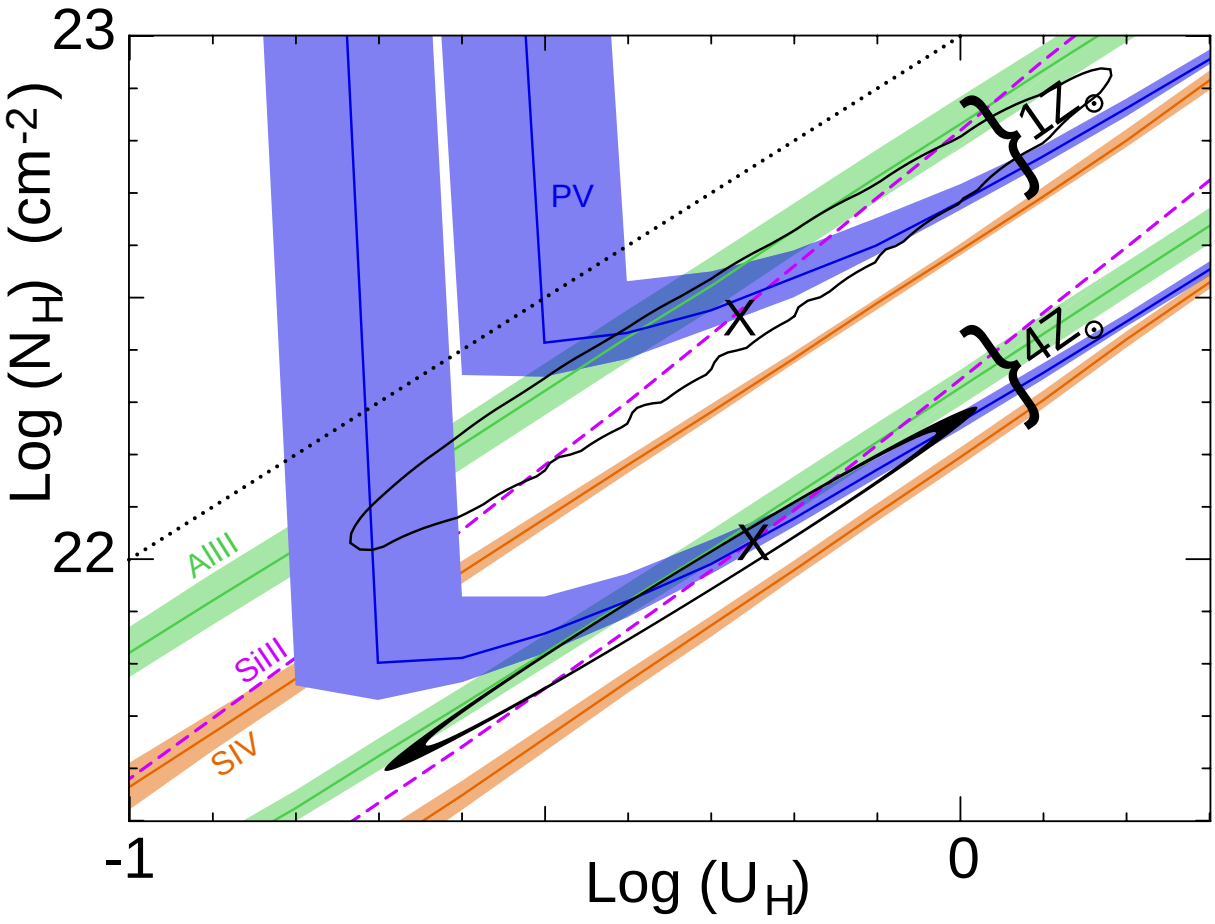

Figure 3.5: **(top)** Phase plot showing the photoionization solution for three SEDs (HE0238, MF87 and UVsoft, see descriptions in Arav et al. 2013) and two metallicities (one solar (Z1) and four solar (Z4)) for a total of six models. Contours of equal $\dot{E}_{\rm k}/L_{\rm Edd}$ (assuming fixed $n_{\rm H}$) are shown as parallel, thin solid lines assuming the UV-Soft SED (see text). **(bottom)** Same as above, but with the horizontal axis converted to distance, which incorporates the errors on $n_{\rm H}$ and $U_{\rm H}$ into the horizontal errors on R.

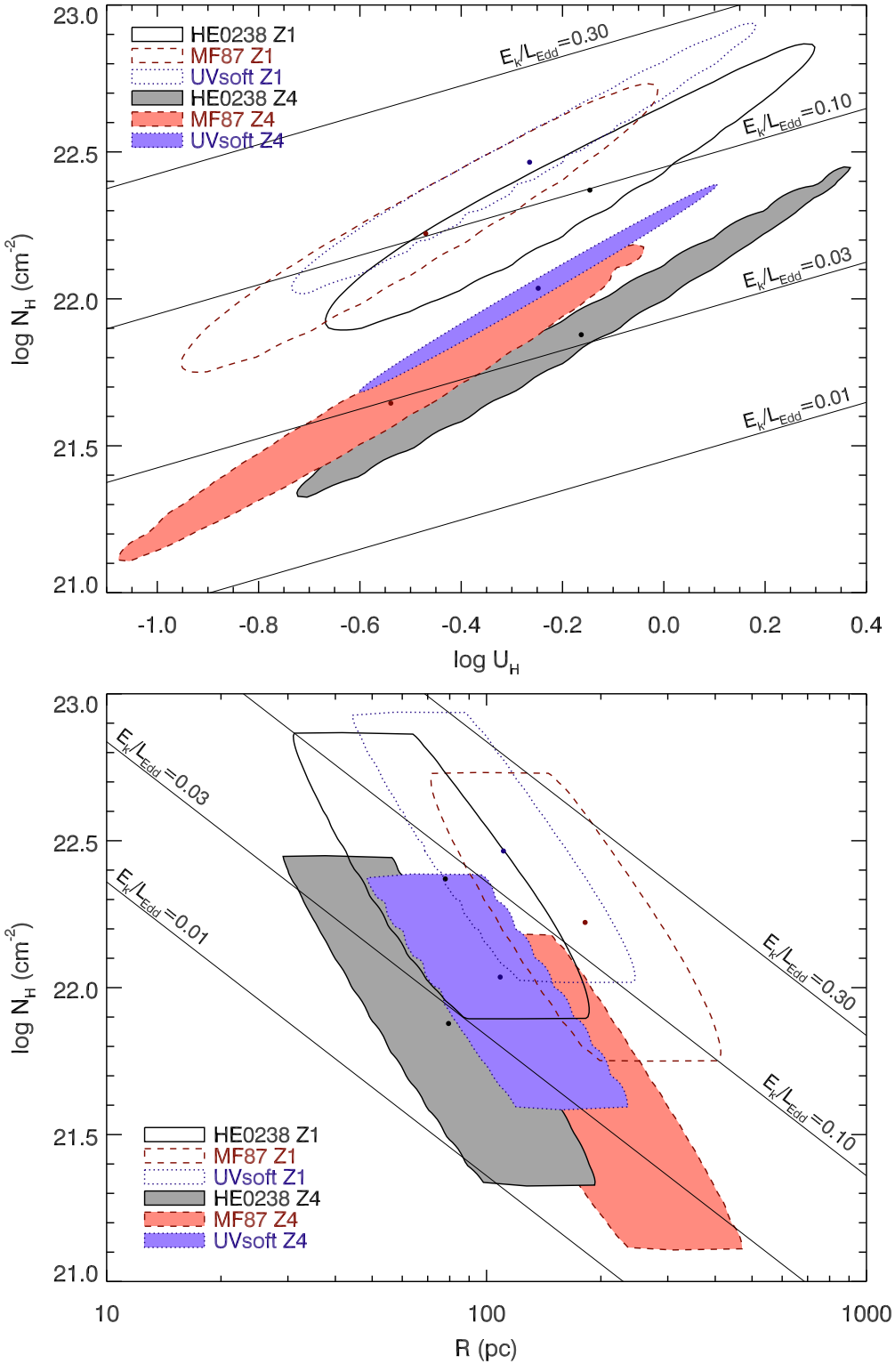

Table 3.4: Properties of the chosen SEDs.

SED	HE0238	MF87	UV-Soft
$\log(L_{\rm Bol})$ (erg s^{-1})	46.79	47.03	46.87
$\log(Q_{\rm H})$ (s^{-1})	56.53	56.95	56.72

3.5.2 Dependence on SED and metallicity

We consider the sensitivity of the photoionization solution to our choice of SED and metallicity by following the approach of Arav et al. (2013), thereby allowing for comparison with previous outflows under the same set of assumptions. We find the photoionization solution in six different cases (three SEDs from Arav et al. 2013 each with $1Z_\odot$ and $4Z_\odot$), plot the χ^2 contours in the top panel of Figure 3.5.1 and report the solutions in Table 3.6.1. The change in metallicity from $1Z_\odot$ to $4Z_\odot$, scaled according to the Cloudy starburst schema (following grid M5a of Hamann & Ferland, 1993), has the same effect with each SED, decreasing the $\log(N_{\rm H})$ of the solution by 0.4 dex. This is illustrated in Figure 3.5.1, which shows the photoionization solution for metallicities of both $Z = 1Z_\odot$ and $Z = 4Z_\odot$. We will discuss alternative elemental abundances in Section 3.6.2; here we consider the same metallicities used for other outflows studied by our group.

The different SEDs we use spread the solution over 0.4 dex in $\log(U_{\rm H})$, which is comparable to the errors on each solution. In Table 3.5.2 we report $Q_{\rm H}$ as well as the bolometric luminosity $L_{\rm Bol}$ for the three SEDs by fitting them to the measured flux (corrected for Galactic reddening) at 1100 Å (in the rest-frame) and integrating over the whole energy range.

One important motivation to find both the ionization parameter $U_{\rm H}$ and the number density $n_{\rm H}$ is to determine the distance of the outflow R from Equation (3.3). We therefore convert the ionization parameter $\log(U_{\rm H})$ to distance R using Equation (3.3) and present the same six photoionization solutions in the bottom panel of Figure 3.5.1. The uncertainties on $U_{\rm H}$ and $n_{\rm H}$ are incorporated into our value for R, which forms the horizontal spread of the contours in Figure 3.5.1. Since $N_{\rm H}$ is not involved in the distance determination, the vertical spread

of the contours in Figure 3.5.1 remains unchanged. In both panels of Figure 3.5.1, we also show the contours of equal $\dot{E}_{\rm k}/L_{\rm Edd}$ (see Section 3.6.1) assuming the UV-Soft SED, noting that the same contours for the different SEDs are shifted in $\log(N_{\rm H})$ by no more than 0.1 dex.

3.6 Results and discussion

3.6.1 Energetics

Assuming the outflow is in the form of a thin partial shell, its mass flow rate ($\dot{M}$) and kinetic luminosity ($\dot{E}_{\rm k}$) are given by (see Borguet et al., 2012b, for discussion)

$$\dot{M} = 4\pi R\Omega\mu m_p N_H v \tag{3.4}$$

$$\dot{E}_{\rm k} = 2\pi R\Omega\mu m_p N_H v^3 \tag{3.5}$$

where R is the distance from the outflow to the central source, Ω is the global covering fraction of the outflow, $\mu = 1.4$ is the mean atomic mass per proton, m_p is the mass of the proton, N_H is the total hydrogen column density of the absorber, and v is the radial velocity of the outflow. Using the parameters reported in the preceeding sections, we calculate the energetics for the six models we have considered for the S IV outflow of SDSS J0831+0354 and report the relevant values in the first six rows of Table 3.6.1 (the other four rows are comparison outflows that will be discussed in Section 3.6.3). We adopt the UV-Soft SED with $Z = 4{\rm Z}_{\odot}$ as our representitive model for this outflow, which is the same model chosen in Paper I, and yields a conservative measurement of $\dot{E}_{\rm k}$. As in Paper I, we use $\Omega = 0.08$, which is appropriate for S IV BAL outflows.

As noted in the Introduction, an $\dot{E}_{\rm k}$ value of at least 0.5% (Hopkins & Elvis, 2010) or 5% (Scannapieco & Oh, 2004) of the Eddington luminosity ($L_{\rm Edd}$) is deemed sufficient to produce significant AGN feedback effects. We determine the Eddington luminosity $L_{\rm Edd} = 10^{47.0}$ erg s^{-1} from the mass of the SMBH (e.g. using Equation (6.21) of Krolik (1999)). The

mass of the SMBH is determined using the virial mass estimator from Equation (3) of (Park et al., 2013, given the caveat that the scaling relationship extrapolated to high-z/luminosity quasars is not yet firmly established). This estimate requires the continuum luminosity at rest-frame 1350Å and the FWHM of the C IV BEL, both of which are directly measured from our spectrum. We use this method to determine $L_{\rm Edd}$ for the quasars SDSS J1106+1939 and SDSS J0838+2955. The C IV BEL in SDSS J0318-0600 is not well-defined, so we perform a similar analysis using the Mg II BEL and Equation (1) of Vestergaard & Osmer (2009). The only spectral coverage of HE 0238-1904 is in the extreme-UV, which does not cover any diagnostic lines sufficient for this method. We therefore use the assertion (from Section 9 of Arav et al., 2013) that the Eddington luminosity is approximately the bolometric luminosity for our comparison in Table 3.1.

We note that recent studies (Luo et al., 2014) have found X-ray weak SEDs for BALQSO that are much softer than the UVsoft SED we use here. To explore the effects of such an SED on our results, we constructed an SED from the object in Luo et al. (2014) showing the most extreme X-ray softness (PG 1254+047) by interpolating between the given flux points (see right-centre panel of Figure 3 of Luo et al., 2014). At 2 keV the flux is three orders of magnitude lower than in our UVsoft SED. The photoionization solution for this very soft SED leads to a distance of 51 pc and $\dot{E}_{\rm k}$=$10^{44.9}$erg s^{-1} for the outflow using Z=4Z$_{\odot}$. This distance and energy is lower by a factor of two and six respectively, compared to the values obtained with the UVsoft SED (110 pc, $\dot{E}_{\rm k}$=$10^{45.7}$erg s^{-1}) for Z=4Z$_{\odot}$.

We caution that the cause of the observed X-ray weakness can be attributed to optically thick absorption from the outflow itself, rather than intrinsically weak X-ray emission or obscuration between the central source and the outflow. If this is the case, then the SED incident on the outflow would likely resemble one of the other SEDs presented here. It is the incident radiation that will determine the photoionization solution.

Table 3.5: Physical properties of energetic quasar outflows (object names abbreviated from Table 3.1).

Object, SED	$\log(L_{\rm Bol})$ (erg s^{-1})	v (km s^{-1})	$\log(U_H)$	$\log(N_H)$ (cm^{-2})	$\log(n_{\rm e})$ (cm^{-3})	R (pc)	$\dot{M}$ ($M_\odot$yr^{-1})	$\log(\dot{E}_k)$ (erg s^{-1})	$\dot{E}_k/L_{\rm Edd}$ (%)
J0831 HE0238 Z1	46.8	-10800	$-0.15^{+0.4}_{-0.5}$	$22.4^{+0.5}_{-0.5}$	$4.42^{+0.26}_{-0.22}$	78^{+27}_{-18}	230^{+330}_{-130}	$45.9^{+0.4}_{-0.3}$	$8^{+11}_{-4.4}$
J0831 MF87 Z1	47.0	-10800	$-0.47^{+0.5}_{-0.5}$	$22.2^{+0.5}_{-0.5}$	$4.42^{+0.26}_{-0.22}$	180^{+53}_{-44}	390^{+570}_{-220}	$46.1^{+0.4}_{-0.4}$	$13^{+19}_{-7.5}$
J0831 UVsoft Z1	46.9	-10800	$-0.26^{+0.4}_{-0.5}$	$22.5^{+0.5}_{-0.4}$	$4.42^{+0.26}_{-0.22}$	110^{+30}_{-25}	410^{+530}_{-220}	$46.2^{+0.4}_{-0.3}$	$14^{+18}_{-7.7}$
J0831 HE0238 Z4	46.8	-10800	$-0.16^{+0.5}_{-0.6}$	$21.9^{+0.6}_{-0.6}$	$4.42^{+0.26}_{-0.22}$	79^{+33}_{-24}	76^{+120}_{-46}	$45.4^{+0.4}_{-0.4}$	$2.6^{+4.2}_{-1.6}$
J0831 MF87 Z4	47.0	-10800	$-0.54^{+0.5}_{-0.5}$	$21.6^{+0.5}_{-0.5}$	$4.42^{+0.26}_{-0.22}$	200^{+74}_{-54}	110^{+170}_{-66}	$45.6^{+0.4}_{-0.4}$	$3.8^{+5.8}_{-2.3}$
J0831 UVsoft Z4	46.9	-10800	$-0.25^{+0.3}_{-0.4}$	$22.0^{+0.4}_{-0.5}$	$4.42^{+0.26}_{-0.22}$	110^{+27}_{-15}	150^{+140}_{-84}	$45.7^{+0.3}_{-0.4}$	$5.2^{+4.8}_{-2.9}$
J1106 UVsoft Z4	47.2	-8250	$-0.5^{+0.3}_{-0.2}$	$22.1^{+0.3}_{-0.1}$	$4.1^{+0.02}_{-0.37}$	320^{+200}_{-100}	390^{+300}_{-10}	$46.0^{+0.3}_{-0.1}$	$12^{+11}_{-0.3}$
HE 0238-1904 Z4[a]	47.2	-5000	$0.5^{+0.1}_{-0.1}$	$20.0^{+0.1}_{-0.1}$	$3.83^{+0.10}_{-0.10}$	3400^{+2000}_{-490}	140^{+80}_{-40}	$45.0^{+0.2}_{-0.2}$	$0.7^{+0.5}_{-0.2}$
SDSS J0838+2955	47.5	-5000	$-2.0^{+0.2}_{-0.2}$	$20.8^{+0.3}_{-0.3}$	3.8	3300^{+1500}_{-1000}	300^{+210}_{-120}	$45.4^{+0.2}_{-0.2}$	$2.3^{+1.5}_{-0.8}$
SDSS J0318-0600	47.7	-4200	-3.1	19.9	3.3	6000	120	44.8	0.13

[a]For the high-ionization phase of trough B.

3.6.2 The S IV discrepancy

Our photoionization solution (for the UV-soft SED) over-predicts the S IV total column density by a factor of eight, which is not alleviated appreciably by changing the SED or metallicity. We offer two resolutions to this discrepancy: a two-phase solution, or individual abundance scaling of sulphur.

1) Arav et al. (2013) showed that two ionization phases exist in some outflows (in that case smaller, denser cloudlets embedded in high-ionization gas with much larger $N_{\rm H}$), and can account for the appearence of low-ionization species that are inconsistent with the ionization solution obtained from higher-ionization species. S IV and P V are both high-ionization species, thus their column densities can be produced in a separate phase than the low-ionization species (Mg II and Al III). The S IV and P V contours in Figure 3.5.1 converge at high ionization parameters ($\log U_{\rm H}$>0.3). A high-ionization phase at this ionization parameter would satisfy both the S IV and P V constraints, but under-predict the Mg II and Al III column densities, which would need to be satisfied by a low-ionization solution. A two-phase solution could resolve the S IV discrepancy, but such a solution is not well-constrained with the measurements obtained from our spectra. However, any high-ionization solutions that adhere to the P V constraint would move towards the upper-right corner of Figure 3.5.1. Since $\dot{E}_{\rm k} \propto N_{\rm H}/\sqrt{U_{\rm H}}$, this increase in both $U_{\rm H}$ and $N_{\rm H}$ by 0.6 dex would result in an increase

in $\dot{E}_{\rm k}$ of 0.3 dex.

2) The discrepancy between S IV and the other ions may be alleviated by considering a higher metallicity, as outflows are known to have supersolar metallicities (e.g. Gabel, Arav & Kim, 2006; Arav et al., 2007). In our Cloudy models the discrepancy persists with different metallicities since the abundance scaling schema from grid M5a of Hamann & Ferland (1993) does not increase the relative [S/P] or [S/Al] abundances. An alternative enrichment model that results in [S/P]=-0.9 and [S/Al]=-0.9 for a certain metallicity would decrease the S IV column density predicted by the solution from the P V and Al III constraints by a factor of eight, thus eliminating the discrepancy that appeared in the solar abundances case. Considering the absence of a complete AGN abundance scaling model, this solution is not as implausible as it seems; e.g. Ballero et al. (2008) derives relative abundances such as [Si/C]=0.83 for $Z = 7.22{\rm Z}_{\odot}$.

If neither of these scenarios apply, then we conclude that the S IV column density is indeed a factor of eight higher than was measured from the S IV and S IV* troughs, and one or both of the troughs must be saturated. S IV* cannot be saturated since its trough is shallower than S IV (see discussion in Section 6.3 of Paper I), thus the true S IV column density increases by a factor of eight, and the S IV*/S IV column density ratio decreases by the same factor. This correction would decrease $n_{\rm e}$ by an order of magnitude (see Figure 3.4.4), which would increase R by a factor of three (see Equation (3.3)), and increase $\dot{M}$ and $\dot{E}_{\rm k}$ by a factor of three (see Equation (3.5)). Although this effect would enhance the energetics of the outflow, we suspect that S IV is not saturated since the depth of S IV λ1062.66 is shallower than either line from the P V doublet which is presumed much closer to saturation. As S IV and P V are both high-ionization ions, we assume that they have similar covering factors and thus their absorption lines would be the same depth if saturated.

3.6.3 Comparison with other outflows

In Table 3.6.1 we also list four other outflows with the highest $\dot{E}_{\rm k}$ determined by our group. Two of these are low-ionization BALs that appear in SDSS J0838+2955 (Moe et al., 2009) and SDSS J0318-0600 (Dunn et al., 2010), and their distance estimate is based on singly ionized species. This introduces an uncertainty (see Section 3.2 for discussion) that can be alleviated by utilizing metastable levels from high-ionization ions such as S IV/S IV*.

The first object to show a large kinetic luminosity ($\dot{E}_{\rm k}$=10^{46} erg s^{-1}) using S IV/S IV* absorption was SDSS J1106+1939 (Paper I). The outflow we study in this paper (SDSS J0831+0354) is the second such example, and it exhibits properties similar to SDSS J1106+1939, albeit at one-third the distance to the quasar. In a cursory examination of the objects to be analyzed in our VLT/X-shooter survey, at least two additional BAL outflows show S IV/S IV* troughs.

Arav et al. (2013) also used the excited state from a high-ionization ion (O IV/O IV*) to determine the energetics of an outflow from quasar HE 0238-1904. Although the outflow did not show absorption from low-ionization ions, absorption from the very-high-ionization ions Ne VIII and Mg X confirmed the existence of a high-ionization phase. As discussed in the previous section, the S IV and P V absorption in SDSS J0831+0354 could originate from a separate ionization phase, but we cannot confirm its existence without absorption data from additional high-ionization ions.

3.6.4 Distance of quasar outflows from the central source

The outflow of SDSS J0831+0354 lies closer to the central source than the other outflows listed in Table 3.6.1. However, this distance ($R \sim 100$ pc) is three orders of magnitude greater than the trough forming region (0.01–0.1 pc) for accretion disk line-driven winds (e.g. Figure (3) of Murray et al., 1995; Proga, Stone & Kallman, 2000). This large empirical distance scale is not limited to high $\dot{E}_{\rm k}$ outflows. The large majority of measured distances

to BAL (and narrower) outflows that were deduced using troughs from excited states yield distances between 10–10,000 pc (de Kool et al., 2001; Hamann et al., 2001; de Kool et al., 2002b,a; Moe et al., 2009; Dunn et al., 2010; Bautista et al., 2010; Aoki et al., 2011; Edmonds et al., 2011; Borguet et al., 2012b,a, 2013; Arav et al., 2013; Lucy et al., 2014). Two outflow components are found to be between 1–10 pc from the central source (de Kool et al., 2002b,a). The discrepancy between the empirical distances and those inferred from accretion disk line-driven winds models suggests that the latter models are not applicable to the trough formation of quasar outflows.

3.6.5 Reliability of measurements

Our group (Arav, 1997; Arav et al., 1999b,a, 2001a,b; Arav, Korista & de Kool, 2002; Arav et al., 2003; Scott et al., 2004; Gabel et al., 2005a) and others (Barlow, Hamann & Sargent, 1997; Hamann et al., 1997; Telfer et al., 1998; Churchill et al., 1999; Ganguly et al., 1999) showed that column densities derived from the apparent optical depth (AOD) analysis of BAL troughs are unreliable when non-black saturation occurs in the troughs. For this reason, we use partial covering (PC) absorption models in this analysis.

It is instructive to assess quantitatively the difference in $\dot{E}_{\rm k}$ that arises from using these two absorption models on our results. To this end we re-determine the photoionization solution using the AOD measurements for P V, Si III, Al III and S IV (i.e. from the first column of Table 3.4.4). The resulting kinetic luminosity of $\dot{E}_{\rm k}$=$10^{45.6}$ erg s^{-1} for the UV-Soft 4Z$_\odot$ model differs only slightly from the $\dot{E}_{\rm k}$=$10^{45.7}$ erg s^{-1} that we derive using the PC template. Thus, our results are rather insensitive to the method of column density extraction.

In Table 3.6.5 we demonstrate that almost all possible deviations from our representative model (UV-Soft SED, $Z = 4{\rm Z}_\odot$, one ionization component, unsaturated Si III absorption) results in a higher $\dot{E}_{\rm k}$ for the SDSS J0831+0354 outflow. Even with $\dot{E}_{\rm k}$ lowered by assuming a different SED, the minimum energy allowed by our analysis is $\dot{E}_{\rm k}/L_{\rm Edd} = 2.6\%$ for the HE0238 SED with $Z = 4{\rm Z}_\odot$ (see Table 3.6.1).

Table 3.6: Sensitivity of derived energetics to input changes.

Assumption	Effect(s)	Outcome	Reference
N(Si III)> $N_{\rm AOD}$	higher $N_{\rm H}$, lower $U_{\rm H}$	higher $\dot{E}_{\rm k}$	Section 3.5.1
$Z < 4{\rm Z}_{\odot}$	higher $N_{\rm H}$	higher $\dot{E}_{\rm k}$	Figure 3.5.1
different SED	lower $N_{\rm H}$	lower $\dot{E}_{\rm k}$	Figure 3.5.1
$\Omega > 0.08$	—	higher $\dot{E}_{\rm k}$	Equation (3.5)
two phases	higher $N_{\rm H}$, higher $U_{\rm H}$	higher $\dot{E}_{\rm k}$	Section 3.6.2
S IV* saturated	lower $n_{\rm H}$, higher R	higher $\dot{E}_{\rm k}$	Section 3.6.2

3.7 Summary

We present the analysis of BALQSO SDSS J0831+0354 using data obtained with VLT/X-shooter. Our main findings are as follows:

1. The BAL outflow in SDSS J0831+0354 has a velocity of 10,800 km s^{-1} in the rest frame of the quasar with a width of 3500 km s^{-1} and shows kinematically connected absorption from the high-ionization species S IV and S IV*. The ratio of the excited column density to ground was used to determine the number density of the outflow to be log ($n_{\rm e}$)=4.42±0.24 cm^{-3}.

2. The non-black saturation of the P V doublet indicated that the absorber was inhomogenously distributed across the emission source. The saturation of the P V doublet resulted in a high ionic column density which, combined with the low elemental abundance of phosphorous, necessitates a high total hydrogen column density ($N_{\rm H}$).

3. Variations of the incident SED had only a small effect on the ionization solution ($U_{\rm H}$,$N_{\rm H}$) of the outflow, while an increased metallicty of 4Z$_{\odot}$ lowered the required hydrogen column density by 0.4 dex. The UV-soft SED with Z=4Z$_{\odot}$ was adopted as the representative model, and the hydrogen column density was determined to be

log ($N_{\rm H}$)=22.0±0.4 cm^{-2} with an ionization parameter of log ($U_{\rm H}$)=-0.25±0.3.

4. The outflow was determined to be located 110 pc from the central source and contained a kinetic luminosity of 5.2% of the Eddington luminosity of the quasar. We establish half of this value (2.6%) as a conservative lower limit. This large kinetic luminosity makes the outflow of SDSS J0831+0354 a candidate for quasar-mode AGN feedback effects seen in simulations (e.g. Hopkins et al., 2006; Ostriker et al., 2010).

Acknowledgement

We acknowledge support from NASA STScI grants GO 11686 and GO 12022 as well as NSF grant AST 1413319.

Chapter 4

Anatomy of the AGN in NGC 5548: II. The spatial, temporal, and physical nature of the outflow from HST/COS Observations

4.1 Abstract

Context. AGN outflows are thought to influence the evolution of their host galaxies and of super massive black holes. Our deep multiwavelength campaign on NGC 5548 has revealed a new, unusually strong X-ray obscuration, accompanied by broad UV absorption troughs observed for the first time in this object. The X-ray obscuration caused a dramatic decrease in the incident ionizing flux on the outflow that produces the long-studied narrow UV absorption lines in this AGN. The resulting data allowed us to construct a comprehensive physical, spatial, and temporal picture for this enduring AGN wind.

Aims. We aim to determine the distance of the narrow UV outflow components from the central source, their total column-density, and the mechanism responsible for their observed absorption variability.

Methods. We study the UV spectra acquired during the campaign, as well as from four previous epochs (1998-2011). Our main analysis tools are ionic column-density extraction techniques, photoionization models based on the code CLOUDY, and collisional excitation simulations.

Results. A simple model based on a fixed total column-density absorber, reacting to changes in ionizing illumination, matches the very different ionization states seen in five spectroscopic epochs spanning 16 years. The main component of the enduring outflow is situated at 3.5±1.1 pc from the central source, and its distance and number density are similar to those of the narrow-emitting-line region in this object. Three other components are situated between 5-70 pc and two are farther than 100 pc. The wealth of observational constraints and the anti-correlation between the observed X-ray and UV flux in the 2002 and 2013 epochs make our physical model a leading contender for interpreting trough variability data of quasar outflows.

Conclusions. This campaign, in combination with prior UV and X-ray data, yields the first simple model that can explain the physical characteristics and the substantial variability observed in an AGN outflow.

4.2 Introduction

AGN outflows are detected as blueshifted absorption troughs with respect to the object systemic redshift. Such outflows in powerful quasars can expel sufficient gas from their host galaxies to halt star formation, limit their growth, and lead to the co-evolution of the size of the host and the mass of its central super massive black holes (e.g., Ostriker et al., 2010; Hopkins & Elvis, 2010; Soker & Meiron, 2011; Ciotti, Ostriker & Proga, 2010; Faucher-

Giguère, Quataert & Murray, 2012; Borguet et al., 2013; Arav et al., 2013). Therefore, deciphering the properties of AGN outflows is crucial for testing their role in galaxy evolution.

Nearby bright AGN are excellent laboratories for studying these outflows because they yield: a) high-resolution UV data, which allow us to study the outflow kinematics and can yield diagnostics for their distance from the central source; and b) high-quality X-ray spectra that give the physical conditions for the bulk of the outflowing material (e.g., Steenbrugge et al., 2005; Gabel et al., 2005b; Arav et al., 2007; Costantini et al., 2007; Kaastra et al., 2012). Thus, such observations are a vital stepping stone for quantifying outflows from the luminous (but distant) quasars, for which high-quality X-ray data are not available.

For these reasons, we embarked on a deep multiwavelength campaign on the prototypical AGN outflow seen in the intensively studied Seyfert 1 galaxy NGC 5548. For the past 16 years, this outflow has shown six kinematic components in the UV band (labeled in descending order of velocity, following Crenshaw et al., 2003), and their associated X-ray warm absorber (WA). We note that there is kinematic correspondence between the six UV components and the deduced WA components (see Section 4.6.1). Our 2013 campaign revealed a new X-ray obscurer accompanied by broad UV absorption (analyzed in Kaastra et al., 2014). The appearance of the obscurer allows us to derive a comprehensive physical picture of the long-term observed outflow, which we report here.

The plan of the paper is as follows. In Section 4.3 we describe the observations and data reduction; in Section 4.4 we analyze the key component of the outflow; in Section 4.5 we discuss the remaining five components; in Section 4.6 we connect the results of the UV analysis with those of the X-ray warm absorber of the same outflow; and in Section 4.7 we compare our results with previous studies, discuss the implication of our results to the variability of AGN outflow troughs in general, and elaborate on the connection between the X-ray obscurer and the persisting outflow; in Section 4.8 we summarize our results.

4.3 Observations and data reduction

Our 2013 multiwavelength campaign on NGC 5548 included coordinated observations using *XMM-Newton*, the *Hubble* Space Telescope (HST), *Swift*, INTEGRAL, and NuSTAR. The overall structure of the campaign was described in Kaastra et al. (2014). A full log of all the observations is given by Mehdipour et al. (2015). Here we present a detailed analysis of the UV observations we obtained using the Cosmic Origins Spectrograph (COS) (Green et al., 2012) onboard HST. We obtained five COS observations simultaneously with five of the *XMM-Newton* observations between 2013 June 22 and 2013 August 01. Each two-orbit observation used gratings G130M and G160M at multiple central wavelength settings and multiple focal-plane positions (FP-POS) to cover the wavelength range from 1132 Å to 1801 Å at a resolving power of ∼15,000. Table A lists the observation dates of the individual visits, the exposure times, and the continuum flux measured at 1350 Å in the rest frame, as well as corresponding information for archival HST observations of NGC 5548 that are also used in this analysis. The five observations from June to August 2013 were optimally weighted to produce an average spectrum that we use for our analysis. Kaastra et al. (2014) describe the data reduction process from the calibration of the data to the production of this average spectrum.

The 2013 average HST/COS spectrum with all identified absorption features is shown in Figure A.1. As described in Kaastra et al. (2014), we modeled the emission from NGC 5548 using a reddened power law (with extinction fixed at $E(B-V) = 0.02$, Schlafly & Finkbeiner, 2011), weak Fe II emission longward of 1550 Å in the rest frame, broad and narrow emission lines modeled with several Gaussian components, blueshifted broad absorption on all permitted transitions in NGC 5548, and a Galactic damped Lyα absorption line. Using this emission model, we normalized the average spectrum to facilitate our analysis of the narrow intrinsic absorption lines in NGC 5548. Figure A.3 shows normalized spectra for absorption lines produced by Si III λ1206, Si IV $\lambda\lambda$1394, 1403, C IV $\lambda\lambda$1548, 1550, N V $\lambda\lambda$1238, 1242, and Lyα as a function of rest-frame velocity relative to a systemic redshift of $z = 0.017175$ (de

Vaucouleurs et al., 1991) via the NASA/IPAC extragalactic database (NED).

As shown in Table A, high-resolution UV spectra of NGC 5548 using HST cover an additional four epochs stretching back to 1998. We use the calibrated data sets for each of these observations as obtained from the Mikulski Archive for Space Telescopes (MAST) at the Space Telescope Science Institute (STScI). We compare the strengths of the narrow UV absorption troughs for each of these epochs with our new data set from 2013 in Figure A.2 and Figure A.3.

4.4 Physical and temporal characteristics of component 1

The key for building a coherent picture of the long-seen outflow is component 1: the strongest and highest velocity outflow component (centered at -1160 km s^{-1}). Due to the strong suppression of incident ionizing flux by the obscurer, the 2013 HST/COS data of component 1 show a wealth of absorption troughs from ions never before observed in the NGC 5548 outflow. These data allow us to decipher the physical characteristics of this component. In Section 4.4.1 we use the column-density measurements of P V, P III, Fe III, and Si II as input in photoionization models, and derive the total hydrogen column-density $N_{\rm H}$ for component 1, and its ionization parameter $U_{\rm H}$. In Section 4.4.2 we use the column-density measurements of C III* and Si III* to infer the electron number density $n_{\rm e}$, which combined with the value of the incident $U_{\rm H}$ yields a distance (R) between component 1 and the central source. In Section 4.4.3 we construct a simple model based on a fixed total column-density absorber, reacting to changes in ionizing illumination, that matches the very different ionization states seen in five HST high-resolution spectroscopic epochs spanning 16 years.

Figure 4.1: Intrinsic absorption features in the 2013 COS spectrum of NGC 5548. Normalized relative fluxes are plotted as a function of velocity relative to the systemic redshift of $z = 0.017175$, top to bottom: Si III λ1206, Si IV $\lambda\lambda$1394, 1403, C IV $\lambda\lambda$1548, 1550, N V $\lambda\lambda$1238, 1242, and Ly α, as a function of rest-frame velocity. For the doublets the red and blue components are shown in red and blue, respectively. Dotted vertical lines indicate the velocities of the absorption components numbered as in Crenshaw et al. (2003).

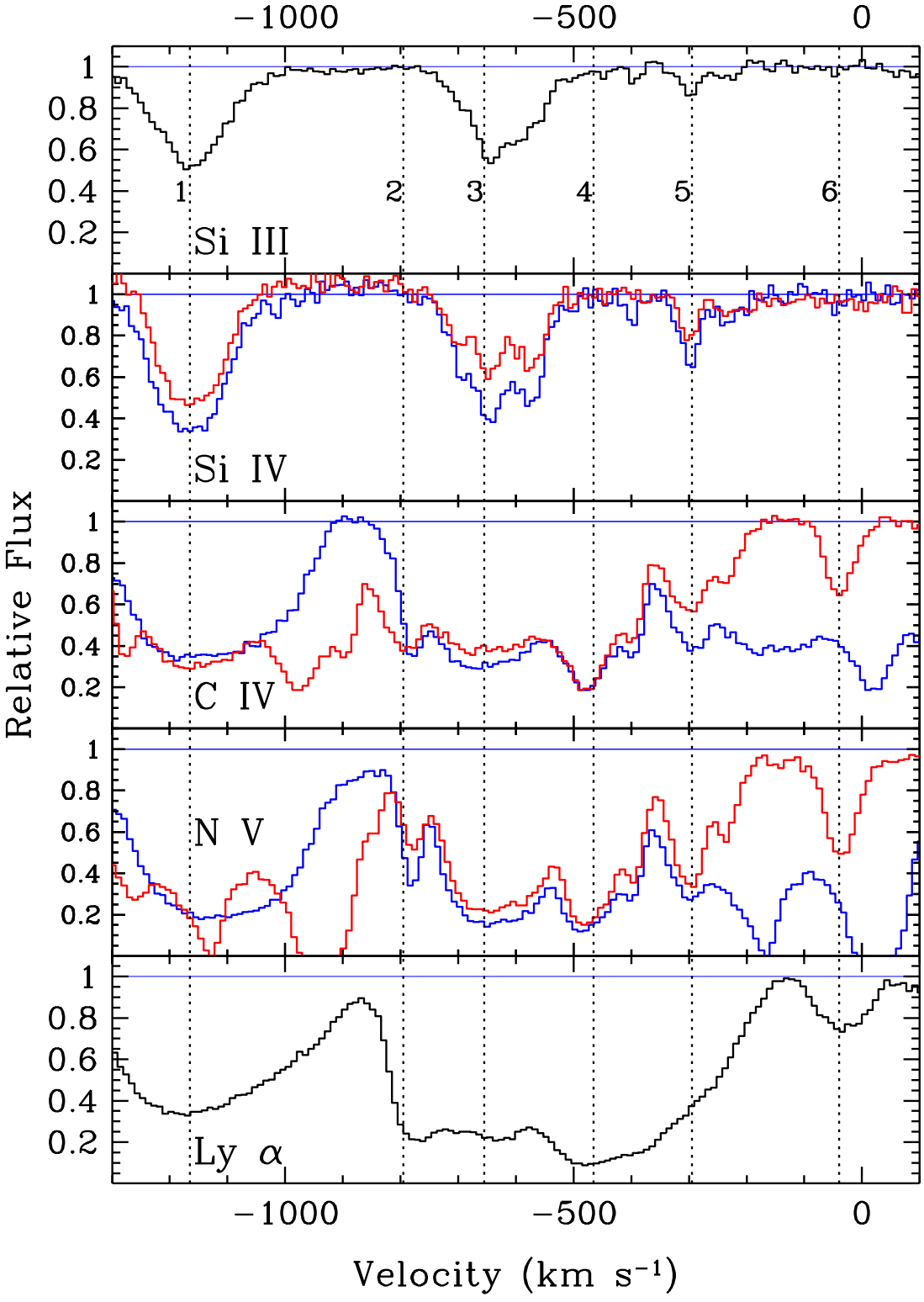

Figure 4.2: Adopted NGC 5548 SEDs. In black we show the SED for NGC 5548 in 2002 at an unobscured X-ray flux (hereafter "high SED", from Steenbrugge et al., 2005). In blue we show the SED appropriate to the 2013 epoch, where for the same flux at 1000 Å, the new X-ray obscurer reduced the ionizing flux by a factor of 17 between 1 Ry and 1 keV (obscured SED). The ionization potentials for destruction of some of the prominent observed species are shown by the vertical lines.

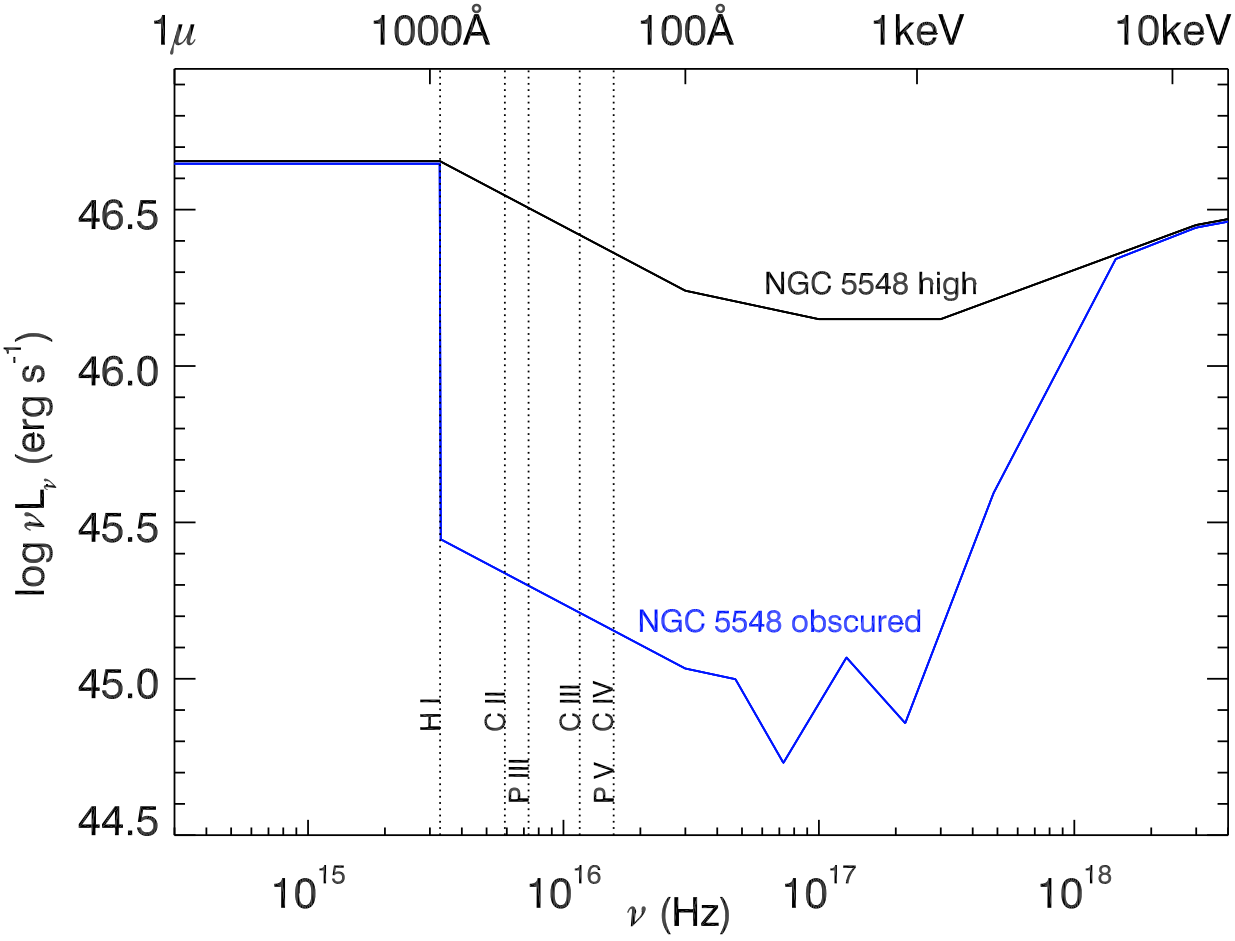

4.4.1 Total column-density $N_{\rm H}$ and ionization parameter $U_{\rm H}$

In the Appendix we describe the methods we use to derive the ionic column-densities ($N_{\rm ion}$) from the outflow absorption troughs. Table A gives the $N_{\rm ion}$ measurements for all observed troughs of all six outflow components in the five HST epochs (spanning 16 years) of high-resolution UV spectroscopy. The upper and lower limits were derived using the apparent optical depth (AOD) method. All the reported measurements were done using the partial overing (PC) method. We used the power-law (PL) method only on the C III* in order to quantify the systematic error due to different measuring methods (see Section 4.4.2).

The $N_{\rm ion}$ we measure are a result of the ionization structure of the outflowing material, and can be compared to photoionization models to determine the physical characteristics of the absorbing gas. As boundary conditions for the photoionization models, we need to specify the choice of incident spectral energy distribution (SED), and the chemical abundances of the outflowing gas.

We make the simple (and probably over-restrictive) assumption that the shape of the SED emitted from the accretion disk did not change over the 16 years of high-resolution UV spectroscopy. Specifically, we assume that the emitted SED has the same shape it had when we obtained simultaneous X-ray/UV observations in 2002 (the "high" SED in Figure 4.4, determined by Steenbrugge et al., 2005). In 2013 the obscurer absorbed much of the soft ionizing photon flux from this SED before it reached component 1. We model the incident SED on component 1 as the "obscured" SED in Figure 4.4, and further justify its specific shape in Section 4.4.3. For abundances, we use pure proto-Solar abundances given by Lodders, Palme & Gail (2009). The influence of the suppressed ionizing continuum on the photoionization solution is also discussed in Section 4.4.3.

With the choice of SED and chemical abundances, two main parameters govern the photoionization structure of the absorber: the total hydrogen column-density (N_H) and the

ionization parameter

$$U_H \equiv \frac{Q_{\rm H}}{4\pi R^2 n_{\rm H} c} \tag{4.1}$$

where $Q_{\rm H}$ is the rate of hydrogen-ionizing photons emitted by the object, c is the speed of light, R is the distance from the central source to the absorber and $n_{\rm H}$ is the total hydrogen number density. We model the photoionization structure and predict the resulting ionic column densities by self-consistently solving the ionization and thermal balance equations with version 13.01 of the spectral synthesis code Cloudy, last described in Ferland et al. (2013). We assume a plane-parallel geometry for a gas of constant $n_{\rm H}$.

To find the pair of ($U_{\rm H}$,$N_{\rm H}$) that best predicts the set of observed column-densities, we vary $U_{\rm H}$ and $N_{\rm H}$ in 0.1 dex steps to generate a grid of models (following the same approach described in Borguet et al., 2012b) and perform a minimization of the function

$$\chi^2 = \sum_i \left(\frac{\log(N_{i,\rm mod}) - \log(N_{i,\rm obs})}{\log(N_{i,\rm obs}) - \log\left(N_{i,\rm obs} \pm \sigma_i\right)} \right)^2 \tag{4.2}$$

where, for ion i, $N_{i,\rm obs}$ and $N_{i,\rm mod}$ are the observed and modeled column-densities, respectively, and σ_i is the error in the observed column-density. The measurement errors are not symmetric. We use the positive error ($+\sigma_i$) when $\log(N_{i,\rm mod}) > \log(N_{i,\rm obs})$ and the negative error ($-\sigma_i$) when $\log(N_{i,\rm mod}) < \log(N_{i,\rm obs})$.

The ionization solution for component 1 at the 2013 epoch is shown in Figure 4.4.1. We only show constraints from $N_{\rm ion}$ measurements, and note that all the lower limits reported in Table A are satisfied by this solution. We find $\log(N_{\rm H}) = 21.5^{+0.4}_{-0.2}$ cm^{-2}, and an ionization parameter of $\log(U_{\rm H}) = -1.5^{+0.4}_{-0.2}$, where the errors are strongly correlated as illustrated by the 1σ χ^2 contour.

4.4.2 Number density and distance

As shown in Figure 4.4.2, we detect absorption troughs from the C III* 1175 Å multiplet, arising from the metastable $3P_j$ levels of the 2s2p term. As detailed in Gabel et al. (2005b),

Figure 4.3: Photoionization phase plot showing the ionization solution for component 1 epoch 2013. We use the obscured SED and assumed proto-solar metalicity (Lodders, Palme & Gail, 2009). Solid lines and associated colored bands represent the locus of ($U_{\rm H}$,$N_{\rm H}$) models which predict the measured $N_{\rm ion}$, and their 1σ uncertainties. The black dot is the best solution and is surrounded by a 1σ χ^2 contour.

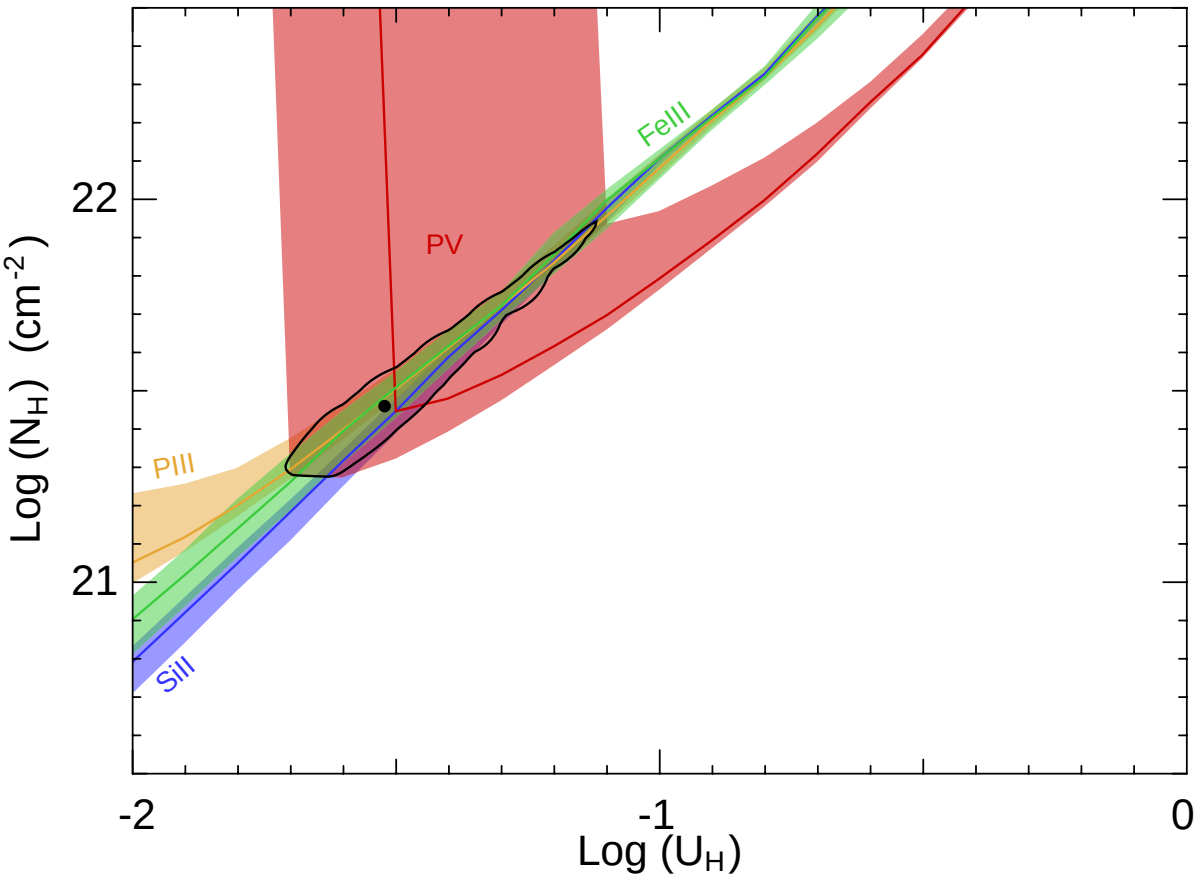

Figure 4.4: **a)** Absorption spectrum for the C III* 1175 Å multiplet. The 2013 COS spectrum shows clear and relatively unblended individual troughs from the J=2 and J=0 levels, but no contribution from the J=1 level that is populated at higher densities (see panel c). **b)** Absorption spectrum for the Si III* 1298 Å multiplet (similar in level structure to the C III* 1175 Å multiplet). The 2013 COS spectrum shows shallow but highly significant individual troughs from the J=2 and J=0 levels, but again no contribution from the J=1 level that is populated at higher densities. **c)** C III* and Si III* level population ratios, theory and measurements. The computed populations for the J=2/J=0 and J=1/J=0 are plotted as a function of electron number density for both ions (see text for elaboration). The crosses show the measured ratios for the J=2/J=0 ratio of both ions. From the C III* ratios we infer $\log(n_e) = 4.8 \pm 0.1$ cm^{-3}, where the error includes both statistical and systematic effects. This value is fully consistent with the one inferred from the Si III* ratio, where in the case of Si III* the statistical error is larger since the troughs are much shallower.

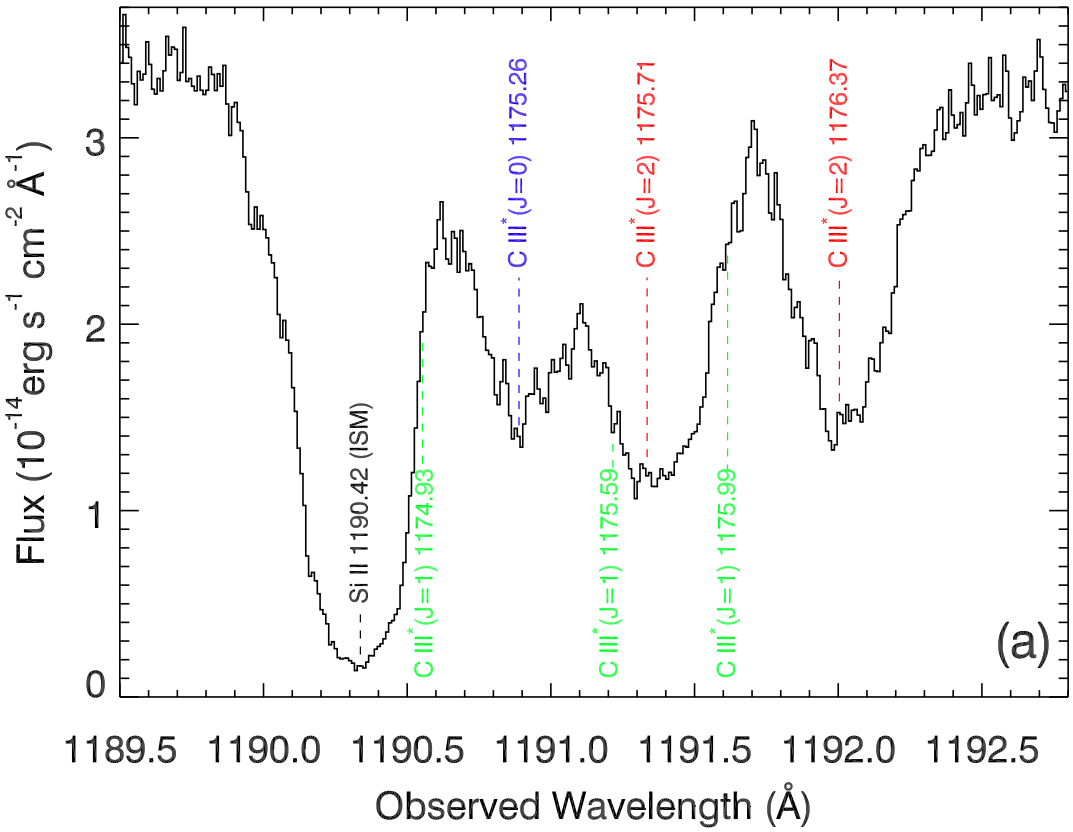

Figure 4.4: *continued*

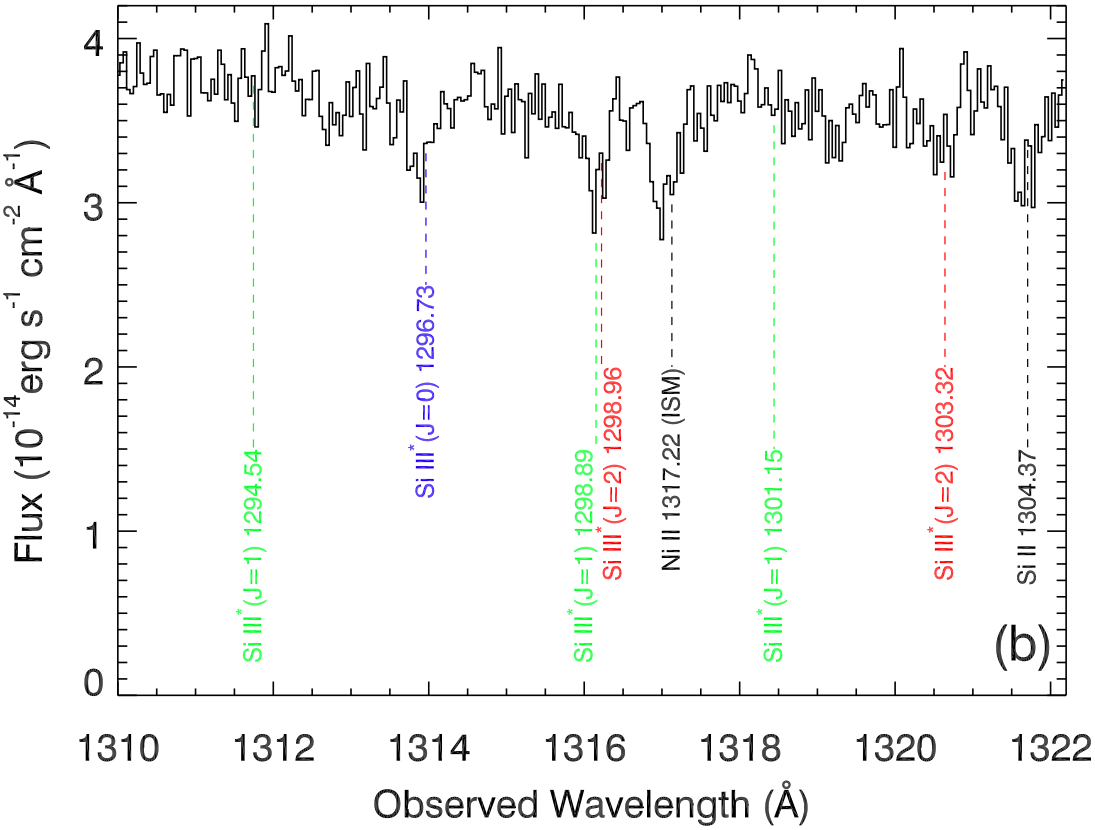

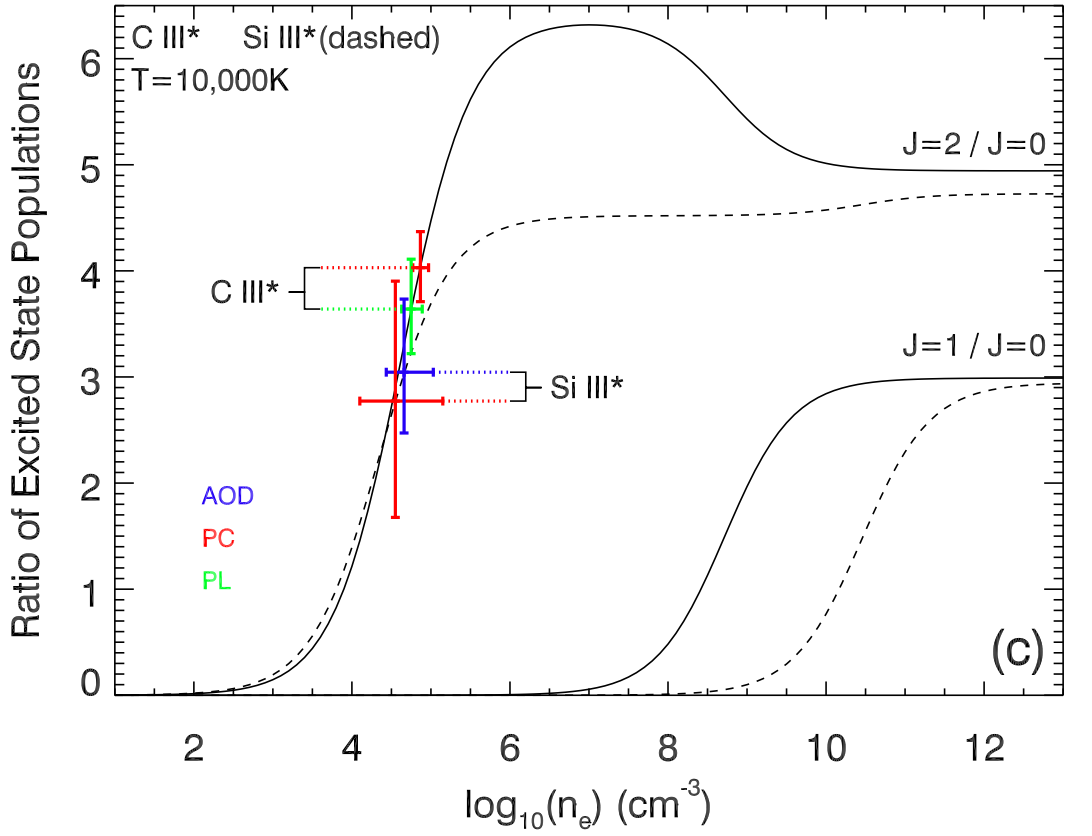

the excited C III* 1175 Å multiplet comprises six lines arising from three J levels. The J=0 and J=2 levels have significantly lower radiative transition probabilities to the ground state than the J=1 level and are thus populated at much lower densities than the latter. In particular, figure 5 in Borguet et al. (2012a) shows that the relative populations of the three levels are a sensitive probe to a wide range of n_e while being insensitive to temperature. The two high-S/N troughs from the J=2 level allow us to accurately account for the mild saturation in these troughs and therefore to derive reliable $N_{\rm ion}$ for both levels. From these measurements we infer $\log(n_{\rm e}) = 4.8 \pm 0.1$ cm^{-3} (see Figure 4.4.2). We also detect two shallow troughs from the same metastable level of Si III* (see panel b of Figure 4.4.2), which we use to measure an independent and consistent value for $n_{\rm e}$ (see panel c of Figure 4.4.2). The collisional excitation simulations shown in Figure 4.4.2c were performed using version 7.1.3 of CHIANTI (Dere et al., 1997; Landi et al., 2013), with a temperature of 10,000K (similar to the predicted temperature of our Cloudy model for component 1 during the 2013 epoch).

In addition to the C III* and Si III* troughs, the 2013 COS spectra of component 1 show several additional troughs from excited states: C II*, Si II*, P III*, Si II* and Fe III* (as well as their associated resonance transitions). Careful measurement of those troughs show that in these cases, the deduced $n_{\rm e}$ is a lower limit that is larger than the critical density of the involved excited and zero energy levels. In all cases the critical densities are below $\log(n_{\rm e}) = 4.8$ cm^{-3}, thus they are consistent with the $n_{\rm e}$ measurement we derive from the C III* and Si III* troughs.

As can be seen from the definition of the ionization parameter $U_{\rm H}$ (Equation (4.1)), knowledge of the hydrogen number density $n_{\rm H}$ for a given $U_{\rm H}$ and $N_{\rm H}$ allows us to derive the distance R. Our photoionization models show that for component 1, $\log(U_{\rm H}) = -1.5$ and since $n_{\rm e} \simeq 1.2 n_{\rm H}$ (as is the case for highly ionized plasma), $n_{\rm H} = 5.3 \times 10^4$ cm^{-3}. To determine the $Q_{\rm H}$ that affects component 1, we first calculate the bolometric luminosity using the average flux at 1350Å for visits 1-5 in 2013, the redshift of the object and the obscured SED (see Figure 4.4). We find $L_{\rm Bol}= 2.6 \times 10^{44}$ erg s^{-1} and from it, $Q_{\rm H} = 6.9 \times 10^{52}$ s^{-1}. Therefore,

Equation (4.1) yields $R = 3.5^{+1.0}_{-1.2}$ pc, where the error is determined from propagating the errors of the contributing quantities. We note that the distance and number density of component 1 are similar to those of the narrow-emitting-line-region (NELR) in this object. Using the variability of the narrow [O III]$\lambda\lambda$4959,5007 emission-line fluxes, Peterson et al. (2013) derive a radius of 1–3 pc and $n_{\rm e} \sim 10^5$ cm^{-3} for the NELR.

Roughly 50% of all Seyfert 1 galaxies show evidence for absorption outflows (Crenshaw et al., 1999). From this observational evidence we assume that all Seyfert 1 galaxies have outflows that cover 50% of the solid angle around the central source. Using equation (1) in Arav et al. (2013) we find that the mass flux associated with the UV manifestation of component 1 is $1.0^{+2.0}_{-0.5}$ solar masses per year, and that the kinetic luminosity is $4^{+8}_{-2} \times 10^{41}$ erg s^{-1}. We note that most of the $N_{\rm H}$ in the various outflow components is associated with the higher ionization X-ray phase of the outflow. Therefore, we defer a full discussion of the total mass flux and kinetic luminosity of the outflow to a future paper that will present a combined analysis of the UV and X-ray data sets.

4.4.3 Modeling the temporal behavior of the outflow

The absorption troughs of component 1 change drastically between the five HST high-resolution spectroscopic epochs spanning 16 years (see Figure A.2 and Figure A.3). After finding the location and physical characteristics of component 1 using the 2013 data, the next step is to derive a self-consistent temporal picture for this component. There are two general models that explain trough variability in AGN outflows (e.g., Barlow et al., 1992; Gabel et al., 2003; Capellupo et al., 2012; Arav et al., 2012; Filiz Ak et al., 2013, and references therein). One model attributes the trough variability to changes of the ionizing flux experienced by the outflowing gas. In its simplest form, this model assumes that the total $N_{\rm H}$ along the line of sight does not change as a function of time. A second model invokes material moving across the line of sight, which in general causes changes of $N_{\rm H}$ along the line of sight as a function of time to explain the observed trough changes.

In the case of component 1, we have enough constraints to exclude the model of material moving across our line of sight. The outflow is situated at 3.5 pc from the central source, which combined with the estimated mass of the black hole in NGC 5548 ($4{\times}10^7$ solar masses; Pancoast et al., 2014), yields a Keplerian speed of 1.9×10^7 cm s^{-1} at that distance. As can be seen from Figure A.1, 2/3 of the emission at the wavelength of component 1 arises from the C IV broad emission line (BEL). Therefore, the transverse motion model crucially depends on the ability of gas clouds to cross most of the projected size of the broad line region (BLR) in the time spanning the observations epochs. Reverberation studies (Korista et al., 1995) give the diameter of the C IV BLR as 15 light days or 3.9×10^{16} cm, which for $v_\perp = 1.9 \times 10^7$ cm s^{-1}, yields a crossing time of 2.0×10^9 seconds, i.e., 65 years.

Thus, in the 16 years between our epochs, material that moves at the Keplerian velocity, 3.5 pc away from the NGC 5548 black hole, will cross only about 25% of the projected size of the C IV BLR. Therefore, the much larger change in the residual intensity of the component 1 C IV trough cannot be attributed to new material appearing due to transverse motion at this distance. We note that 25% motion across the projected size of the C IV BLR is a highly conservative limit for two reasons: 1) at certain velocities there are changes of 50% in the residual intensity in the component 1 C IV trough between the 2011 and 2013 epochs; and in the elapsing 2 years, transverse motion will only cover 3% of the projected size of the C IV BLR; 2) material that moves away from the central source under the influence of radial forces should conserve its angular momentum. Therefore, if it moved to distances that are much larger compared with its initial distance, its $v_\perp \ll v_{\rm kep}$ at its current distance. We conclude that even under favorable conditions, the transverse motion model of gas into or out of the line of sight cannot explain the observed behavior of component 1 over the five observed epochs.

Can changes of the ionizing flux experienced by the outflowing gas explain the observed trough changes? We construct such a model under the simplest and restrictive assumption that the $N_{\rm H}$ of component 1 did not change over the 16 years spanning the five high resolution UV spectral epochs. Furthermore, for $\log(n_{\rm e}) = 4.8$ cm^{-3}, the absorber should react

to changes in incident ionizing flux on time-scales of ~ 5 days (see Equation (4.3) here, and discussion in Arav et al., 2012). Therefore, for component 1 we use the restrictive assumption of a simple photoionization equilibrium, determined by the flux level of the specific observation.

In 1998 the AGN was in a high flux level of F=6 (measured at 1350 Å rest-frame and given in units of 10^{-14} ergs s^{-1} cm^{-2} Å^{-1}). At that epoch the absorber only showed a Lyα trough necessitating $\log(U_{\rm H}) \gtrsim 0.1$ (otherwise a N v trough would be detected, see Figure 4.4.3). In 2002 the AGN was in a medium flux level with F=2, at which time the absorber showed C iv and N v troughs in addition to Lyα. In 2004 the AGN was at a historically low flux of F=0.25. In that epoch a Si iii trough appeared in addition to the C iv, N v and Lyα troughs; however, a C ii trough did not appear. The combination of the Si iii and C ii constraints necessitates $-1.3 < \log(U_{\rm H}) < -1.15$ (see Figure 4.4.3). The change in $\log(U_{\rm H})$ required by the photoionization models agrees remarkably well with the change in flux between the 1998 and 2004 epochs as $\log(F_{2004}/F_{1998}) = -1.4$. Thus, a constant $N_{\rm H}$ absorber yields an excellent fit for the absorption features from two epochs with the same spectral energy distribution (high SED in Figure 4.4.3), but with very different $U_{\rm H}$ values. Comparison of several key troughs between the five epochs is shown in Figure A.2 and Figure A.3. The 1350Å flux measurements, plus observation details are given in Table A and the derived column-densities for all the outflow features are given in Table A.

In 2013 the AGN flux was F=3. With this flux level and assuming the same SED, the $U_{\rm H}$ value should have been 50% higher than in 2002, and we would expect to see only C iv, N v and Lyα troughs. Instead we also detect Si iii, C ii, Si ii and Al ii. Therefore, the incident SED for component 1 must have changed, and indeed the 2013 soft X-ray flux is 25 times lower compared to that of the 2002 epoch (see Fig. 1 in Kaastra et al., 2014). This drop is caused by the newly observed obscurer close to the AGN, which does not fully cover the source (Kaastra et al., 2014). We found a good match to the UV absorption and soft X-ray flux with an SED that is similar to that of the high flux one longward of 1 Ryd, but abruptly drops to 6% of that flux between 1 Ryd and 1 keV (see Figure 4.4). This picture is consistent

Figure 4.5: Photoionization phase plot showing the ionization solutions for component 1 for all five epochs. The 2013 epoch solution is identical to the one shown in Figure 4.4.1. For the 1998, 2002, and 2004 epochs we used the high SED (see Figure 4.4) with the same abundances, and their ionization solutions are shown in blue crosses. Dashed lines represent $N_{\rm ion}$ lower-limit that allow the phase-space above the line, while the dotted lines are upper-limits that allow the phase-space below the line (only the most restrictive constraints are shown). $N_{\rm H}$ is fixed for all epochs at the value determined from the 2013 solution. For 1998, 2002 and 2004 the difference in $U_{\rm H}$ values is determined by the ratio of fluxes at 1350Å and the actual value is anchored by the observed $N_{\rm ion}$ constraints. As explained in Section 4.4.3, the $U_{\rm H}$ position of the 2011 epoch is less tightly constrained. The solution for each epoch satisfies all the $N_{\rm ion}$ constraints for that epoch.

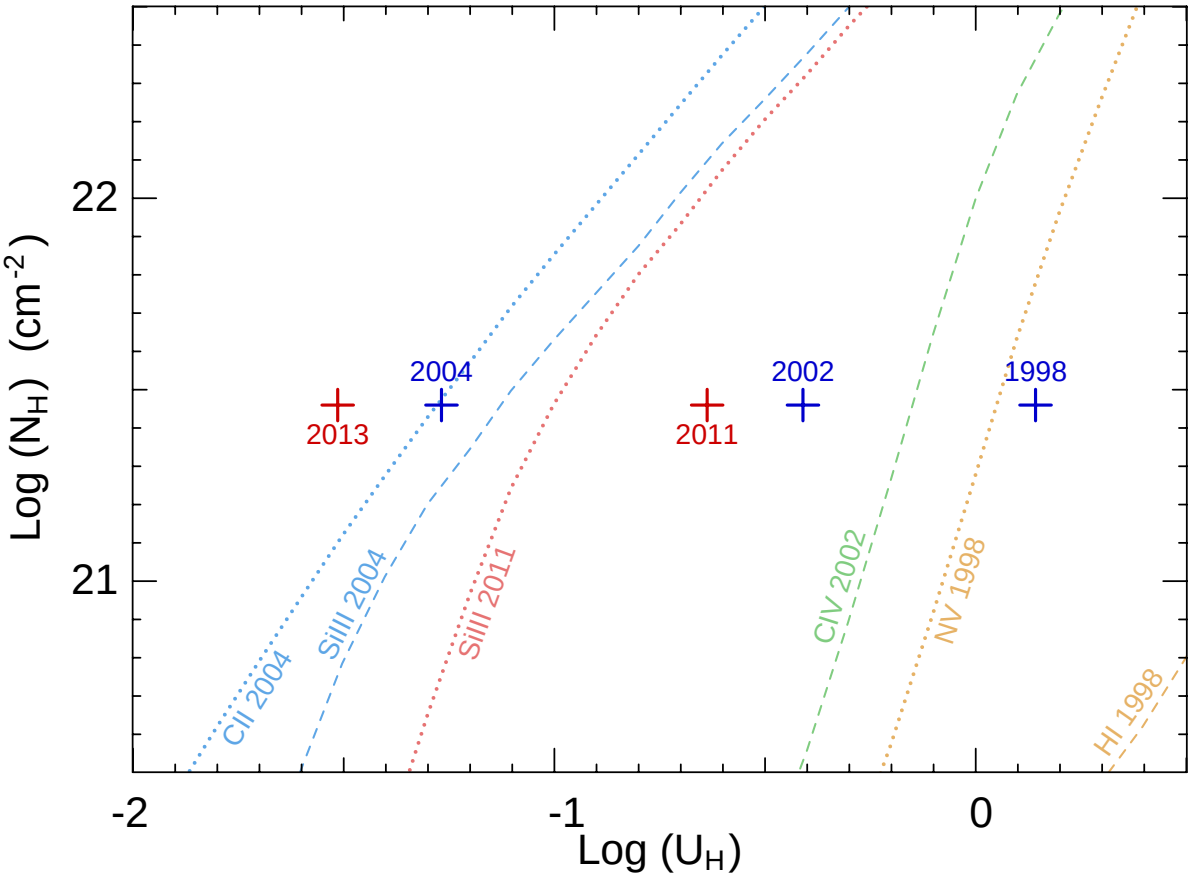

with the transmitted flux resulting from the low-ionization, partial covering model of the obscurer derived in Kaastra et al. (2014). To complete the UV picture for component 1, in 2011 NGC 5548 showed F=6, equal to that of the 1998 epoch. However, C IV and N V are clearly seen in the 2011 epoch but not any of the other ionic species seen in 2013. To explain this situation we assume that the obscurer was present at the 2011 epoch, but it only blocked somewhere between 50–90% of the emitted ionizing radiation between 1 Ryd and 1 keV. The possible presence of a weaker X-ray obscurer is also suggested by broad absorption on the blue wing of the C IV emission line in 2011 that is weaker than that seen in 2013.

To summarize, a simple model based on a fixed total column-density absorber, reacting to changes in ionizing illumination, matches the very different phenomenology seen in all high-resolution UV spectra of component 1 spanning 16 years. Figure 4.6 gives a schematic illustration of the temporal model.

4.5 Components 2-6

We can derive distances (or limits of) for the other five outflow components and some constraints on the $N_{\rm H}$ and $U_{\rm H}$ of components 3 and 5. Figure 4.6 gives the velocities and distances of all six components, as well as a schematic illustration for their temporal behavior.

4.5.1 Constraining the distances

Components 2-6 do not show absorption from excited levels (except for component 3, whose C II/C II* troughs only yield a lower limit for $n_{\rm e}$). However, components 3 and 5 show clear variations in their Si III and Si IV troughs between our 2013/6/22 and 2013/8/1 observations, but not between the 2013/7/24 and 2013/8/1 ones, when we do see changes in component 1. Using the formalism given in Section 4 of Arav et al. (2012), we can deduce the $n_{\rm e}$ of these components from the observed time lags. Suppose an absorber in photoionization

equilibrium experiences a sudden change in the incident ionizing flux such that $I_i(t > 0) = (1 + f)I_i(t = 0)$, where $-1 \leq f \leq \infty$. Then the timescale for change in the ionic fraction is given by:

$$t^* = \left[-f\alpha_i n_e \left(\frac{n_{i+1}}{n_i} - \frac{\alpha_{i-1}}{\alpha_i} \right) \right]^{-1}, \tag{4.3}$$

where α_i is the recombination rate of ion i and n_i is the fraction of a given element in ionization stage i. From the 40 days that separate epochs showing trough changes and the 7 days separating epochs with no change, we can deduce $3.5 < \log(n_{\rm e}) < 4.5$ cm^{-3} for both components, otherwise their troughs would not react to changes in incident ionizing flux in the observed way, despite the large changes in incident ionizing flux over that period. Assuming a similar $U_{\rm H}$ to that of component 1 (see discussion below), this $n_{\rm e}$ range yields distances of $5 < R < 15$ pc. Similarly, component 6 shows C IV and N V troughs in 2011 but not in 2002. This nine years timescale yields $R < 100$ pc. Component 2 and component 4 do not show changes in the UV absorption between any of the epochs. Therefore, we can derive a lower limit for their distance of $R > 130$ pc.

4.5.2 Constraining $N_{\rm H}$ and $U_{\rm H}$:

It is not feasible to put physically interesting constraints on components 2, 4 and 6. First, they only show troughs from C IV, N V, and Lyα, which (based on our analysis of component 1) are probably highly saturated. Second, the ionization time-scales of components 2 and 4 are larger than 16 years. Therefore, even if a $U_{\rm H}$ can be deduced from the measurements, it will only be a representative average value for a period of time larger than 16 years.

Figure 4.6 shows the $N_{\rm H}$–$U_{\rm H}$ phase plot for component 3 based on the $N_{\rm ion}$ reported in Table A (the Lyα and C IV $N_{\rm ion}$ lower limits are trivially satisfied by the lower limit shown for the N V $N_{\rm ion}$). The phase plot constraints given by the $N_{\rm ion}$ measurements are mostly parallel to each other. Therefore, the $N_{\rm H}$–$U_{\rm H}$ constraints are rather loose, allowing a narrow strip from $\log(N_{\rm H}) = 19.6$ cm^{-2} and $\log(U_{\rm H}) = -2$, to $\log(N_{\rm H}) = 21.5$ cm^{-2} and $\log(U_{\rm H}) = -1.1$. If we take the most probable value of $\log(U_{\rm H}) = -1.3$, the distance estimate for component 3 will

drop by 30% compared with the estimate of $5 < R < 15$ pc, which used the $\log(U_{\rm H}) = -1.5$ of component 1. For component 5, the situation is rather similar, as the detected Si III and Si IV allow a narrow strip from $\log(N_{\rm H}) = 19.2$ cm^{-2} and $\log(U_{\rm H}) = -1.8$, to $\log(N_{\rm H}) = 20.7$ cm^{-2} and $\log(U_{\rm H}) = -1.2$, while the lowest χ^2 is achieved at $\log(N_{\rm H}) = 20.7$ cm^{-2} and $\log(U_{\rm H}) = -1.3$.

4.6 Comparison with the warm absorber analysis

Here we compare the physical characteristics inferred from the outflows' UV diagnostics to the properties of the X-ray manifestation of the outflow known as the warm absorber (WA). Since the soft X-ray flux in our 2013 data is very low due to the appearance of the obscurer, we cannot characterize the WA that is connected with the six UV outflow components at that epoch. Our main inferences about the WA are from the 2002 epoch when we obtained simultaneous X-ray and UV spectra of the outflow (when no obscurer was present) that gave a much higher soft X-ray flux (compared with the 2013 observations) and allowed a detail modeling of the WA in that epoch (Steenbrugge et al., 2005; Kaastra et al., 2014). Due to the inherent complications of comparing analyses on different spectral regions (X-ray and UV) separated by 11 years (2002 and 2013), of a clearly time-dependent phenomenon, we defer a full comparison to a later paper (Ebrero et al 2015). Here we outline some of the main points in such a comparison, based on the analysis presented here and the published analysis of the WA (Steenbrugge et al., 2005; Kaastra et al., 2014) and discuss some of the similarities and challenges of such a combined analysis.

4.6.1 Kinematic similarity

There is kinematic correspondence between the UV absorption troughs in components 1–5 and the six ionization components (A–F) of the X-ray WA (Kaastra et al., 2014, see Table 4.6.1 here). X-ray components F and C span the width of UV component 1. X-ray

Figure 4.6: An illustration of the physical, spatial and temporal conditions of the outflows seen in NGC 5548. Along the time axis we show the behavior of the emission source at the five UV epochs and give its UV flux values (measured at 1350 Å rest-frame and given in units of 10^{-14} ergs s^{-1} cm^{-2} $Å^{-1}$). The obscurer is situated at roughly 0.01 pc from the emission source and is only seen in 2011 and 2013 (it is much stronger in 2013). Outflow component 1 shows the most dramatic changes in its absorption troughs. Different observed ionic species are represented as colored zones within the absorbers. The trough changes are fully explained by our physical model shown in Figure 4.4.3. Using component 1 C III* troughs, which are only seen in the 2013 epoch, we determine its number density (see Figure 4.4.2) to be $\log(n_e) = 4.8 \pm 0.1$ cm^{-3}, and therefore its distance, R=3.5 pc. The distances for the other components are discussed in Section 4.5. Dimmer clouds represent epochs where components 2-6 did not show new absorption species compared with the 2002 epoch.

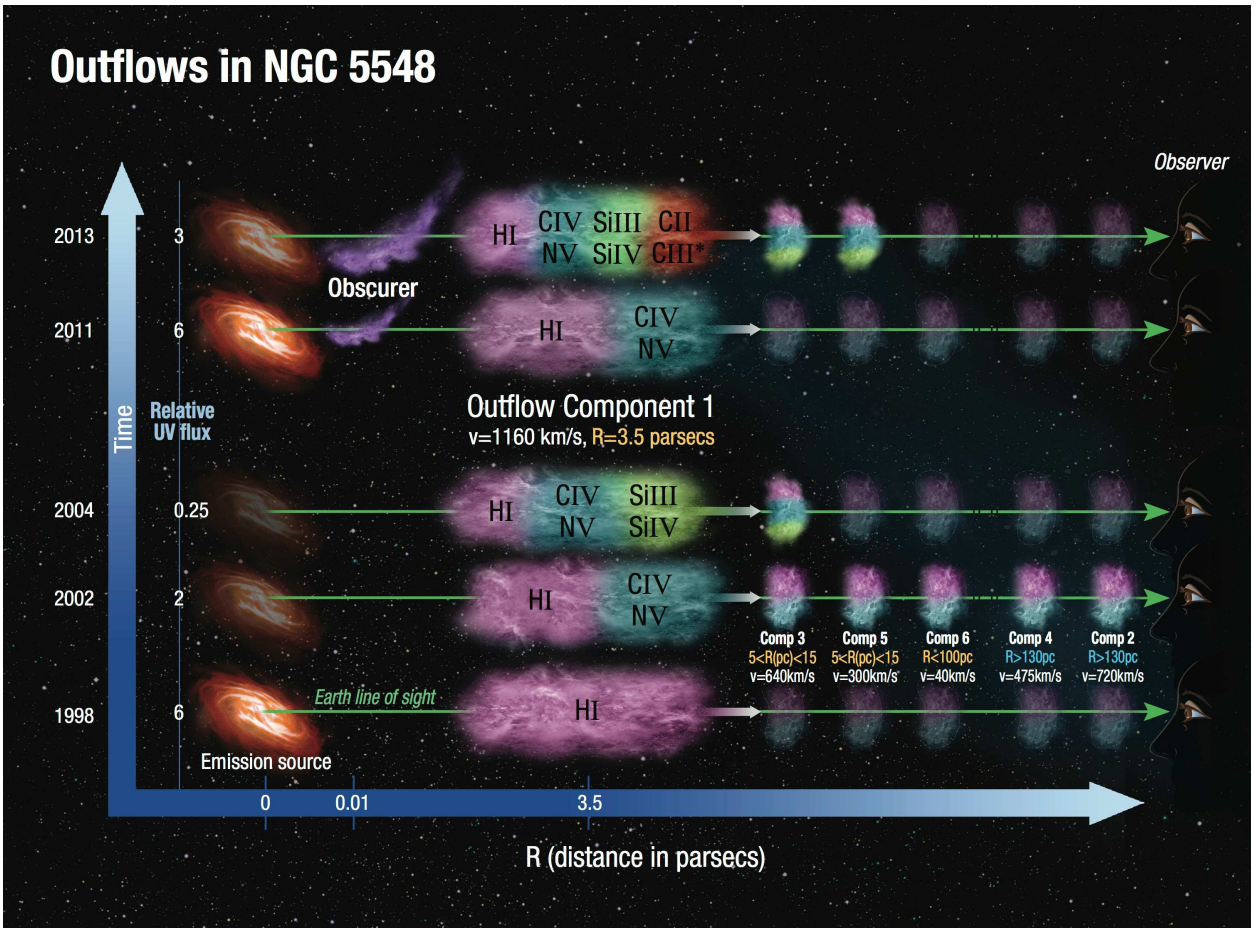

Figure 4.7: A photoionization phase plot showing the ionization solution for component 3 epoch 2013. As for component 1, we use the obscured SED and assumed proto-solar metalicity (Lodders, Palme & Gail, 2009). Solid lines and associated colored bands represent the locus of ($U_{\rm H}$, $N_{\rm H}$) models, which predict the measured $N_{\rm ion}$, and their 1σ uncertainties, while the dashed line is the lower limit on the N V column-density that permits the phase-space above it. The blue cross is the best χ^2 solution and is surrounded by a 1σ χ^2 blue contour.

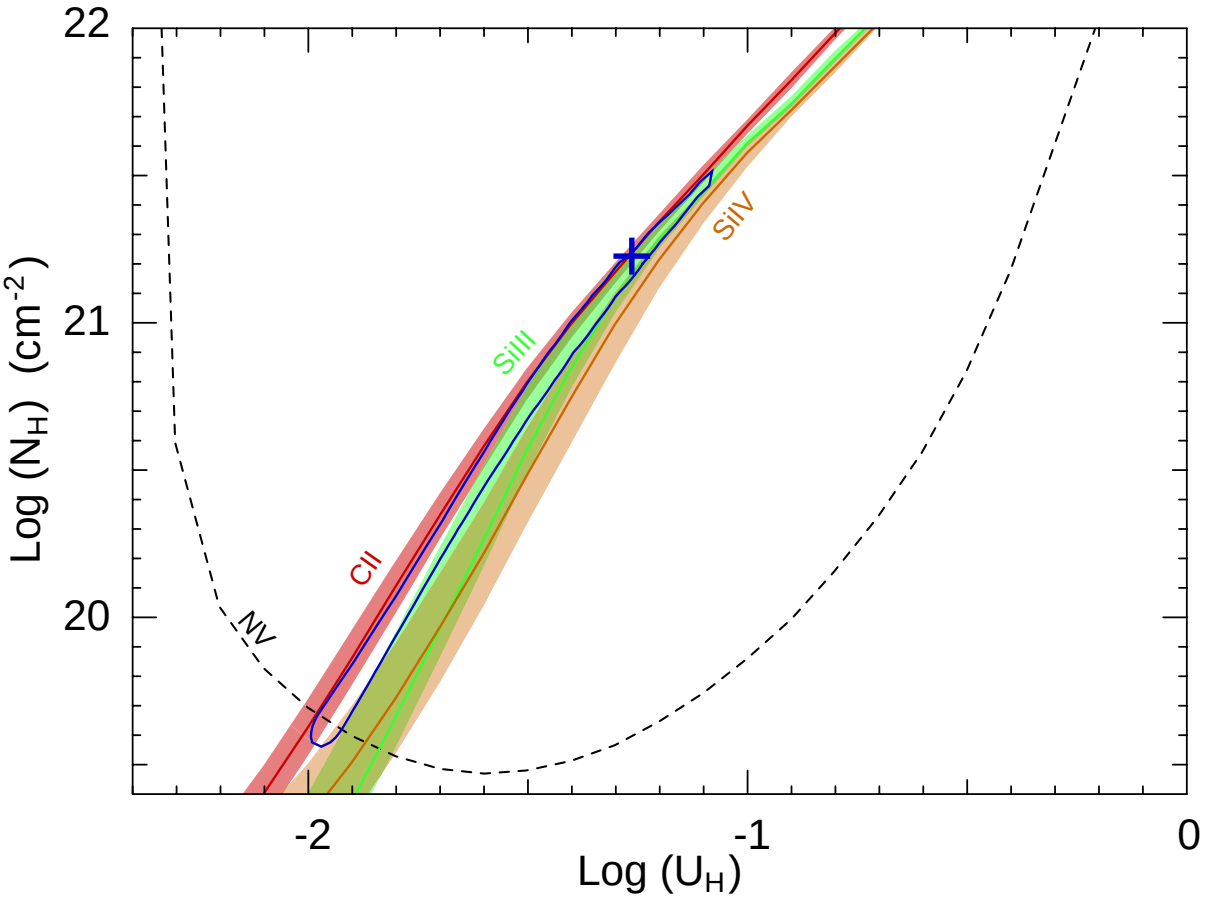

component E matches UV component 2. The lowest ionization X-ray components, A and B comprise the full width of the blended UV troughs of components 3 and 4. Finally, X-ray component D kinematically matches UV component 5. However, as we show in point 2 below, this kinematic matching is physically problematic as the ionization parameters of WA components C, D, E and F are too high to produce observed troughs from C IV and N V that are observed in all the UV components.

Table 4.1: Comparison between the UV and WA components

Component	Velocity[a] (km s^{-1})	$\log(N_H)$ (cm^{-2})	$\log(U_H)$ (2002)
UV 1[b]	-1160	$21.5^{+0.4}_{-0.2}$	$-0.4^{+0.4}_{-0.2}$
UV 2	-720	—	—
UV 3	-640	$19.6 - 21.5$	$(-0.9) - 0.0$
UV 4	-475	—	—
UV 5	-300	$19.2 - 20.7$	$(-0.7) - (-0.1)$
UV 6	-40	—	—
WA A[c]	-588 ± 34	20.30 ± 0.12	-0.82 ± 0.08
WA B	-547 ± 31	20.85 ± 0.06	-0.09 ± 0.05
WA C	-1148 ± 20	21.18 ± 0.08	0.55 ± 0.03
WA D	-255 ± 25	21.03 ± 0.07	0.76 ± 0.03
WA E	-792 ± 25	21.45 ± 0.12	1.34 ± 0.08
WA F	-1221 ± 25	21.76 ± 0.13	1.53 ± 0.05

[a]velocity centroid of the component
[b]UV components 1-6 are arranged by decreasing absolute velocity.
[c]Parameters for Warm Absorber components A-F are from Table S2 of Kaastra et al. (2014). They are arranged by increasing ionization parameter.

4.6.2 Comparing similar ionization phases

We note that the X-ray analysis of the WA in the Chandra 2002 observations uses a different ionization parameter (ξ) than the U_H we use here; where $\xi \equiv L/(n_H r^2)$ (erg cm s^{-1}) with n_H being the hydrogen number density, L the ionizing luminosity between 13.6 eV and 13.6 keV and r the distance from the central source. For the high SED, $log(U_H) = \log(\xi) + 1.6$.

In Table 4.6.1, we give the $log(U_{\rm H})$ for the WA components. From the WA analysis and Figure 4.4.3 here, we deduce that 90% of the WA material (components C, D , E and F in Table S2 of Kaastra et al., 2014) is in a too high ionization stage to produce measurable lines from the UV observed ions (e.g., C IV, N V). Only component A and B of the WA are at low enough ionization states to give rise to the UV observed material. The issue of pressure equilibrium between the different ionization phases is beyond the scope of this paper, and will be discussed in a forthcoming paper.

4.6.3 Assuming constant $N_{\rm H}$ for the UV components and components A and B of the WA.

Our temporal model for component 1 has a constant $N_{\rm H}$ value in all the observed epochs, including 2002. The model also predicts the $U_{\rm H}$ of the 2002 epoch (see Figure 4.4.3). We can therefore compare the predictions of this model to the results of the reanalysis of the 2002 WA (Kaastra et al., 2014), provided that the $N_{\rm H}$ for components A and B of the WA also did not change over the 11 years between the epochs. We note that since UV component 1 is the closest to the central source, the assumption of constant $N_{\rm H}$ for the other UV components, over this 11 years time period, is reasonable (see discussion in Section 4.4.3). Therefore, we use the same ionization assumptions for UV components 3 and 5 as for component 1. That is, their $N_{\rm H}$ is fixed to the 2013 value and their $\log(U_{\rm H})_{2002} = \log(U_{\rm H})_{2013} + 1.1$, which are the values we list in Table 4.6.1. We do not have empirical constraints on the distances of WA components A-F from the central source.

4.6.4 Comparing UV components 1 and 3 to components A and B of the WA.

Using proto-Solar abundances (Lodders, Palme & Gail, 2009), our 2002 model prediction for UV component 1 has $\log(N_{\rm H}) = 21.5^{+0.4}_{-0.2}$ cm^{-2}, and an ionization parameter of $\log(U_{\rm H}) =$

$-0.4^{+0.4}_{-0.2}$ (see Section 4.4.1 and Figure 4.4.3). This model gives a good match for the UV data of that epoch (2002) and its $\log(U_{\rm H})$ is in between those of WA components A [$\log(U_{\rm H}) = -0.8$] and B [$\log(U_{\rm H}) = -0.1$]. However, there are two inconsistencies between the models. First, components A and B have a total $\log(N_{\rm H}) = 20.95\pm0.1$ cm^{-2} or about 2σ disagreement with that of UV component 1. This discrepancy is mainly due to the limit on the O VII $N_{\rm ion}$ that arises from the bound-free edge of this ion in the X-ray data. In the WA model, about 95% of the O VII $N_{\rm ion}$ arises from components A and B. Second, the reported velocity centroids for WA components A and B (-588 ± 34 km s^{-1} and -547 ± 31 km s^{-1}, respectively) are in disagreement with the velocity centroids of UV component 1 (-1160 km s^{-1}) and its 300 km s^{-1} width.

UV component 3 has a velocity centroid at –640 km s^{-1} and a width of $\sim$200 km s^{-1}, and therefore is a better velocity match with WA components A and B. The large uncertainties in the inferred $N_{\rm H}$ and $U_{\rm H}$ for UV component 3 (see Figure 4.4.3 and Table 4.6.1), make these values consistent with the $N_{\rm H}$ and $U_{\rm H}$ deduced for WA components A and B. However, the uncertainties also allow UV component 3 to have a negligible $N_{\rm H}$ compared to WA components A and B.

We note that with the current analyses, the better the agreement between UV component 3 and WA components A and B, the worse is the disagreement between UV component 1 and WA components A and B. This is because UV component 1 already predicts higher values of $N_{\rm H}$ and O VII $N_{\rm ion}$ than are measured in WA components A and B, and the kinematics of the deduced O VII $N_{\rm ion}$ disagree considerably. In points 5 and 6 below we identify two possible ways to alleviate and even eliminate these apparent discrepancies.

4.6.5 Existence of considerable O VII $N_{\rm ion}$ at the velocity of UV component 1

The 2002 X-ray spectra presented by Steenbrugge et al. (2005) consist of two different data sets that were acquired in the same week: 170 ks observations taken with the High Energy Transmission Grating Spectrometer (HETGS) and 340 ks observations with the Low Energy Transmission Grating Spectrometer (LETGS). Figure 2 in Steenbrugge et al. (2005) shows some of the low ionization WA troughs in velocity presentation, where the dotted lines show the position of the UV components (with somewhat different velocity values than we use here due to the use of a slightly different systemic redshift for the object). The LETGS data of the O VII and O V troughs are consistent with one main kinematic component matching the velocity of UV component 3. However, the more noisy but higher resolution HETGS data for the same transitions, show two subtroughs: one corresponding to UV component 1 and one to UV component 3. Therefore, it is possible that much of the O VII $N_{\rm ion}$ is associated with UV component 1.

4.6.6 Abundances considerations

As mentioned in Section 4.4, for the UV analysis, we use pure proto-Solar abundances (Lodders, Palme & Gail, 2009), which well-match the measured $N_{\rm ion}$ from the UV data. But these models produce considerably more O VII $N_{\rm ion}$ in the 2002 epoch, than the measured O VII $N_{\rm ion}$ in the warm absorber data. However, the $N_{\rm H}$ (and therefore also the O VII $N_{\rm ion}$) of UV component 1 is critically dependent on the assumed phosphorus abundance. Ionization models with all elements having proto-Solar abundances except phosphorus, for which we assume twice proto-Solar abundance, preserve the fit to the UV data (at 1/3 the $N_{\rm H}$ value) and at the same time match the O VII $N_{\rm ion}$ measured in the X-ray warm absorber at the 2002 epoch. Larger over-abundances of phosphorus further reduce the $N_{\rm H}$ value and therefore the predicted O VII $N_{\rm ion}$ for the 2002 epoch.

But are such assumed abundances physically reasonable? AGN outflows are known to have abundances higher by factors of two (Arav et al., 2007) and even ten (Gabel, Arav & Kim, 2006) compared with the proto-Solar values. In particular, phosphorus abundance in AGN outflows, relative to other metals, can be a factor of several higher than in proto-Solar abundances (see Section 4.1 in Arav et al., 2001b). Furthermore, the theoretical expectations for the value of chemical abundances in an AGN environment as a function of metalicity are highly varied. The leading models can differ about relative abundances values by factors of three or more (e.g., comparing the values of Hamann & Ferland, 1993; Ballero et al., 2008).

We conclude that if roughly half of the observed O VII $N_{\rm ion}$ is associated with UV component 1 (as discussed in point 5), and if the relative abundance of phosphorus to oxygen is twice solar or larger, than the $N_{\rm H}$, $U_{\rm H}$ and velocity distribution of the WA and UV outflowing gas can be consistent.

4.7 Discussion

4.7.1 Comparison with Crenshaw et al. (2009)

Here we compare our results with previous work by Crenshaw et al. (2009, hereafter C09) on the "enduring" outflow in NGC 5548. For the first time a simple model of a constant $N_{\rm H}$ absorber yields a physical picture that is consistent with the substantial trough variations seen in all epochs of high-resolution UV spectral observations. The trough changes are explained solely by the observed differences in the incident ionizing flux. In addition, we determine robust distances for (or limits on) all six kinematic components.

Our results differ considerably from those previously found for this outflow in C09. The HST epochs of 1998, 2002 and 2004 were analyzed by C09. In Table 4.7.1 we show for component 1 the deduced $\log(N_{\rm H})$ and $\log(U_{\rm H})$ values for these 3 epochs, for both C09 (see their Table 6) and this work (see Figure 4.4.3 here). It is clear that we derive very different parameters

Table 4.2: Comparing the photoionization solutions for component 1

	$\log(N_{\rm H})$		$\log(U_{\rm H})$	
Epoch	This Work	C09	This Work	C09
1998	21.50	19.23	0.14	-0.50
2002	21.50	19.55	-0.41	-0.74
2004	21.50	20.35	-1.27	-0.55

than those of C09.

The main reason for these differences is the reliability of the measured ionic column censities (N_{ion}), which are used as input in photoionization models. Both works use Cloudy, assume the same abundances and use a similar SED. C09 base their photoionization solution on the $N_{\rm ion}$ of C IV and N V (see C09 Table 5). We obtain similar C IV and N V $N_{\rm ion}$ values in these epochs (see Table A here), but we only use them as lower limits. The new diagnostic troughs seen during the 2013 campaign (especially P V) demonstrate this crucial point. The existence of similar depth C IV and P V troughs in component 1 is evidence that the actual C IV $N_{\rm ion}$ is at least a factor of 100 larger than the lower limit (see discussion in Borguet et al., 2012a). A similar situation occurs for N V. This assertion is confirmed quantitatively by our full photoionization models. With such large saturation factors, photoionization solutions for this outflow based on the trough-derived C IV and N V $N_{\rm ion}$ are unreliable.

Examining the results for the 2004 epoch demonstrates these issues. Using the C IV and N V $N_{\rm ion}$ values of C09 for component 1, we can reproduce their $\log(U_{\rm H})$ and $\log(N_{\rm H})$ parameters. However, the 2004 HST spectrum shows clear Si III troughs in components 1 and 3 (see Figure A.3 here) that are unaccounted for in C09. The C09 solution shown in Table 4.7.1 is incompatible with the Si III $N_{\rm ion}$ measurement, even if that trough is unsaturated. To reproduce the Si III measurement using the C09 $\log(N_{\rm H}) = 20.35$ cm^{-2}, $\log(U_{\rm H})$ need to be -1.7 ± 0.1 instead of the C09 value of $\log(U_{\rm H}) = -0.55$. However, at $\log(N_{\rm H}) = 20.35$ cm^{-2} and $\log(U_{\rm H}) = -1.7$, Cloudy yields a C IV $N_{\rm ion}$ that is 100 times larger than the value C09 deduce from the observations (see their Table 5).

In conclusion, our improved physical modeling is due to powerful diagnostics that were

revealed during the 2013 campaign, establishing that many of the observed troughs are highly saturated; and also because C09 did not account for the Si III troughs associated with components 1 and 3 in the 2004 data.

4.7.2 Implications for BALQSO variability studies

Our multiwavelength campaign has significant consequences for studies of absorption trough variability in quasar outflows, and in particular for the intensive studies of trough variability in broad absorption line (BAL) quasars (e.g., Barlow et al., 1992; Capellupo et al., 2012; Filiz Ak et al., 2013, and references therein). AGN outflow absorption systems with different velocity width, and different AGN luminosities, share similar physical characteristics (e.g., ionization states, trough variability time scales, trough variability pattern, solar or larger metallicity, non-black saturation in the troughs). Therefore, we can make a comparison between the mechanisms in the narrow outflow of NGC 5548 to that of BALs in QSOs.

As discussed in Section 4.4.3, the two main proposed mechanisms for trough variability are (1) reaction to changes in ionizing flux of a constant absorber (which is the model we successfully use to explain the NGC 5548 outflow trough changes); and (2) absorber motion across the line of sight (e.g., Gabel et al., 2003), which as we demonstrated, cannot explain the variability of the enduring, narrow-trough outflow in NGC 5548 (see Section 4.4.3).

In some BALQSO cases the rest-frame UV flux around 1350Å does not change appreciably between the studied epochs while significant trough variability is observed. This behavior is taken as an argument against mechanism (1) (e.g., Barlow et al., 1992; Filiz Ak et al., 2013) as the ionizing flux (below 912Å) is assumed to correlate with the longer wavelength UV flux. However, our simultaneous UV/X-ray observations show a clear case where the ionizing photon flux drops by a factor of 25 between the 2002 and 2013 epochs, while the 1350Å UV flux actually increases by 50%.

Mechanism (1) is a simpler explanation for cases where velocity-separated outflow troughs

change in the same way between different epochs (i.e., when all troughs become either shallower or deeper; Capellupo et al., 2012; Filiz Ak et al., 2013). As we demonstrated, the objection to this model based on the assumed correlation between the rest-frame UV flux around 1350Å and the ionizing flux might not be valid. Therefore, due to its simplicity, mechanism (1) is a strong contender for interpreting trough variability data of quasar outflows.

We note that the above discussion does not exclude the possibility of trough variability due to absorber motion across the line of sight, in some cases. Indeed it is possible that this mechanism explains the variability in the newly discovered broad UV absorption in NGC 5548, as argued in Kaastra et al. (2014).

The data set of NGC 5548 (spanning five high-resolution spectroscopic epochs between 1998 and 2013) gives high S/N spectra of UV absorption troughs that arise from many different ions, and simultaneously yields the crucial soft X-ray flux that is responsible for the ionization of the outflow. Such data can constrain trough variability models far better than the standard variability data sets where one or two rest-frame UV BAL are observed at two (and less frequently in more) epochs (e.g., Capellupo et al., 2012; Filiz Ak et al., 2013).

4.7.3 Implications for the X-ray obscurer

Our results about the "enduring" outflow have implications for the X-ray obscurer and the broad UV absorption discovered by Kaastra et al. (2014). The derived transmission for the X-ray obscurer is consistent with the SED required for the 2013 spectrum, thus showing that the obscurer is closer to the super massive black holes than 3.5 pc, and that its shadow influences the conditions in the more distant narrow UV absorbers.

4.8 Summary

In 2013 we executed the most comprehensive multiwavelength spectroscopic campaign on any AGN to date, directed at NGC 5548. This paper presents the analysis' results from our HST/COS data of the enduring UV outflow, which is detected in six distinct kinematic components. Our campaign revealed an unusually strong X-ray obscuration. The resulting dramatic decrease in incident ionizing flux on the outflow allowed us to construct a comprehensive physical, spatial and temporal picture for the well-studied AGN wind in this object. Our main findings are listed below (see Figure 4.6 for a graphic illustration of our results).

1. Our best constraints are obtained for component 1 (the highest velocity component). It is situated at $R = 3.5^{+1.0}_{-1.2}$ pc from the central source, has a total hydrogen column-density of $\log(N_{\rm H}) = 21.5^{+0.4}_{-0.2}$ cm^{-2}, an ionization parameter of $\log(U_{\rm H}) = -1.5^{+0.4}_{-0.2}$, and an electron number density of $\log(n_{\rm e}) = 4.8 \pm 0.1$ cm^{-3}. This component probably carries the largest $N_{\rm H}$ associated with the UV outflow. See Section 4.4.1 and Section 4.4.2.

2. For component 1 a simple model based on a fixed total column-density absorber, reacting to changes in ionizing illumination, matches the very different ionization states seen at five spectroscopic epochs spanning 16 years. See Section 4.4.3.

3. The distance and number density of component 1 are similar to those of the narrow-emitting-line-region in this object (Peterson et al., 2013). See Section 4.4.2.

4. The wealth of observational constraints makes our changes-of-ionization model a leading contender for interpreting trough variability data of quasar outflows, in particular broad absorption line (BAL) variability. See Section 4.7.2.

5. Components 3 and 5 are situated between 5-15 pc from the central source, component 6 is closer than 100 pc and components 2 and 4 are further out than 130 pc. See Section 4.5.

A detailed comparison of the physical characteristics inferred from the outflows' UV diagnostics with those of the X-ray Warm Absorber is deferred to a future paper. Here we outline some of the main points in such a comparison, and discuss some of the similarities and challenges of such a combined analysis. See Section 4.6.

Acknowledgement

Figure 4.6 was created by Ann Feild from STScI.

Chapter 5

Conclusions

This thesis presented detailed analyses on three different quasar outflows. It can be concluded from these analyses that

1. The use of collisional excitation simulations to model excited-state absorption lines from multiple ions can yield a self-consistent measurement of electron number density (Chapter 2). Utilizing such excited-state diagnostics is a powerful technique for determining physical properties of quasar outflows.

2. Quasar outflows can be observed much farther away from the central source than their presumed formation region (Chapter 2 and Chapter 3). Either outflows are stable over the timescales needed to travel from their origin to the observed location, or the mechanism by which outflows are formed needs to be re-examined.

3. A sample of currently-studied quasar outflows contain enough energy to theoretically produce AGN feedback effects (Chapter 3). A larger sample of quasar outflows should be pursued to determine a reasonable average outflow energy that can be generalized to all AGN.

4. Variability of absorption troughs can be interpreted using a simple change-in-ionization model (Chapter 4). This model provides a plausible alternative to the transverse-motion-across-the-line-of-sight model commonly used to explain trough variability.

5. Obscuration of the emission source can decrease the ionizing flux incident on the outflow and cause drastic changes in the ionization state of the outflowing gas (Chapter 4). Concurrent, multiwavelength observations should be pursued when studying trough variability since the emission source can vary in different energy ranges.

Bibliography

Aoki K., Oyabu S., Dunn J. P., Arav N., Edmonds D., Korista K. T., Matsuhara H., Toba Y., 2011, PASJ, 63, 457

Arav N., 1997, in Astronomical Society of the Pacific Conference Series, Vol. 128, Mass Ejection from Active Galactic Nuclei, Arav N., Shlosman I., Weymann R. J., eds., p. 208

Arav N., Becker R. H., Laurent-Muehleisen S. A., Gregg M. D., White R. L., Brotherton M. S., de Kool M., 1999a, ApJ, 524, 566

Arav N., Borguet B., Chamberlain C., Edmonds D., Danforth C., 2013, MNRAS, 436, 3286

Arav N., Brotherton M. S., Becker R. H., Gregg M. D., White R. L., Price T., Hack W., 2001a, ApJ, 546, 140

Arav N. et al., 2015, A&A, 577, A37

Arav N. et al., 2001b, ApJ, 561, 118

Arav N. et al., 2012, A&A, 544, A33

Arav N. et al., 2007, ApJ, 658, 829

Arav N., Kaastra J., Kriss G. A., Korista K. T., Gabel J., Proga D., 2005, ApJ, 620, 665

Arav N., Kaastra J., Steenbrugge K., Brinkman B., Edelson R., Korista K. T., de Kool M., 2003, ApJ, 590, 174

Arav N., Korista K. T., de Kool M., 2002, ApJ, 566, 699

Arav N., Korista K. T., de Kool M., Junkkarinen V. T., Begelman M. C., 1999b, ApJ, 516, 27

Arav N., Moe M., Costantini E., Korista K. T., Benn C., Ellison S., 2008, ApJ, 681, 954

Ballero S. K., Matteucci F., Ciotti L., Calura F., Padovani P., 2008, A&A, 478, 335

Ballester P., Bramich D., Forchi V., Freudling W., Garcia-Dabó C. E., klein Gebbinck M., Modigliani A., Romaniello M., 2011, in Astronomical Society of the Pacific Conference Series, Vol. 442, Astronomical Data Analysis Software and Systems XX, I. N. Evans, A. Accomazzi, D. J. Mink, & A. H. Rots, ed., p. 261

Barlow T. A., Hamann F., Sargent W. L. W., 1997, in Astronomical Society of the Pacific Conference Series, Vol. 128, Mass Ejection from Active Galactic Nuclei, N. Arav, I. Shlosman, & R. J. Weymann, ed., pp. 13–+

Barlow T. A., Junkkarinen V. T., Burbidge E. M., Weymann R. J., Morris S. L., Korista K. T., 1992, ApJ, 397, 81

Bautista M. A., Dunn J. P., Arav N., Korista K. T., Moe M., Benn C., 2010, ApJ, 713, 25

Borguet B. C. J., Arav N., Edmonds D., Chamberlain C., Benn C., 2013, ApJ, 762, 49

Borguet B. C. J., Edmonds D., Arav N., Benn C., Chamberlain C., 2012a, ApJ, 758, 69

Borguet B. C. J., Edmonds D., Arav N., Dunn J., Kriss G. A., 2012b, ApJ, 751, 107

Capellupo D. M., Hamann F., Shields J. C., Rodríguez Hidalgo P., Barlow T. A., 2012, MNRAS, 422, 3249

Cardelli J. A., Clayton G. C., Mathis J. S., 1989, ApJ, 345, 245

Cattaneo A. et al., 2009, Nature, 460, 213

Chamberlain C., Arav N., 2015, MNRAS, 454, 675

Chamberlain C., Arav N., Benn C., 2015, MNRAS, 450, 1085

Choi E., Naab T., Ostriker J. P., Johansson P. H., Moster B. P., 2014, MNRAS, 442, 440

Churchill C. W., Mellon R. R., Charlton J. C., Jannuzi B. T., Kirhakos S., Steidel C. C., Schneider D. P., 1999, ApJ, 519, L43

Ciotti L., Ostriker J. P., Proga D., 2009, ApJ, 699, 89

Ciotti L., Ostriker J. P., Proga D., 2010, ApJ, 717, 708

Costantini E. et al., 2007, A&A, 461, 121

Crenshaw D. M., Kraemer S. B., Boggess A., Maran S. P., Mushotzky R. F., Wu C., 1999, ApJ, 516, 750

Crenshaw D. M. et al., 2003, ApJ, 594, 116

Crenshaw D. M., Kraemer S. B., Schmitt H. R., Kaastra J. S., Arav N., Gabel J. R., Korista K. T., 2009, ApJ, 698, 281

Dai X., Shankar F., Sivakoff G. R., 2008, ApJ, 672, 108

Dai X., Shankar F., Sivakoff G. R., 2012, ApJ, 757, 180

de Kool M., Arav N., Becker R. H., Gregg M. D., White R. L., Laurent-Muehleisen S. A., Price T., Korista K. T., 2001, ApJ, 548, 609

de Kool M., Becker R. H., Arav N., Gregg M. D., White R. L., 2002a, ApJ, 570, 514

de Kool M., Becker R. H., Gregg M. D., White R. L., Arav N., 2002b, ApJ, 567, 58

de Kool M., Korista K. T., Arav N., 2002, ApJ, 580, 54

de Vaucouleurs G., de Vaucouleurs A., Corwin, Jr. H. G., Buta R. J., Paturel G., Fouqué P., 1991, Third Reference Catalogue of Bright Galaxies. Volume I: Explanations and references. Volume II: Data for galaxies between 0^h and 12^h. Volume III: Data for galaxies between 12^h and 24^h.

Dere K. P., Landi E., Mason H. E., Monsignori Fossi B. C., Young P. R., 1997, A&AS, 125, 149

Di Matteo T., Springel V., Hernquist L., 2005, Nature, 433, 604

Dunn J. P., Arav N., Aoki K., Wilkins A., Laughlin C., Edmonds D., Bautista M., 2012, ApJ, 750, 143

Dunn J. P. et al., 2010, ApJ, 709, 611

Edmonds D. et al., 2011, ApJ, 739, 7

Elvis M., 2006, Mem. Soc. Astron. Italiana, 77, 573

Faucher-Giguère C.-A., Quataert E., 2012, MNRAS, 425, 605

Faucher-Giguère C.-A., Quataert E., Murray N., 2012, MNRAS, 420, 1347

Ferland G. J. et al., 2013, Rev. Mexic. de Astron. y Astrof., 49, 137

Filiz Ak N. et al., 2013, ApJ, 777, 168

Gabel J. R. et al., 2005a, ApJ, 623, 85

Gabel J. R., Arav N., Kim T., 2006, ApJ, 646, 742

Gabel J. R. et al., 2003, ApJ, 583, 178

Gabel J. R. et al., 2005b, ApJ, 631, 741

Ganguly R., Brotherton M. S., 2008, ApJ, 672, 102

Ganguly R., Eracleous M., Charlton J. C., Churchill C. W., 1999, AJ, 117, 2594

Germain J., Barai P., Martel H., 2009, ApJ, 704, 1002

Gilkis A., Soker N., 2012, MNRAS, 427, 1482

Green J. C. et al., 2012, ApJ, 744, 60

Hamann F., Barlow T. A., Junkkarinen V., Burbidge E. M., 1997, ApJ, 478, 80

Hamann F., Ferland G., 1993, ApJ, 418, 11

Hamann F. W., Barlow T. A., Chaffee F. C., Foltz C. B., Weymann R. J., 2001, ApJ, 550, 142

Hewett P. C., Foltz C. B., 2003, AJ, 125, 1784

Hopkins P. F., Elvis M., 2010, MNRAS, 401, 7

Hopkins P. F., Hernquist L., Cox T. J., Di Matteo T., Robertson B., Springel V., 2006, ApJS, 163, 1

Hopkins P. F., Murray N., Thompson T. A., 2009, MNRAS, 398, 303

Kaastra J. S. et al., 2012, A&A, 539, A117

Kaastra J. S. et al., 2014, Science, 345, 64

Knigge C., Scaringi S., Goad M. R., Cottis C. E., 2008, MNRAS, 386, 1426

Korista K. T. et al., 1995, ApJS, 97, 285

Korista K. T., Bautista M. A., Arav N., Moe M., Costantini E., Benn C., 2008, ApJ, 688, 108

Krolik J. H., 1999, Active galactic nuclei : from the central black hole to the galactic environment

Krolik J. H., Kriss G. A., 2001, ApJ, 561, 684

Landi E., Young P. R., Dere K. P., Del Zanna G., Mason H. E., 2013, ApJ, 763, 86

Levine R., Gnedin N. Y., 2005, ApJ, 632, 727

Lodders K., Palme H., Gail H.-P., 2009, in "Landolt-Börnstein - Group VI Astronomy and Astrophysics Numerical Data and Functional Relationships in Science and Technology Volume, Trümper J. E., ed., p. 44

Lucy A. B., Leighly K. M., Terndrup D. M., Dietrich M., Gallagher S. C., 2014, ApJ, 783, 58

Luo B. et al., 2014, ApJ, 794, 70

Mehdipour M. et al., 2015, A&A, 575, A22

Moe M., Arav N., Bautista M. A., Korista K. T., 2009, ApJ, 706, 525

Murray N., Chiang J., Grossman S. A., Voit G. M., 1995, ApJ, 451, 498

Ostriker J. P., Choi E., Ciotti L., Novak G. S., Proga D., 2010, ApJ, 722, 642

Pancoast A., Brewer B. J., Treu T., Park D., Barth A. J., Bentz M. C., Woo J.-H., 2014, MNRAS, 445, 3073

Park D., Woo J.-H., Denney K. D., Shin J., 2013, ApJ, 770, 87

Peterson B. M. et al., 2013, ApJ, 779, 109

Proga D., Stone J. M., Kallman T. R., 2000, ApJ, 543, 686

Scannapieco E., Oh S. P., 2004, ApJ, 608, 62

Schlafly E. F., Finkbeiner D. P., 2011, ApJ, 737, 103

Schlegel D. J., Finkbeiner D. P., Davis M., 1998, ApJ, 500, 525

Scott J. E. et al., 2004, ApJS, 152, 1

Silk J., Rees M. J., 1998, A&A, 331, L1

Soker N., Meiron Y., 2011, MNRAS, 411, 1803

Steenbrugge K. C. et al., 2005, A&A, 434, 569

Telfer R. C., Kriss G. A., Zheng W., Davidsen A. F., Green R. F., 1998, ApJ, 509, 132

Vestergaard M., Osmer P. S., 2009, ApJ, 699, 800

Vestergaard M., Peterson B. M., 2006, ApJ, 641, 689

Weymann R. J., Carswell R. F., Smith M. G., 1981, ARA&A, 19, 41

Weymann R. J., Morris S. L., Foltz C. B., Hewett P. C., 1991, ApJ, 373, 23

Zubovas K., Nayakshin S., 2014, MNRAS, 440, 2625

Appendix A

Ionic column-density measurements for NGC 5548

The column-density associated with a given ion as a function of the radial velocity v is defined as:

$$N_{\rm ion}(v) = \frac{3.8 \times 10^{14}}{f_j \lambda_j} < \tau_j(v) > \quad ({\rm cm}^{-2}\ {\rm km}^{-1}\ {\rm s}) \tag{A.1}$$

where f_j, λ_j and $< \tau_j(v) >$ are respectively the oscillator strength, the rest wavelength and the average optical depth across the emission source of the line j for which the optical depth solution is derived (see Edmonds et al., 2011). The optical depth solution across a trough is found for a given ion by assuming an absorber model. As shown in Edmonds et al. (2011), the major uncertainty on the derived column-densities comes from the choice of absorption model. In this study we investigate the outflow properties using column-densities derived from three common absorber models.

Assuming a single, homogeneous emission source of intensity F_0, the simplest absorber model is the one where a homogeneous absorber parameterized by a single optical depth fully covers the photon source. In that case, known as the apparent optical depth scenario (AOD), the optical depth of a line j as a function of the radial velocity v in the trough is simply derived

by the inversion of the Beer-Lambert law: $\tau_j(v) = -ln(F_j(v)/F_0(v))$, where $F_j(v)$ is the observed intensity of the line.

Early studies of AGN outflows pointed out the inadequacy of such an absorber model, specifically its inability to account for the observed departure of measured optical depth ratio between the components of typical doublet lines from the expected laboratory line strength ratio $R = \lambda_i f_i/\lambda_j f_j$. Two parameter absorber models have been developed to explain such discrepancies. The partial covering model (e.g. Hamann et al., 1997; Arav et al., 1999a; Arav, Korista & de Kool, 2002; Arav et al., 2005) assumes that only a fraction C of the emission source is covered by absorbing material with constant optical depth τ. In that case, the intensity observed for a line j of a chosen ion can be expressed as

$$F_j(v) = F_0(v)(1 + C(v) * (e^{-\tau j(v)} - 1)). \tag{A.2}$$

Our third choice are inhomogeneous absorber models. In that scenario, the emission source is totally covered by a smooth distribution of absorbing material across its spatial dimension x. Assuming the typical power law distribution of the optical depth $\tau(x) = \tau_{\max} x^a$ (de Kool, Korista & Arav, 2002; Arav et al., 2005, 2008), the observed intensity observed for a line j of a chosen ion is given by

$$F_j(v) = F_0(v) \int_0^1 e^{-\tau_{\max,j}(v) x^{a(v)}} dx \tag{A.3}$$

Once the line profiles have been binned on a common velocity scale (we choose a resolution $dv = 20$ km s^{-1}, slightly lower than the resolution of COS), a velocity dependent solution can be obtained for the couple of parameters (C, τ_j) or $(a, \tau_{\max})$ of both absorber models as long as one observes at least two lines from a given ion, sharing the same lower energy level. Once the velocity dependent solution is computed, the corresponding column density is derived using Equation (A.1) where $< \tau_j(v) >= C_{\rm ion}(v)\tau_j(v)$ for the partial covering model and $< \tau_j(v) >= \tau_{{\rm max},j}(v)/(a_{\rm ion}(v) + 1)$ for the power law distribution. Note that the AOD solution can be computed for any line (singlet or multiplet), without further assumption on

the model, but will essentially give a lower limit on the column-density when the expected line strength ratio observed is different from the laboratory value.

Table A.1: Observations and flux values for all epochs

Epoch	Observing Dates	Instrument	Grating	Exposure	avg F^a_{1350}	fit F^b_{1350}	fit α^c
2013_v1	2013/June/22	HST:COS	G130M	1.8ks	1.95 ± 0.36		
			G160M	2.1ks			
2013_v2	2013/July/12	HST:COS	G130M	5.0ks	2.22 ± 0.34		
			G160M	2.2ks			
2013_v3	2013/July/24	HST:COS	G130M	2.0ks	3.70 ± 0.44		
			G160M	2.2ks			
2013_v4	2013/July/30	HST:COS	G130M	2.0ks	3.51 ± 0.44		
			G160M	2.2ks			
2013_v5	2013/August/01	HST:COS	G130M	2.0ks	3.28 ± 0.40		
			G160M	2.2ks			
2013_v6	2013/December/20	HST:COS	G130M	2.0ks	3.26 ± 0.40	3.14 ± 0.02	-0.79 ± 0.03
			G160M	2.2ks			
2013_v345	2013/July/24 to 2013/August/01	HST:COS	G130M	6.0ks	3.51 ± 0.24	3.44 ± 0.03	-0.776 ± 0.014
			G160M	6.6ks			
2013_v12345	2013/June/22 to 2013/August/01	HST:COS	G130M	12.8ks	3.11 ± 0.19	3.051 ± 0.015	-0.736 ± 0.026
			G160M	11.0ks			
2011	2011/June/16	HST:COS	G130M	1.9ks	6.17 ± 0.52	6.13 ± 0.05	-0.86 ± 0.07
			G160M	2.4ks			
2004	2004/February/10 to 2004/February/13	HST:STIS	E140M	52.2ks	0.25 ± 0.07	0.203 ± 0.017	-1.86 ± 0.29
2002	2002/January/22 to 2002/January/23	HST:STIS	E140M	15.3ks	1.80 ± 0.18	1.80 ± 0.04	-1.46 ± 0.06
1998	1998/March/11	HST:STIS	E140M	4.75ks	6.41 ± 0.75	6.43 ± 0.12	-1.51 ± 0.13

[a]Flux at rest-frame 1350Å in units of 10^{-14} erg s^{-1} cm^{-2} Å^{-1}

[b]Flux from a power-law fit of the form $F(\lambda) = F_{1350}(\lambda/1350)^{\alpha}$

[c]Spectral index from the above power-law fit

Table A.2: UV column-densities for the outflow components in NGC 5548

Ion	v_1 $[-1450,-850]^a$	v_2 $[-850,-750]$	v_3 $[-750,-540]$	v_4 $[-540,-360]$	v_5 $[-360,-80]$	v_6 $[-80,+50]$
			Epoch 2013			
H I	$>14.39^b$	>13.86	>14.28	>14.40	>14.00	>13.00
C II	>14.52	<12.81	$13.67^{+0.1}_{-0.1}$	<13.24	<13.40	<13.00
C III$^*_{J=0}$	$14.03^{+0.02}_{-0.02}$					
C III$^*_{J=2}$	$14.64^{+0.02}_{-0.02}$					
C IV	>14.60	$14.00^{+0.3}_{-0.1}$	>14.30	>14.30	>14.10	>13.70
N V	>14.90	$13.90^{+0.2}_{-0.2}$	>14.90	>14.80	>14.60	>14.10
Al II	>13.05					
Si II	$14.30^{+0.18}_{-0.3}$	<11.80	<12.00	<11.90	<11.40	<12.10
Si III	>13.70	<12.00	$13.10^{+0.3}_{-0.3}$	<12.20	$12.20^{+0.2}_{-0.2}$	<11.50
Si IV	>14.08	$12.30^{+0.2}_{-0.2}$	$13.88^{+0.2}_{-0.2}$	<13.00	$13.13^{+0.2}_{-0.2}$	<12.30
P III	$14.04^{+0.16}_{-0.06}$					
P V	$14.15^{+0.5}_{-0.15}$					
S III	$15.00^{+0.30}_{-0.22}$					
Fe III	$14.70^{+0.30}_{-0.30}$					
			Epoch 2011			
H I	>14.34	>13.80	>14.28	>14.33	>13.83	>12.90
C IV	>14.20	>13.70	>14.30	$14.40^{+0.2}_{-0.2}$	>13.83	>13.03
N V	>14.59	>13.95	>14.65	>14.77	>14.43	>13.84
Si III	<12.20	<11.50	<11.98	<11.84	<11.55	<11.59
Si IV	<13.06	<12.54	<12.66	<12.70	<12.53	<12.37
			Epoch 2004			
H I	>13.94	>13.82	>14.20	>14.44	>14.15	>12.41
C IV	>14.59	>13.83	>13.95	>14.25	>14.20	>13.16
N V	>14.65	>13.83	>14.20	>14.35	>13.75	>13.20
Si III	>13.61	>12.47	>13.29	>12.41	>12.66	>12.33
Si IV	>14.18	>12.91	>13.65	>12.71	>13.32	>12.76
			Epoch 2002			
H I	>14.34	>13.91	>14.29	>14.46	>13.91	>13.20
C IV	>14.08	>13.54	>13.95	$14.30^{+0.2}_{-0.2}$	>13.60	>13.23
N V	>14.54	$13.87^{+0.2}_{-0.2}$	$14.50^{+0.2}_{-0.2}$	>14.76	>14.12	>13.21
Si III	<12.66	<11.80	<11.97	<11.91	<12.14	<11.97
Si IV	<13.31	<12.39	<12.81	<12.74	<13.13	<12.58
			Epoch 1998			
H I	>14.06	>13.66	>14.28	>14.36	>13.75	>12.96
C IV	<13.69	>13.25	>13.59	>14.47	<13.09	<13.00
N V	<13.99	>13.89	>14.19	>14.88	>14.13	<13.98
Si III	<12.83	<12.14	<12.46	<12.18	<12.57	<12.41
Si IV	<13.39	<12.83	<12.93	<12.69	<12.89	<12.13

[a] Integration limits in km s^{-1}.

[b] Lower limit log column-densities given in units of cm^{-2} are shown in blue.
Upper limits are likewise shown in red.

Figure A.1: Plot of the 2013 spectrum of NGC 5548. The vertical axis is the flux in units of 10^{-14} erg s^{-1} cm^{-2} Å^{-1}, and the quasar-rest-frame and observer-frame wavelengths are given in Angstroms on the top and bottom of each sub-plot, respectively. Each of the six kinematic components of the outflow shows absorption troughs from several ions. We place a vertical mark at the expected center of each absorption trough (following the velocity template of Si IV and N V) and state the ion, rest-wavelength and component number (C_1–C_6). We also assign a color to each component number that ranges from blue (C_1) to red (C_6). Absorption lines from the ISM are likewise marked in black with dashed lines.

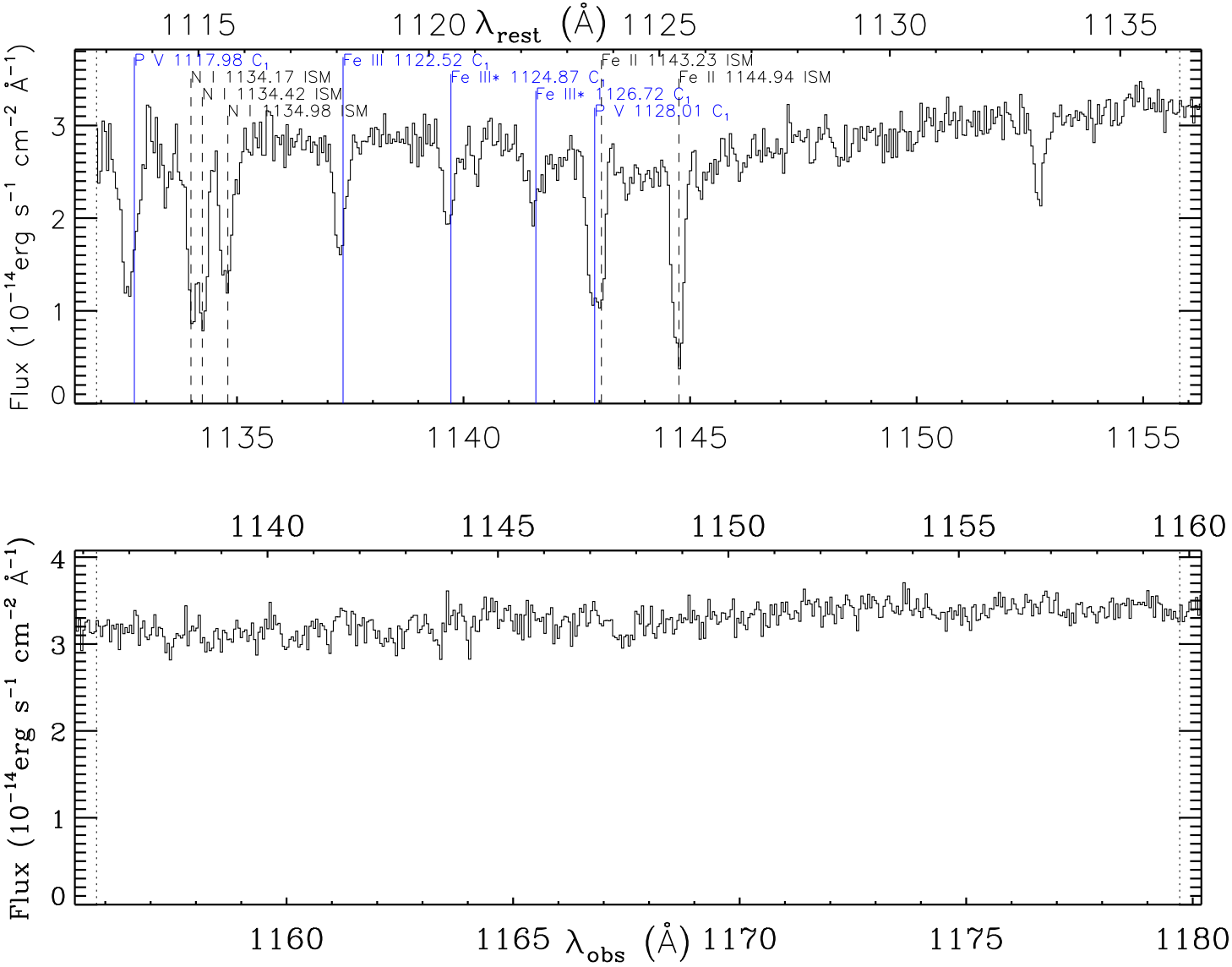

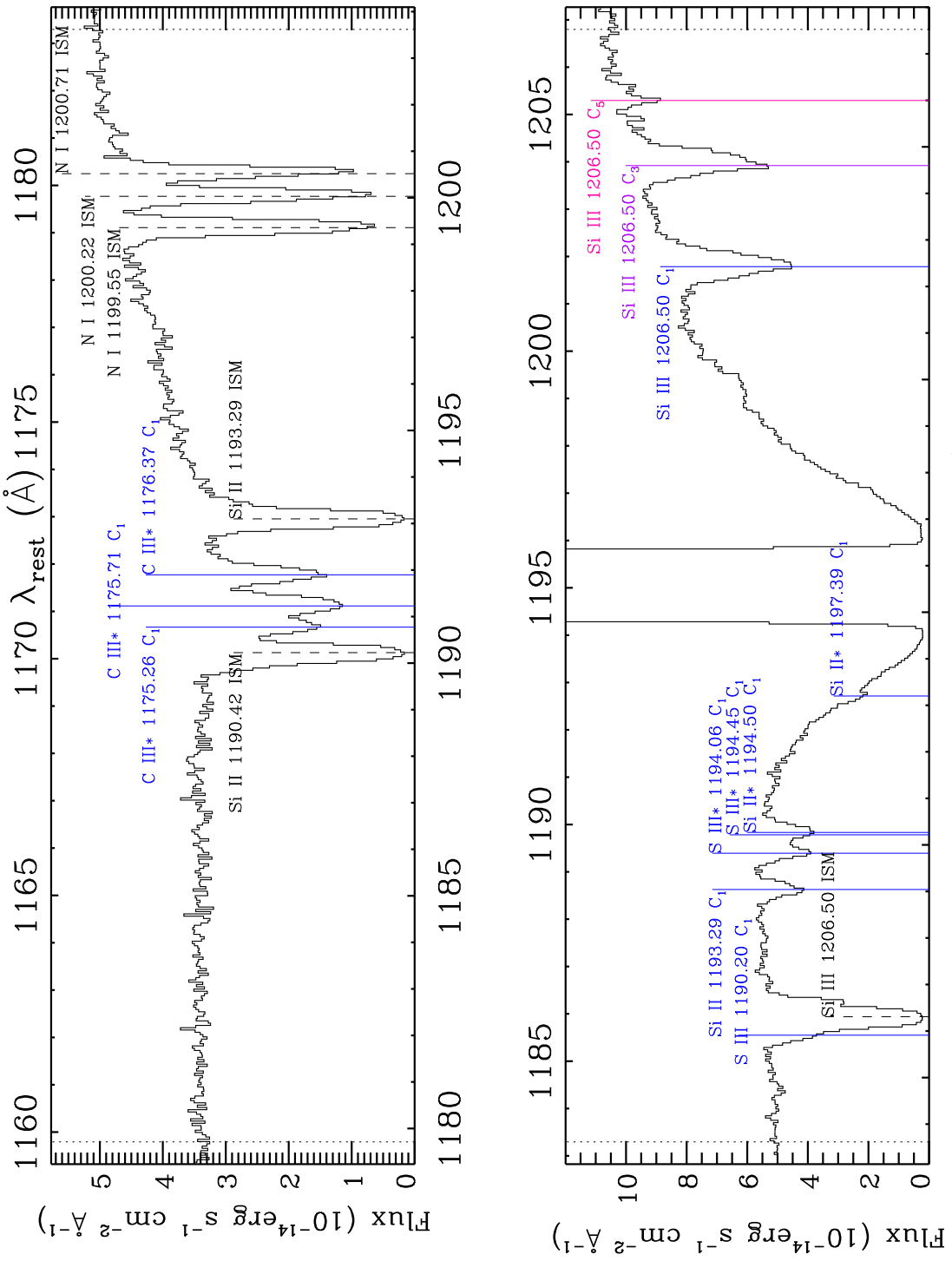

Figure A.1: *continued*

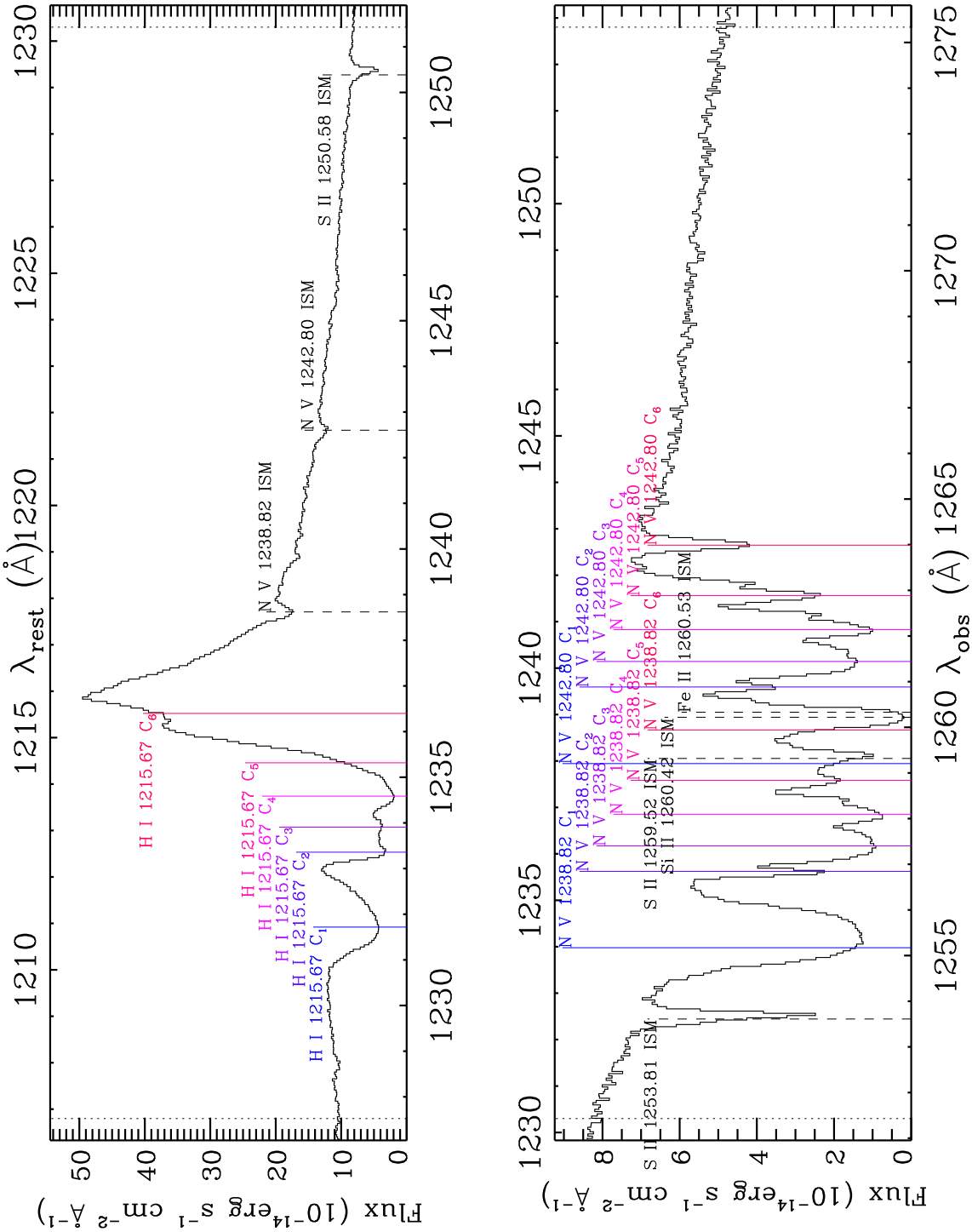

Figure A.1: *continued*

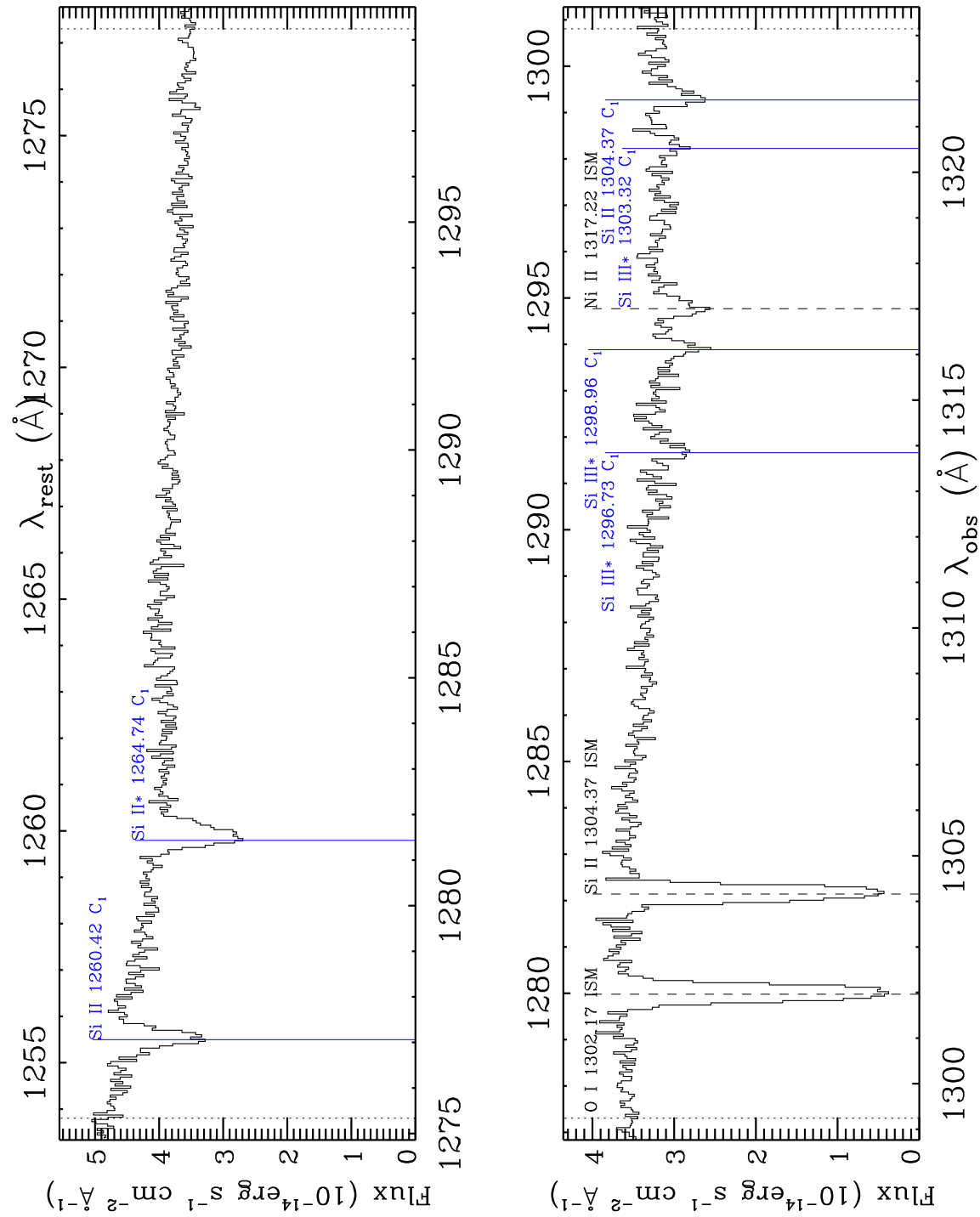

Figure A.1: *continued*

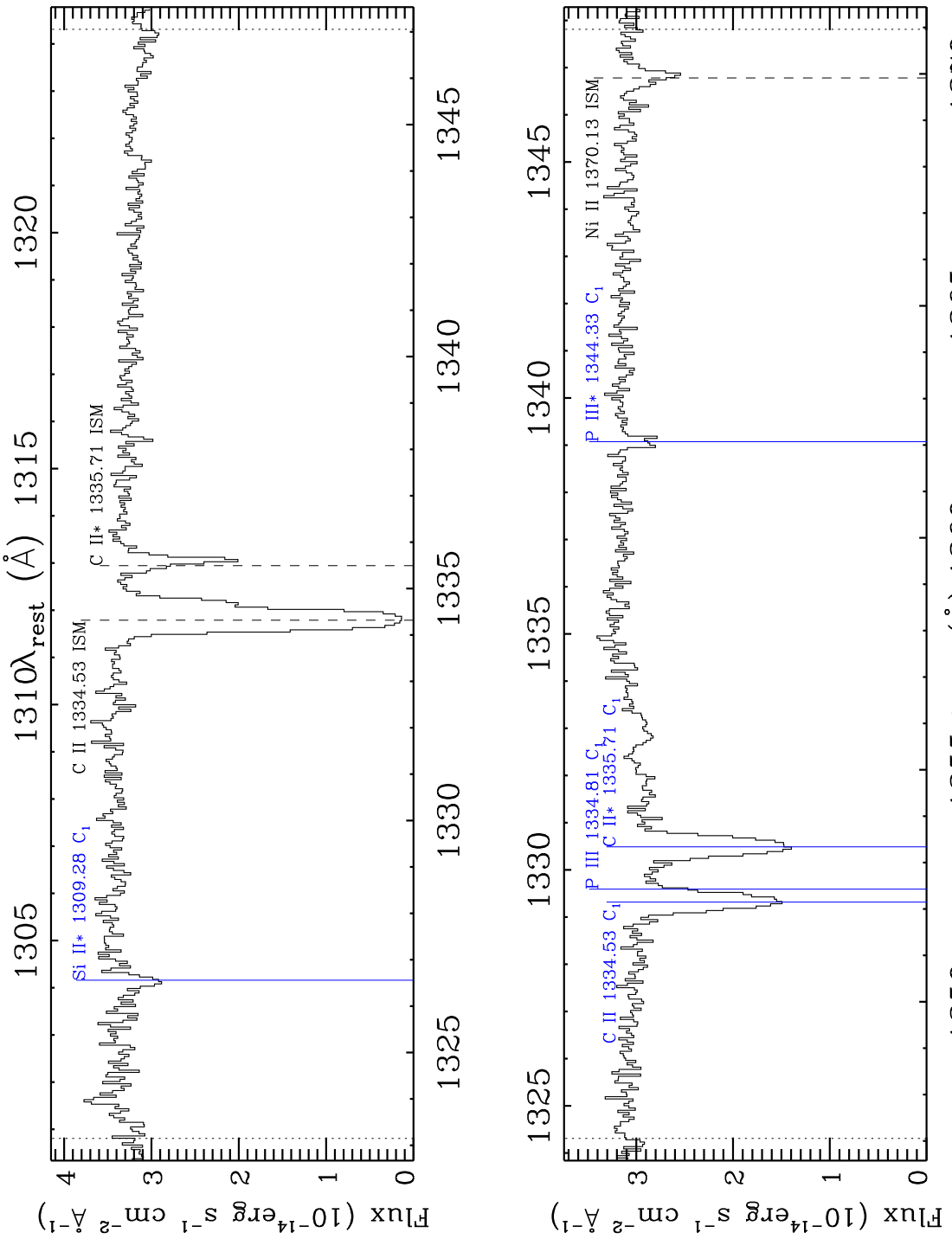

Figure A.1: *continued*

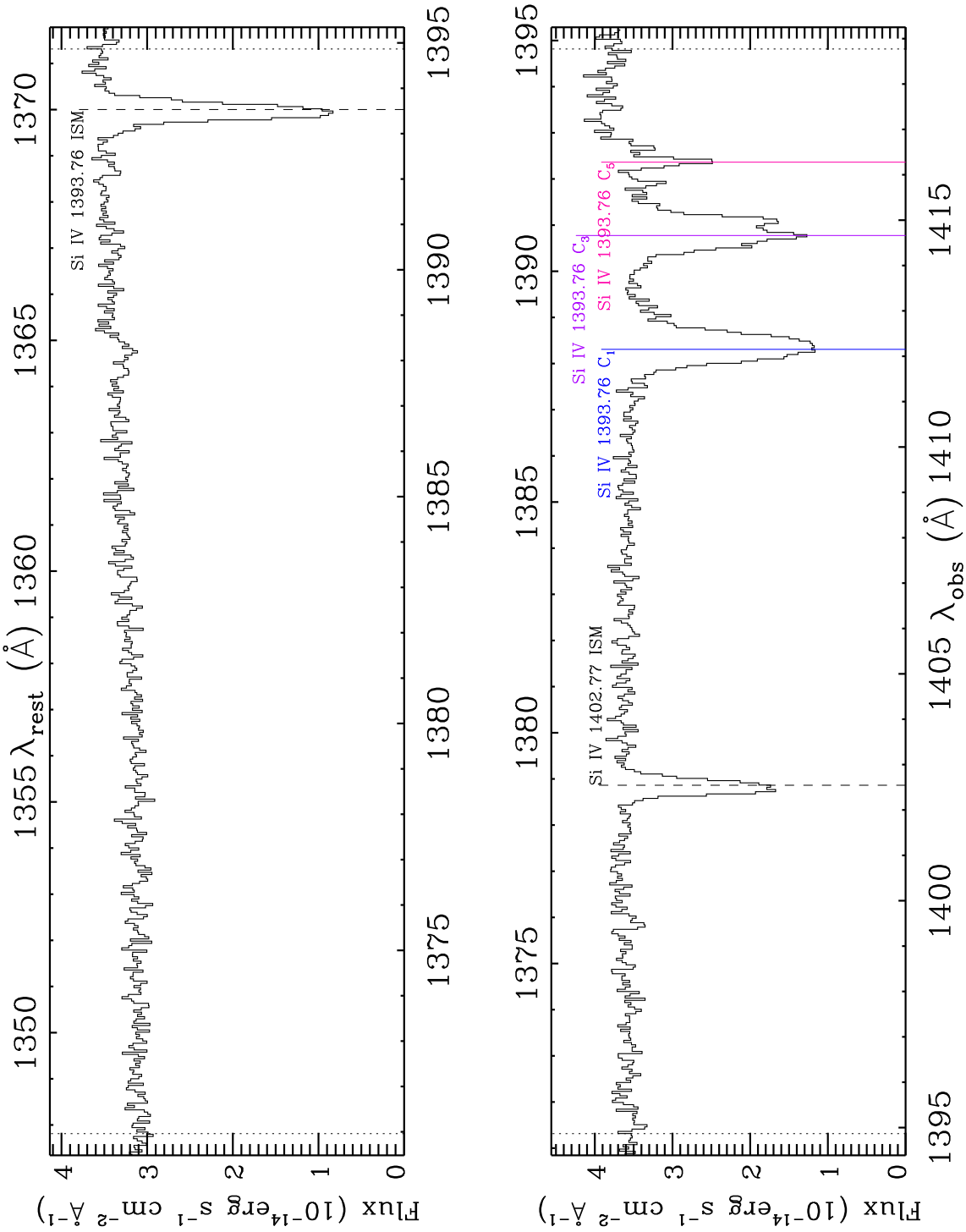

Figure A.1: *continued*

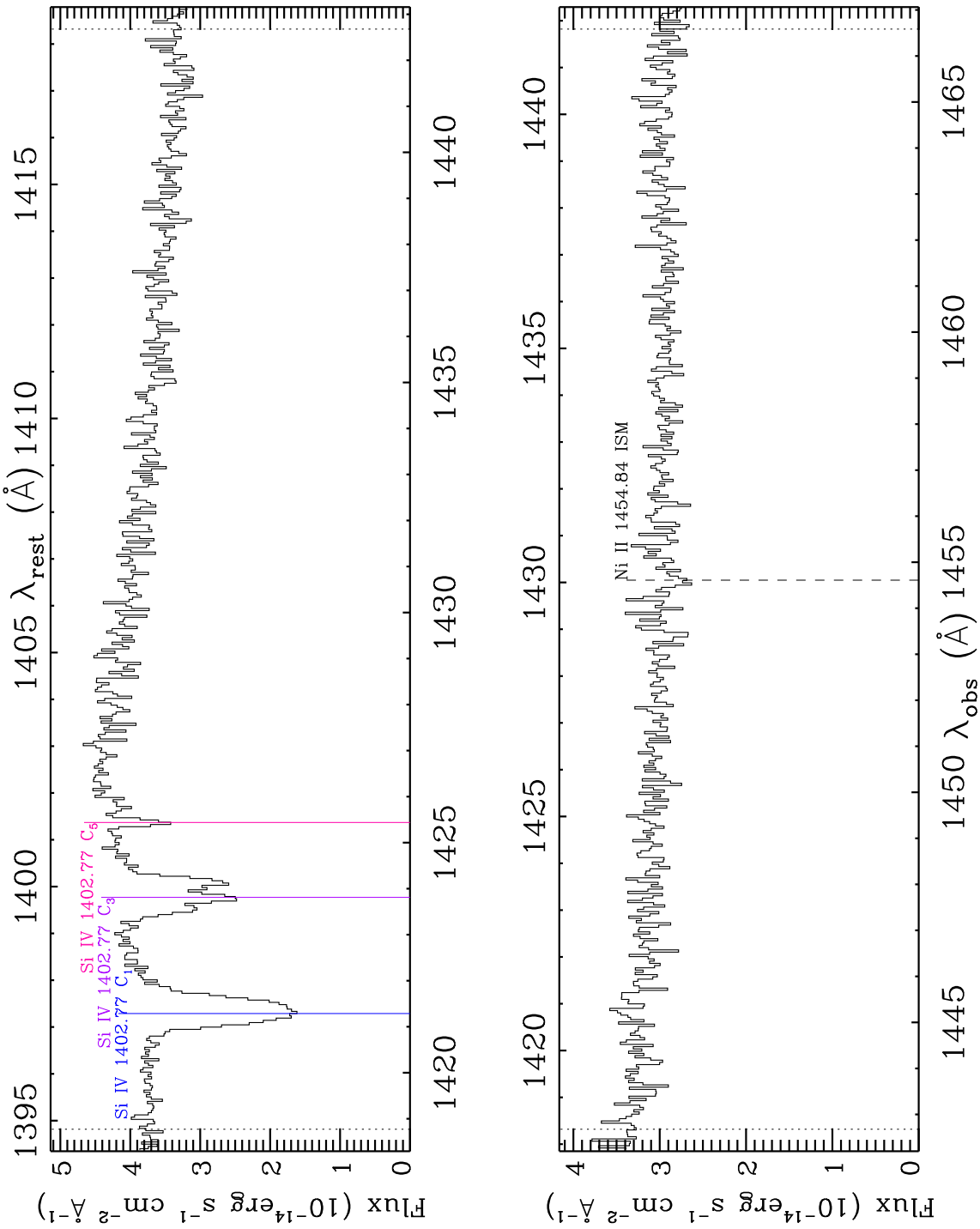

Figure A.1: *continued*

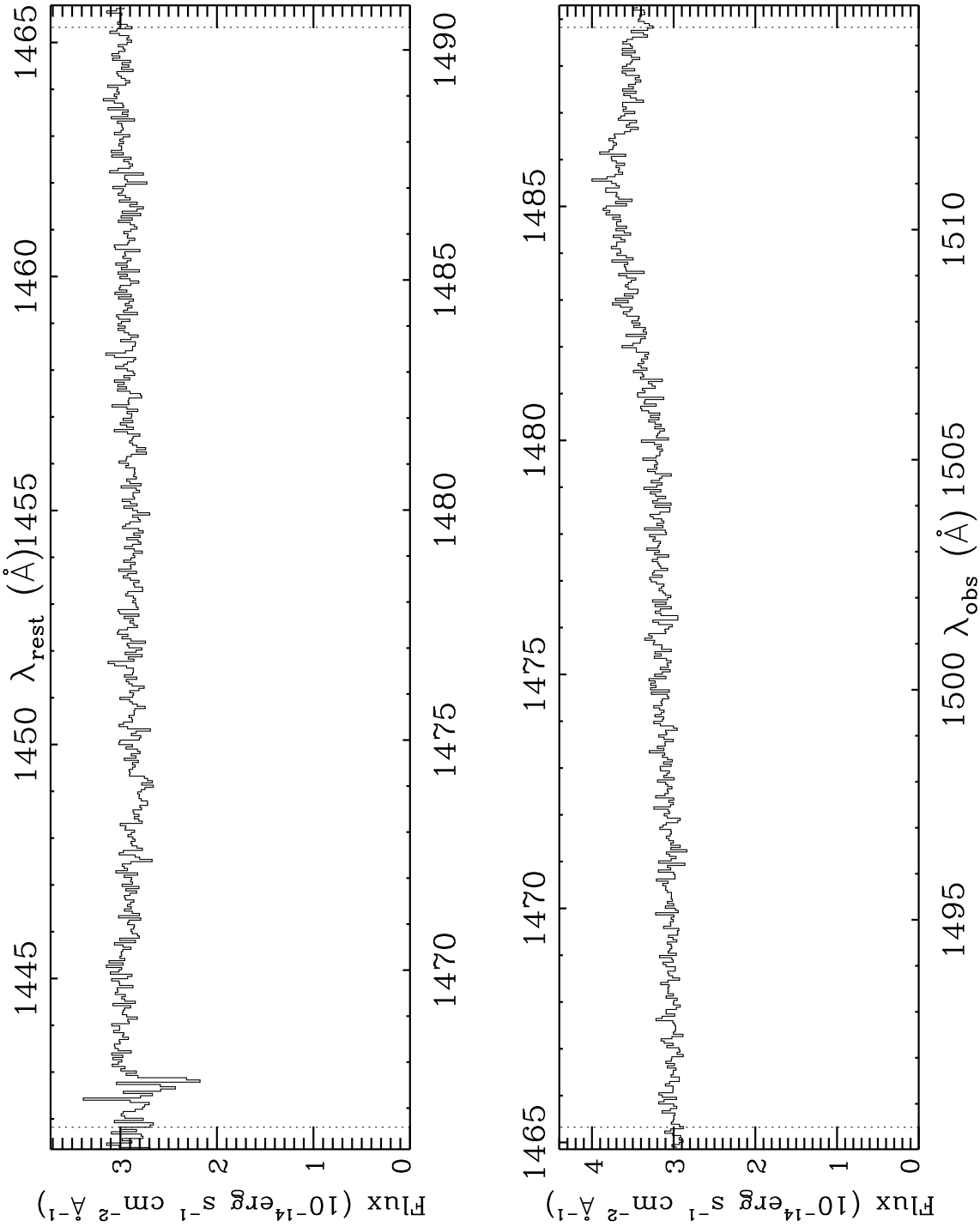

Figure A.1: *continued*

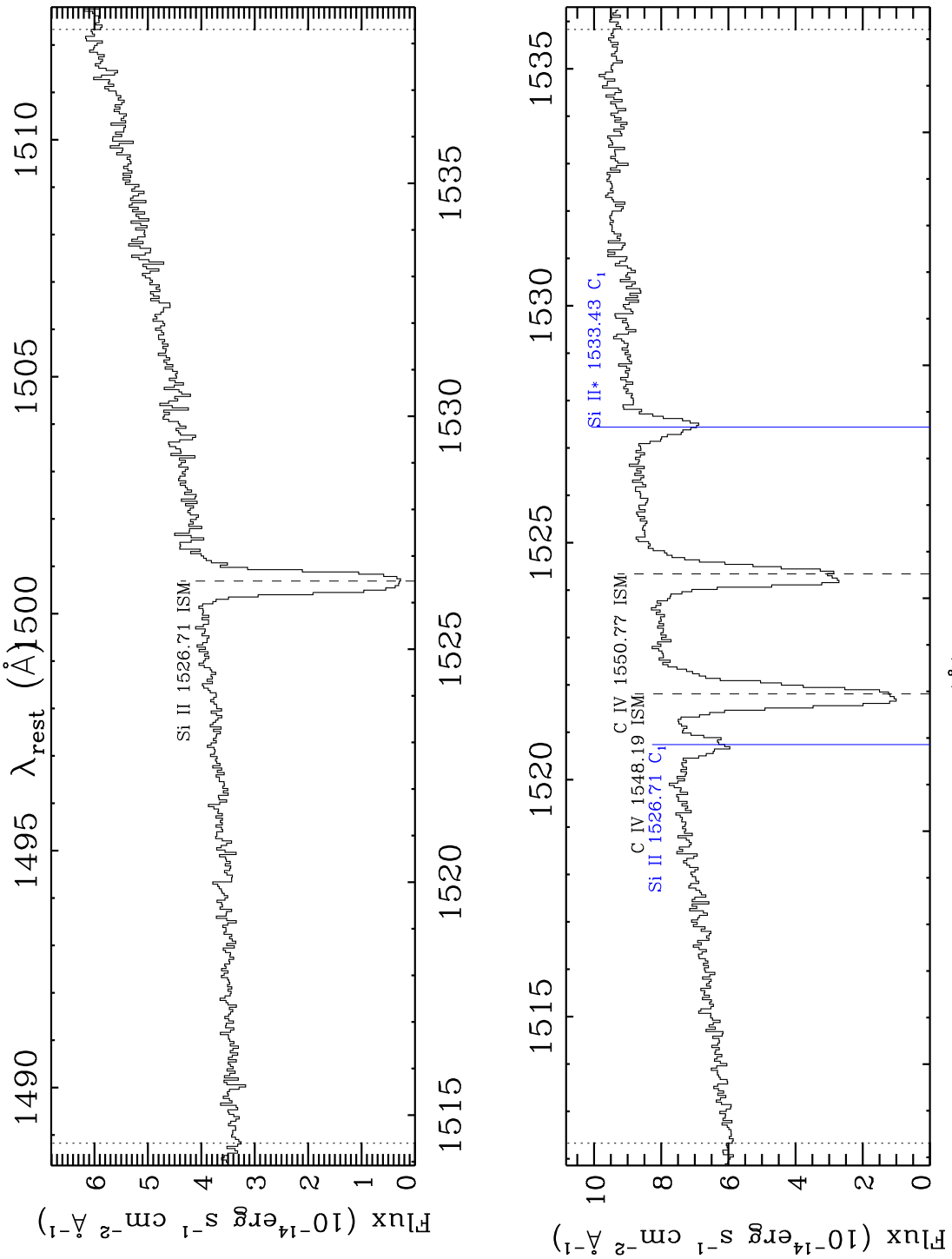

Figure A.1: *continued*

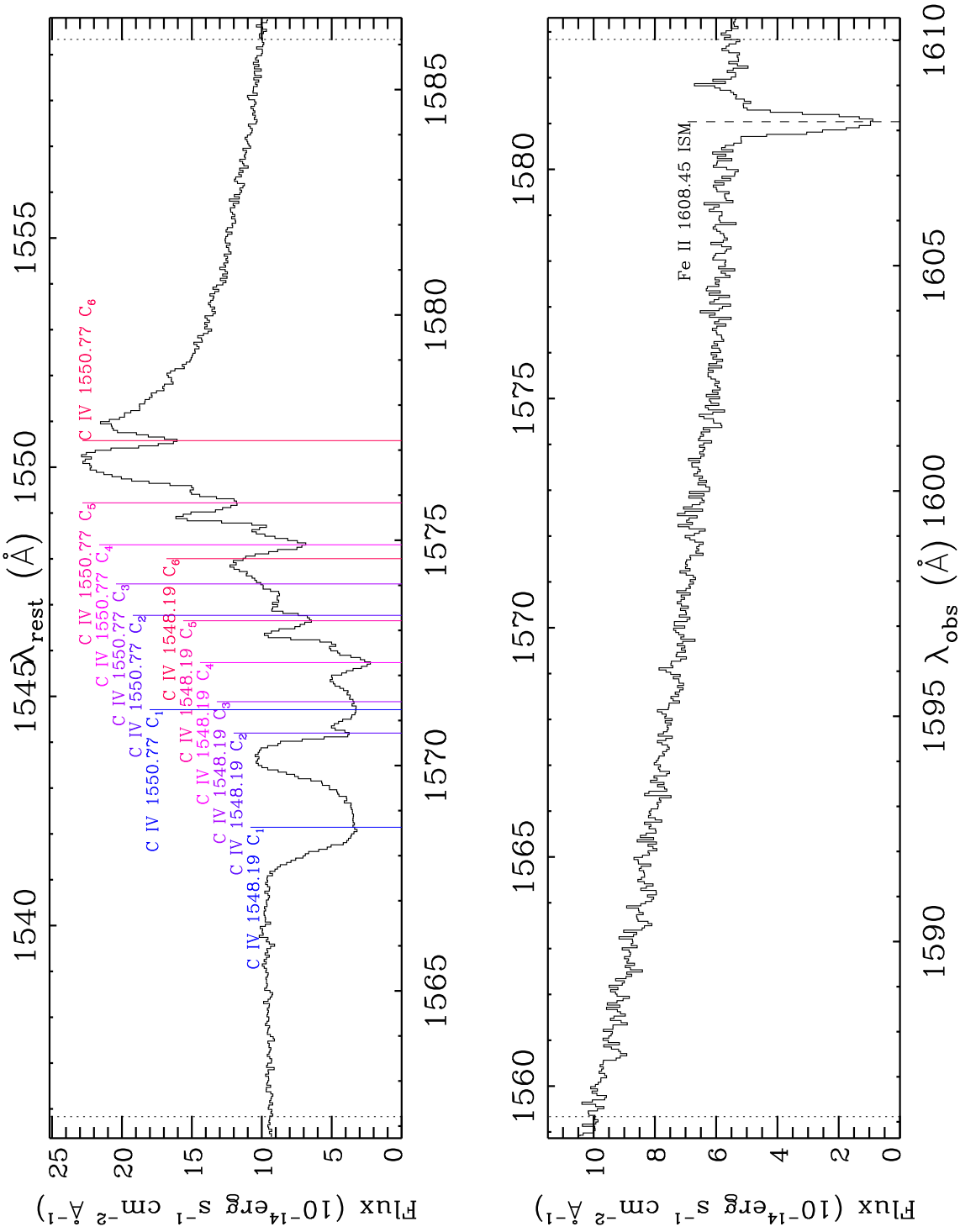

Figure A.1: *continued*

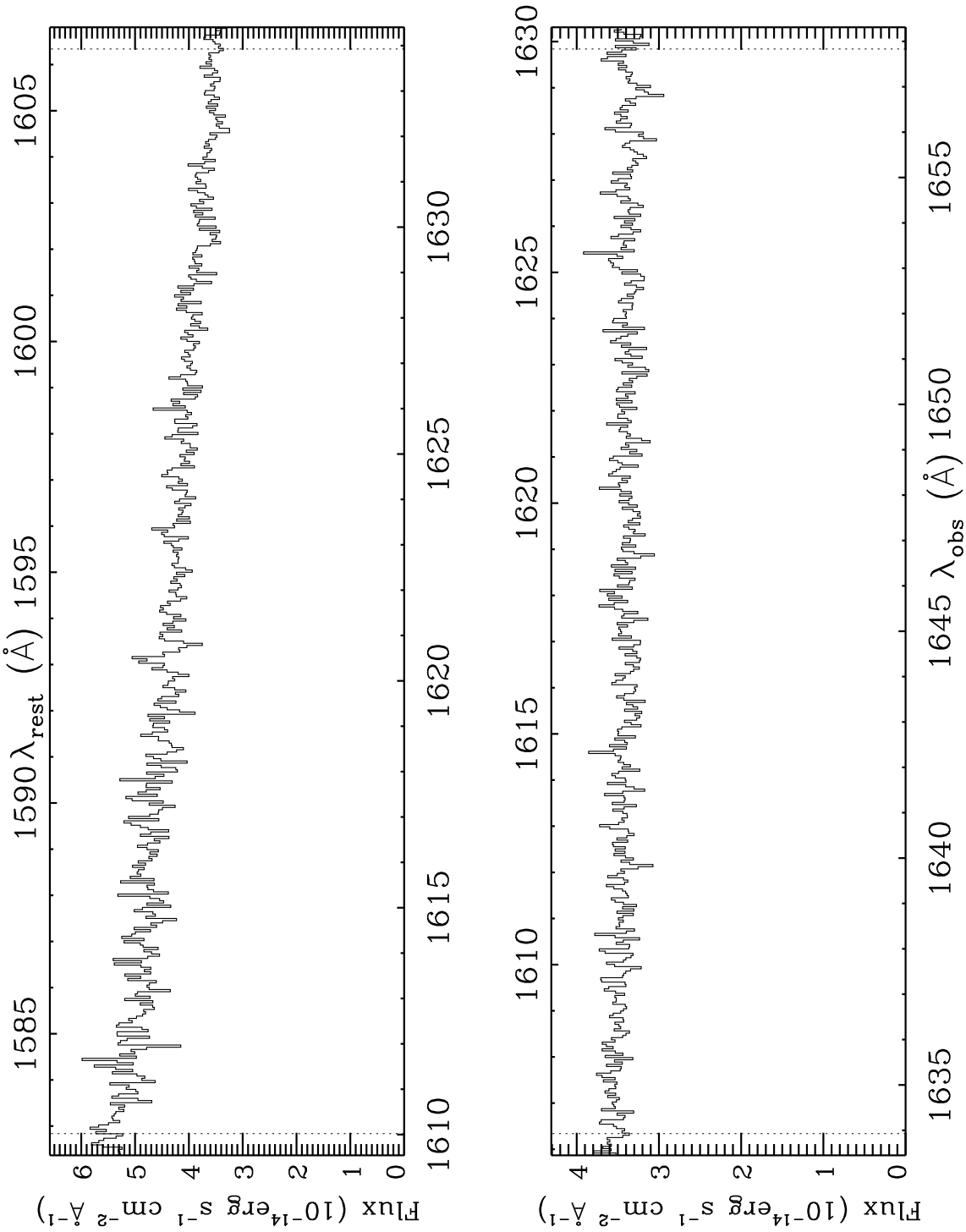

Figure A.1: *continued*

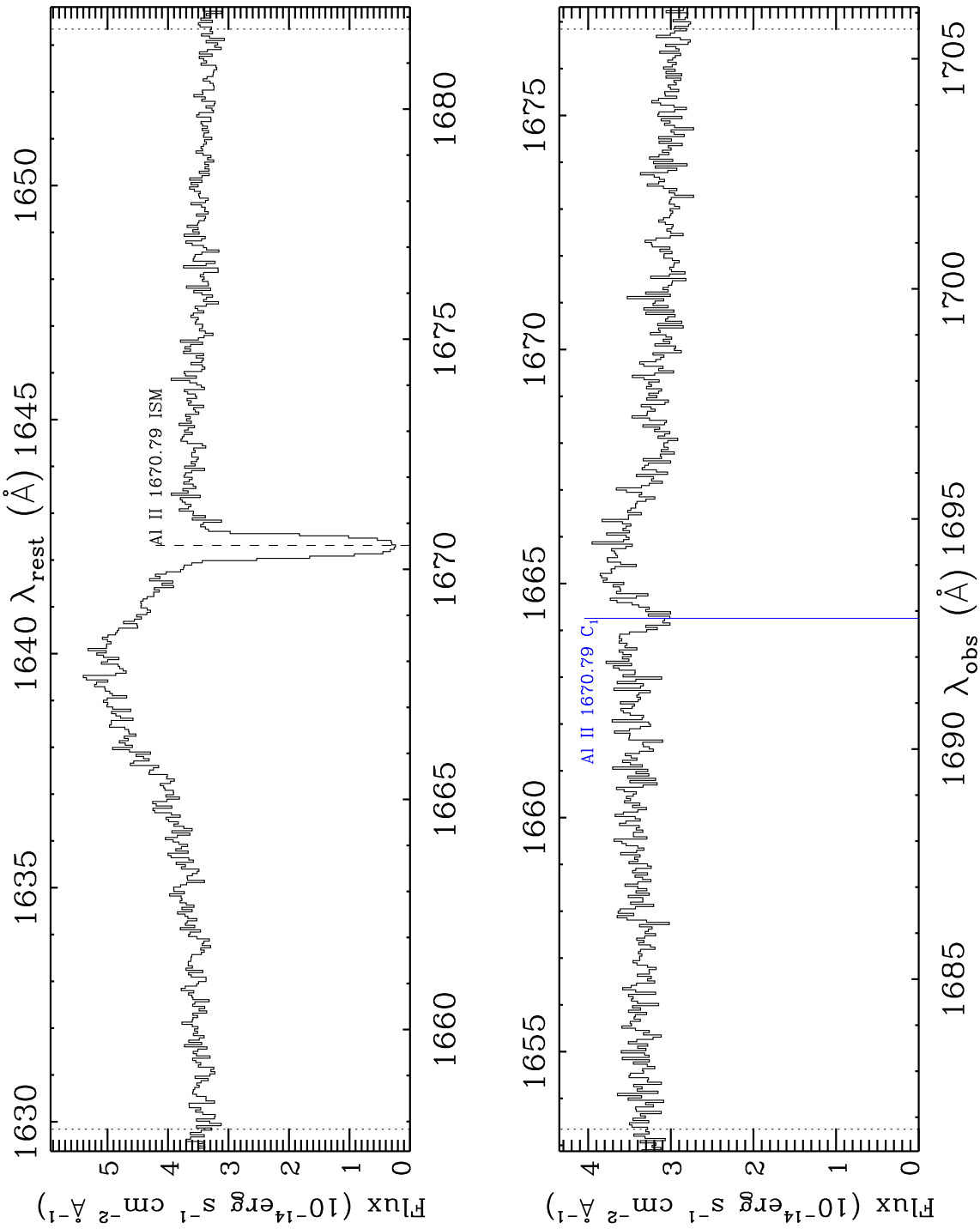

Figure A.1: *continued*

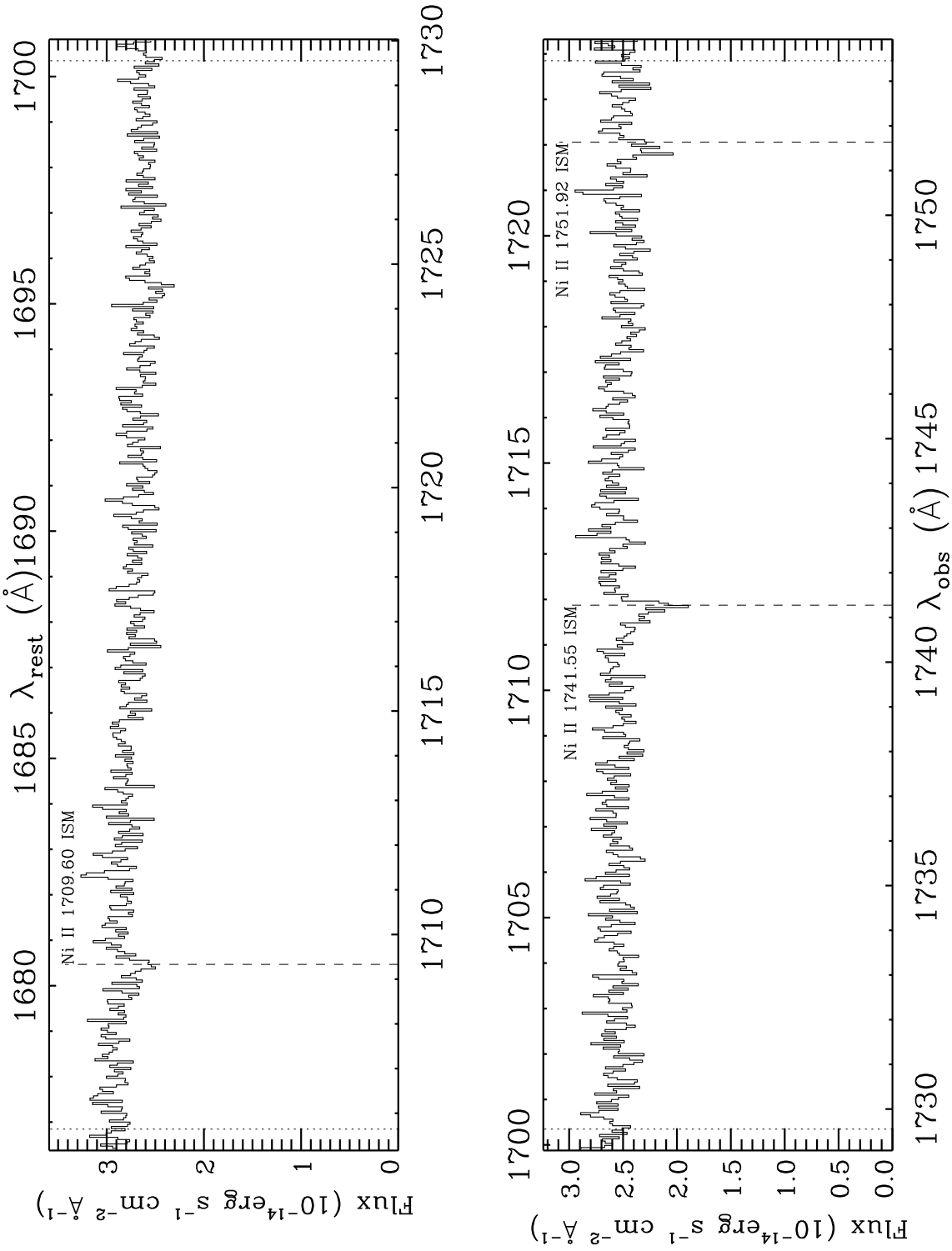

Figure A.1: *continued*

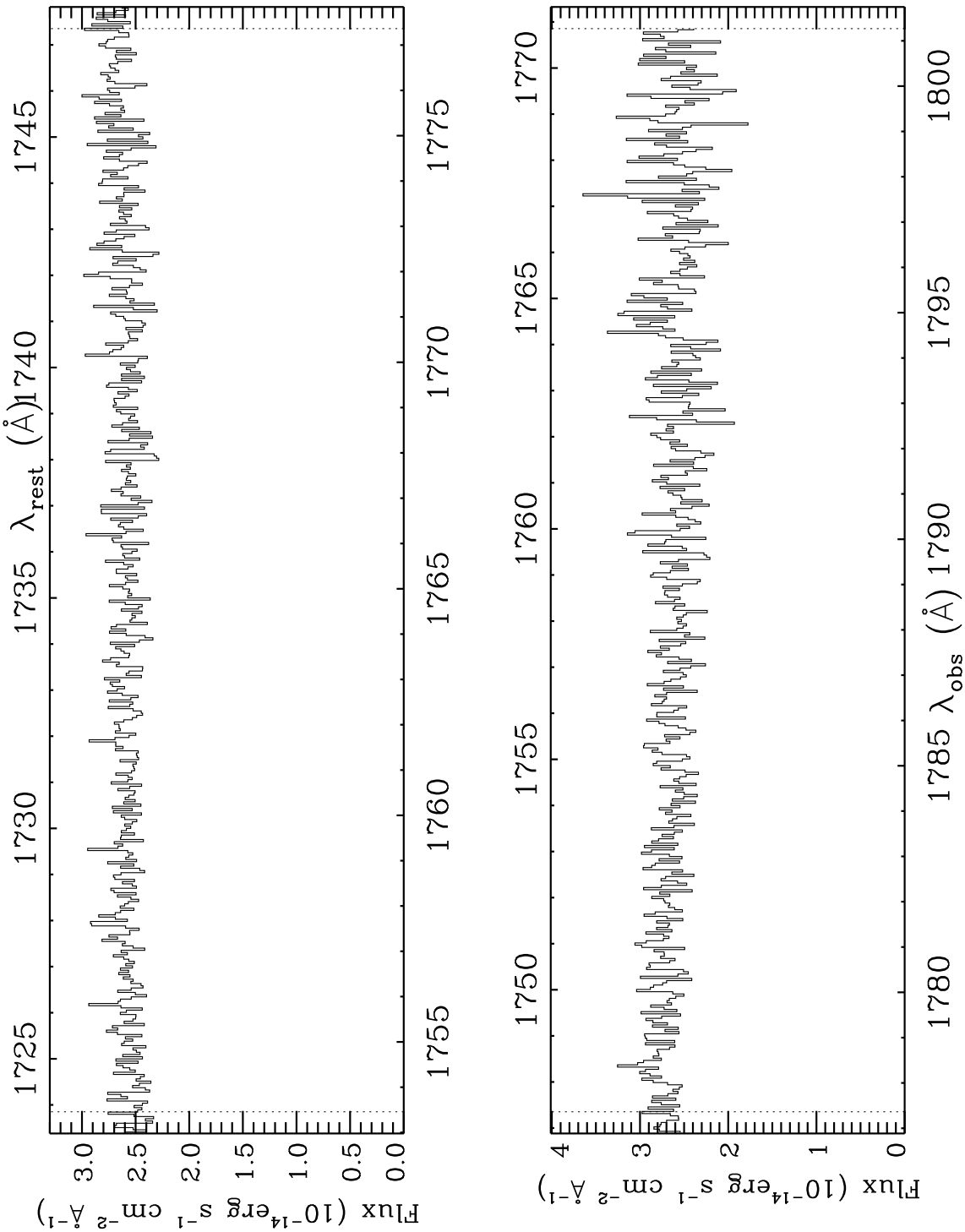

Figure A.1: *continued*

Figure A.2: A plot of the spectrum of NGC 5548 during the five epochs of observation. The 2013 spectrum is obtained by co-adding visits 1 through 5. Spectral regions where absorption troughs from five ions are shown in sub-plots (a) through (e) and the six kinematic components associated with such absorption are labelled C_1 through C_6.

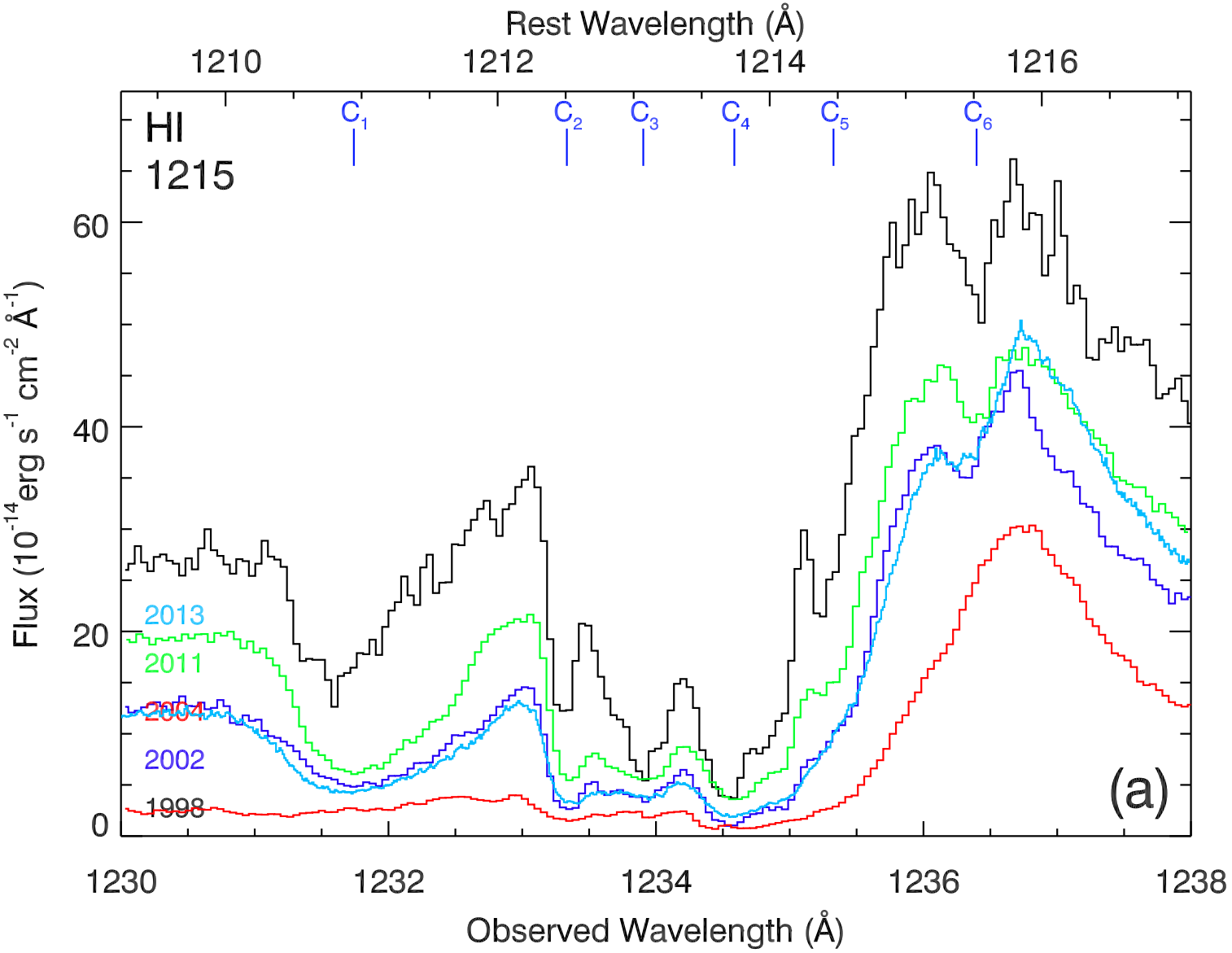

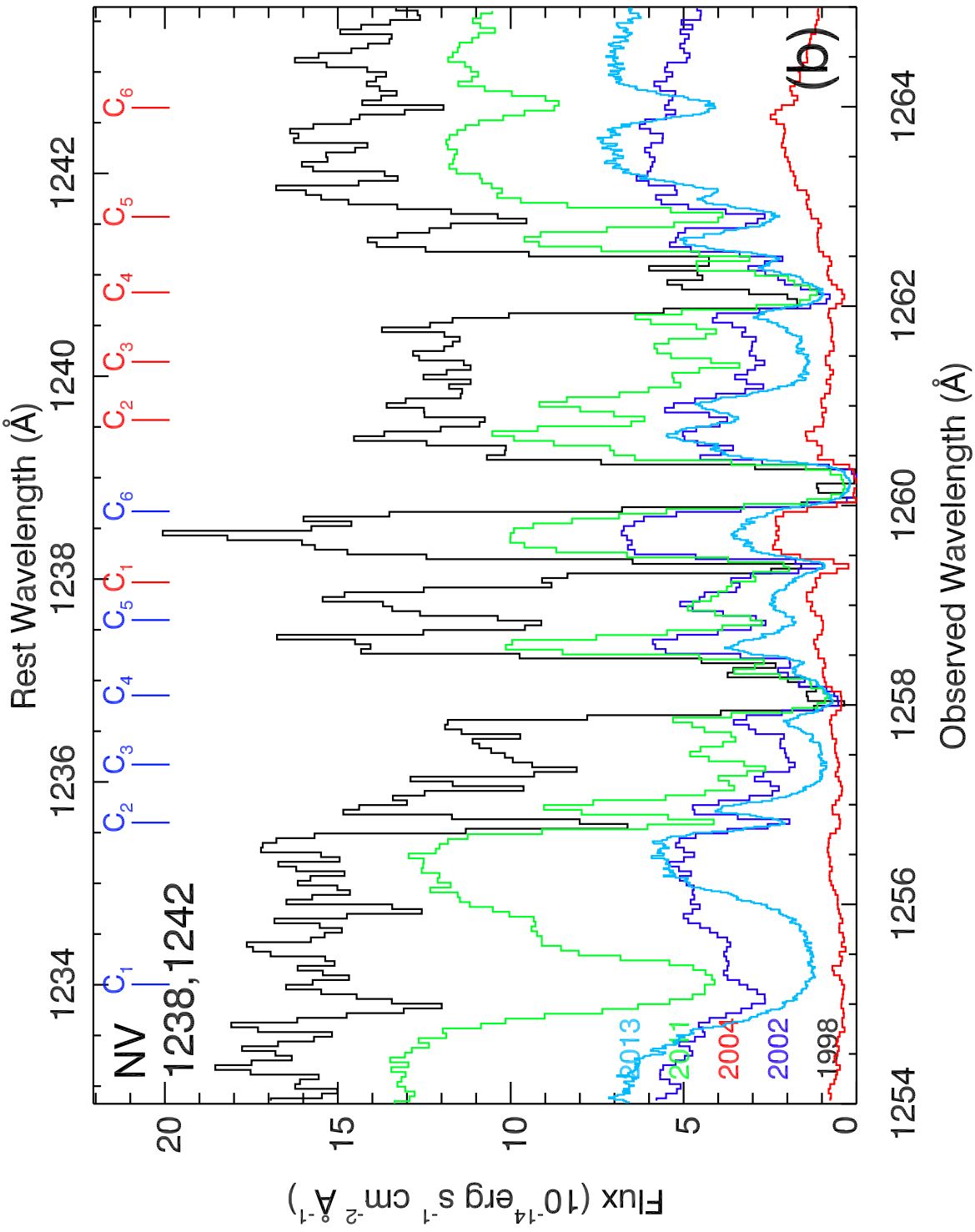

Figure A.2: *continued*

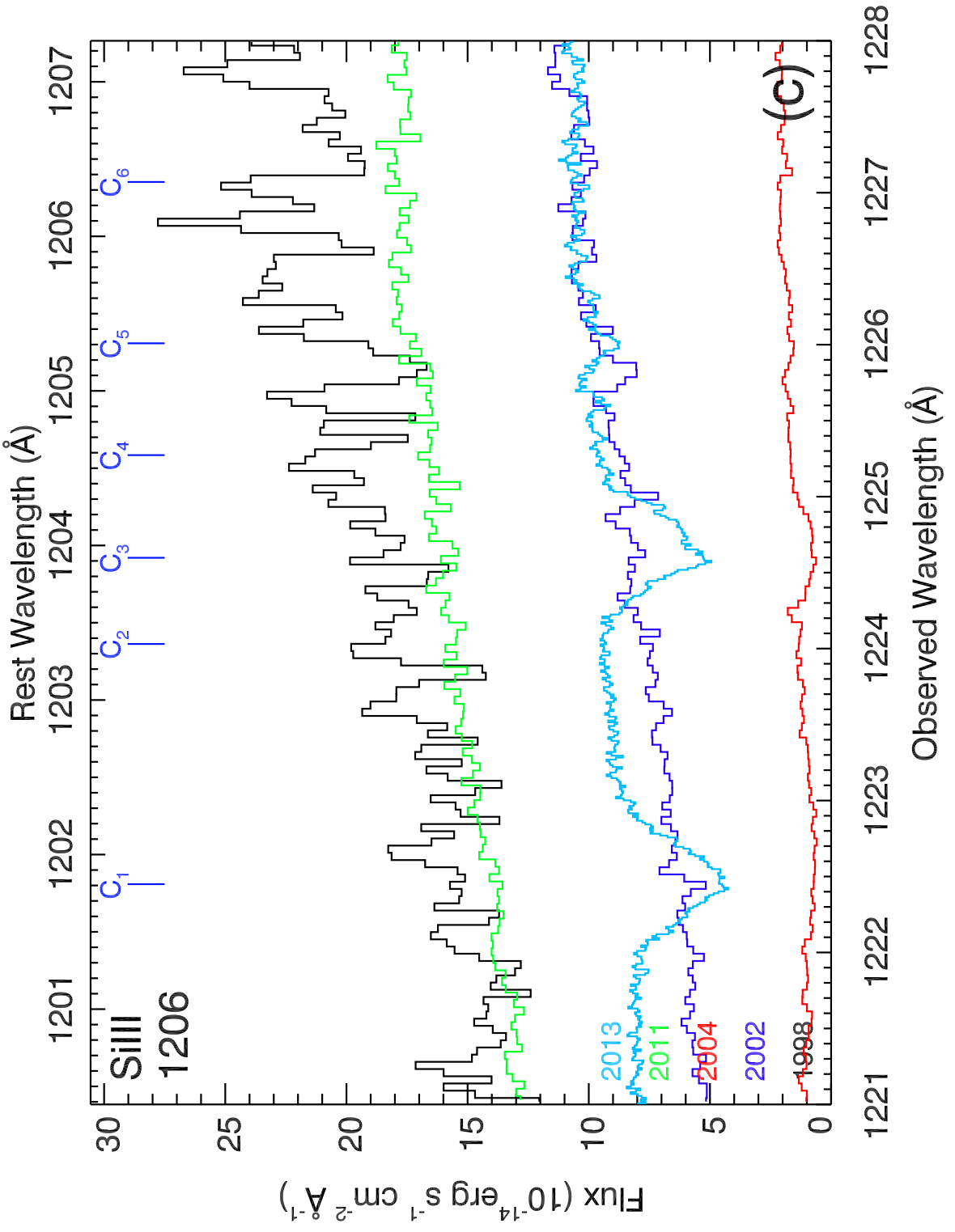

Figure A.2: *continued*

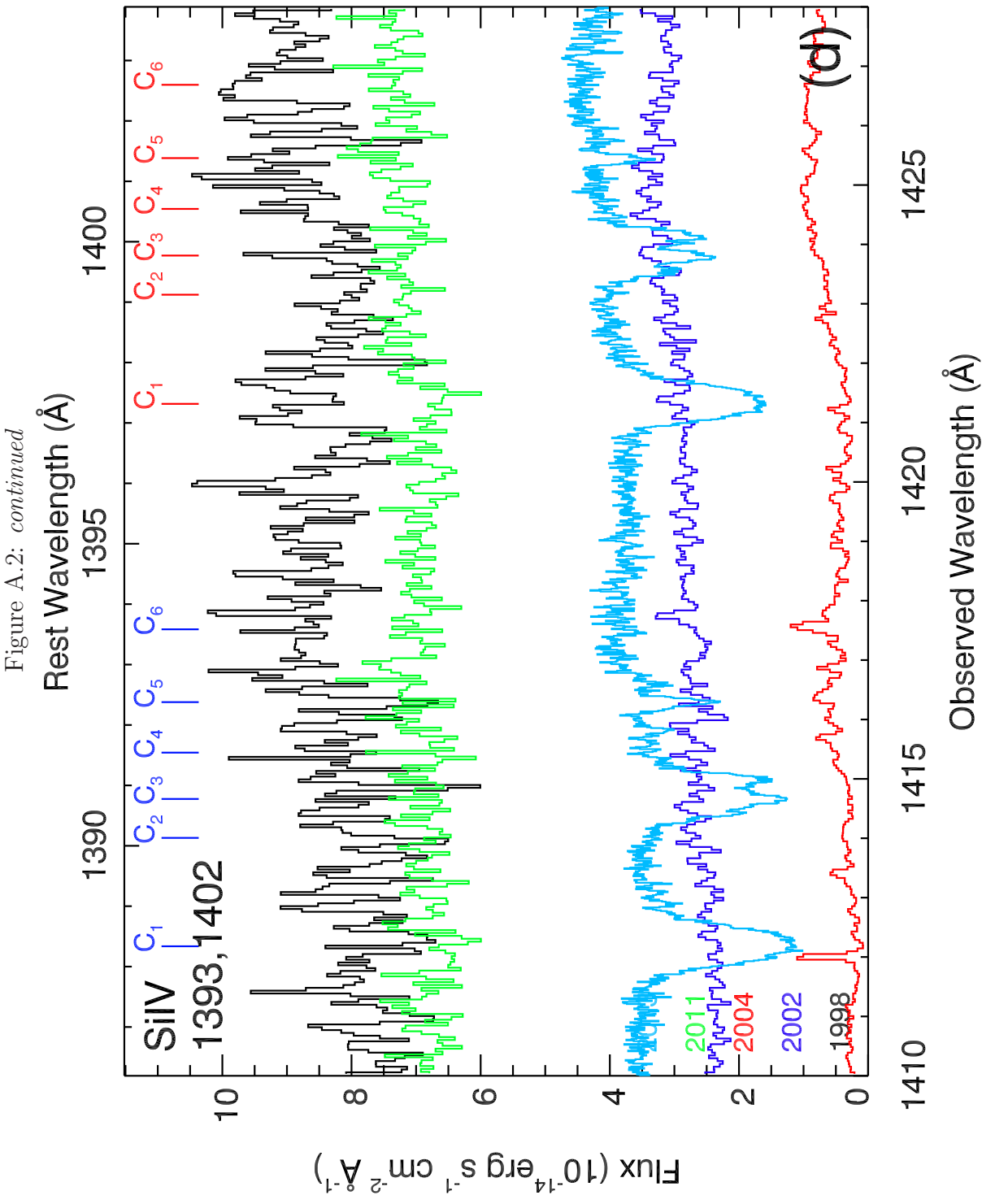

Figure A.2: *continued*

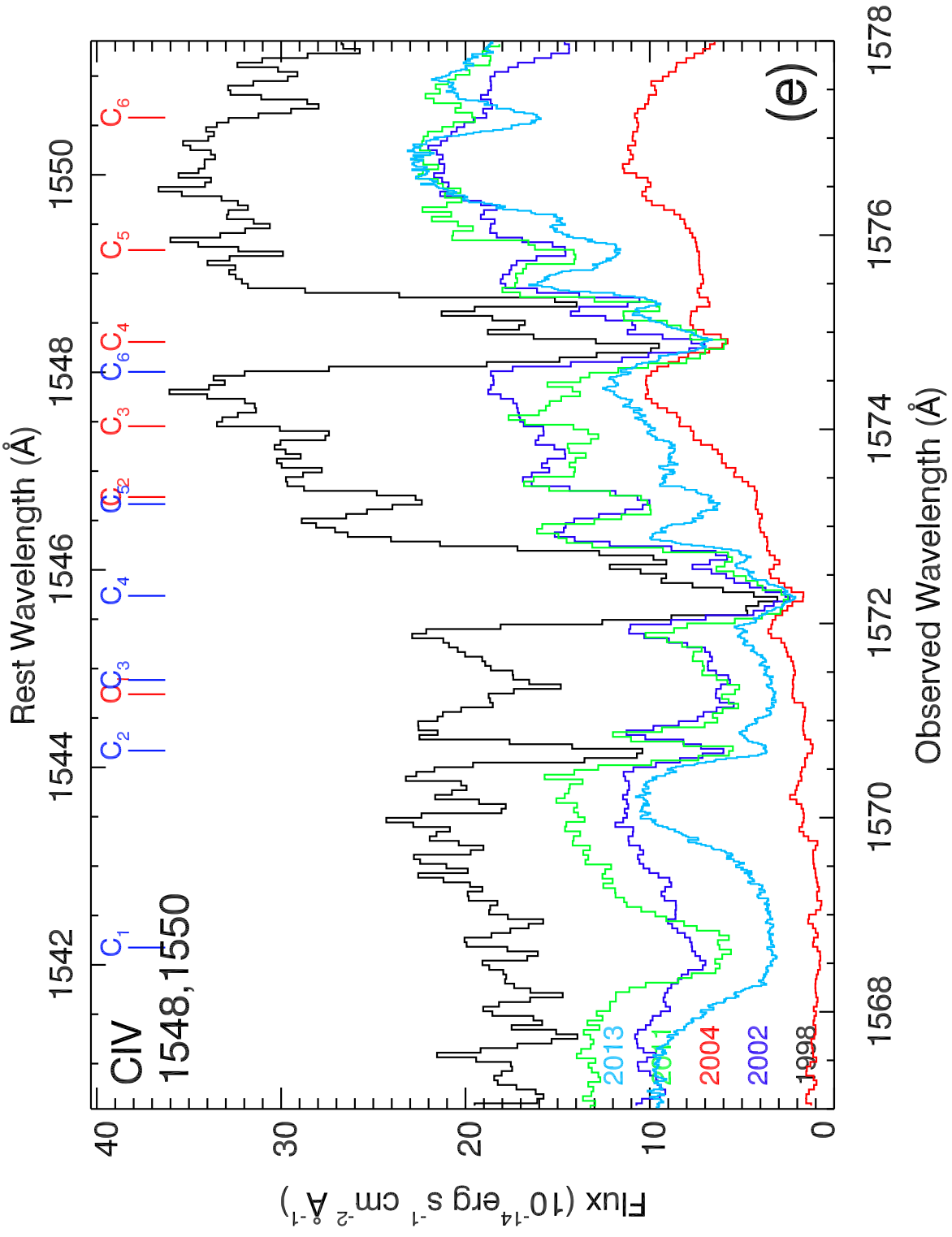

Figure A.2: *continued*

Figure A.3: A plot of the normalized spectrum of NGC 5548 during the five epochs of observation, plotted in the velocity rest-frame of the quasar (same annotation as Figure A.2).

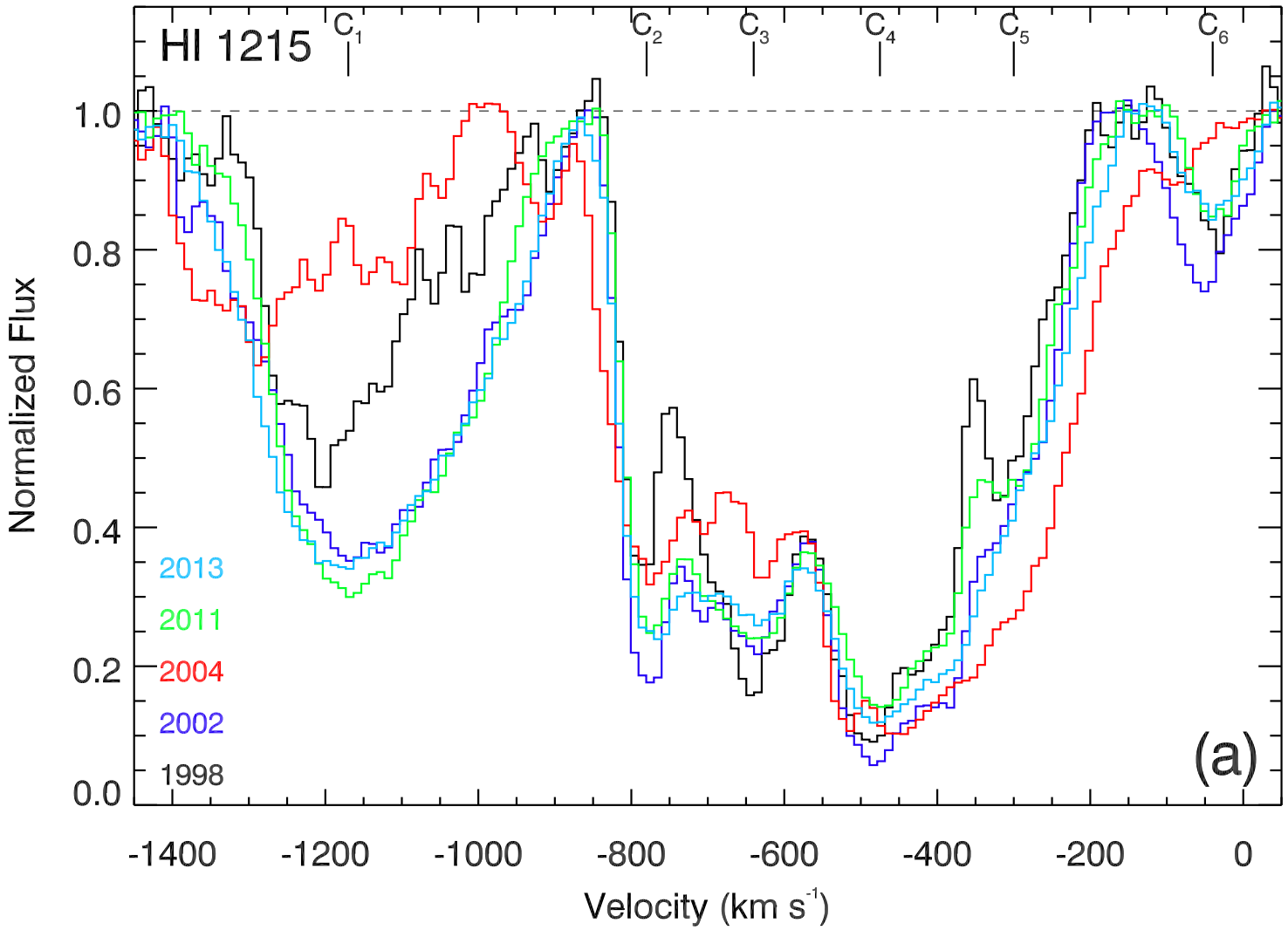

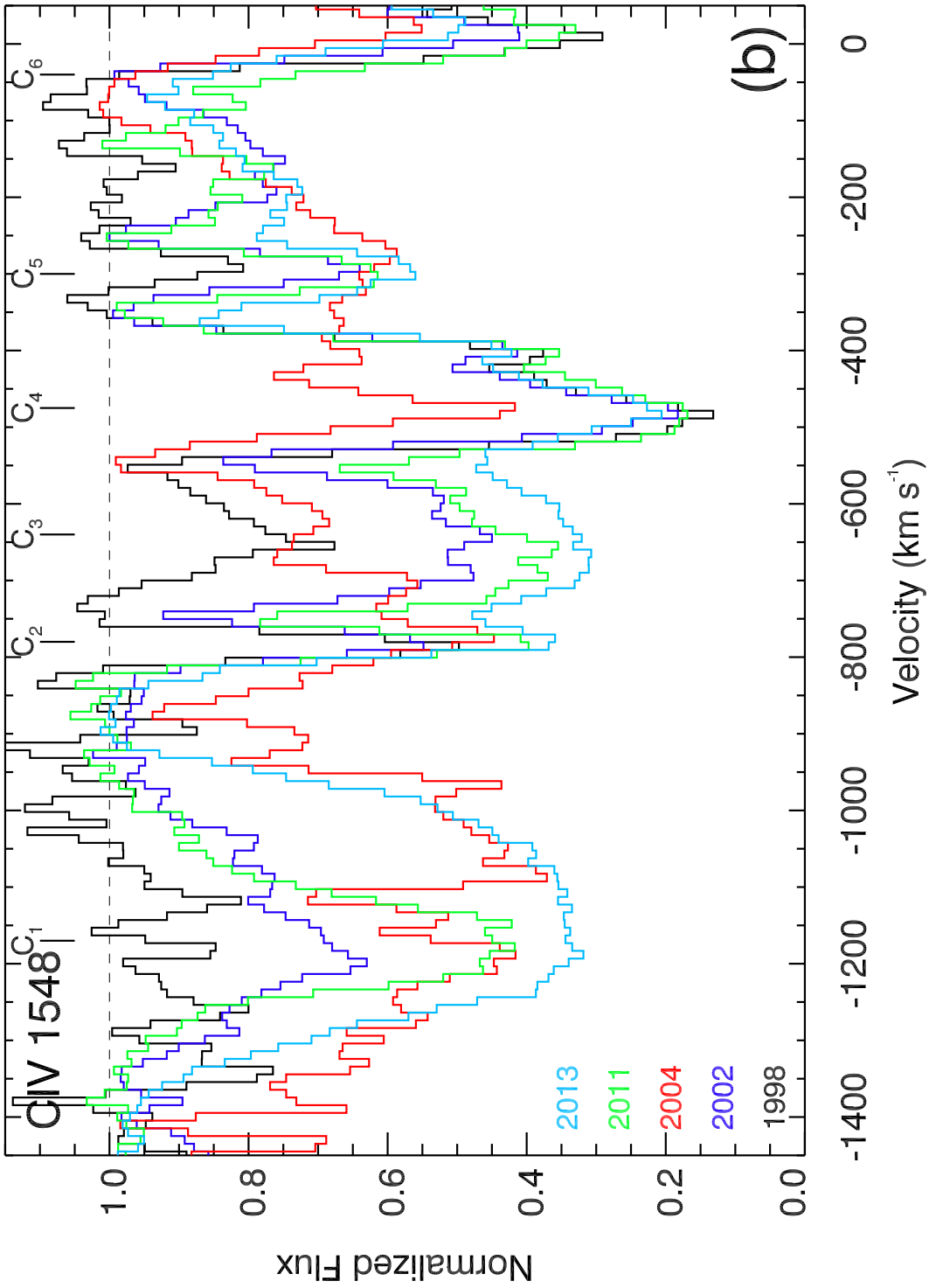

Figure A.3: *continued*

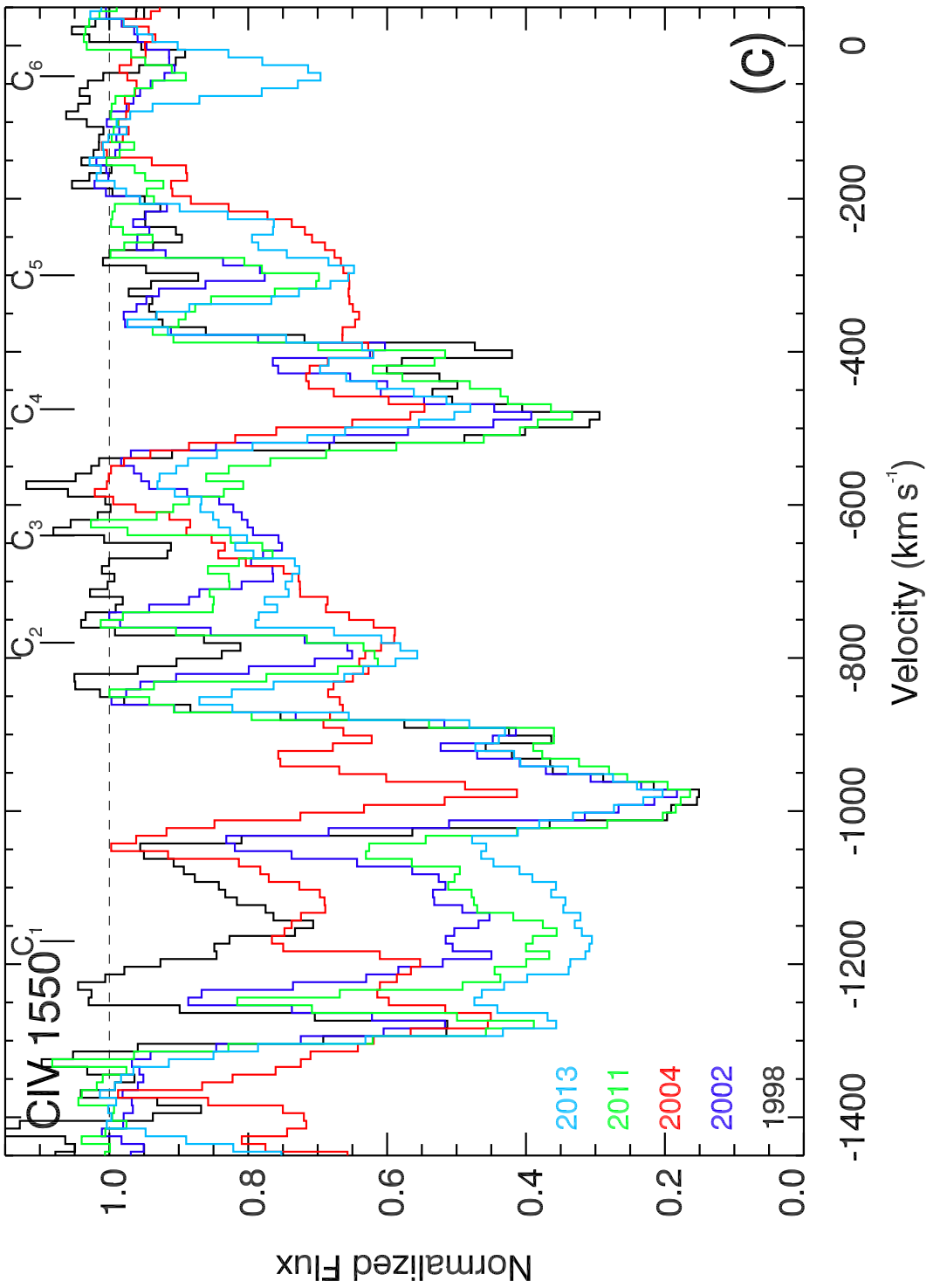

Figure A.3: *continued*

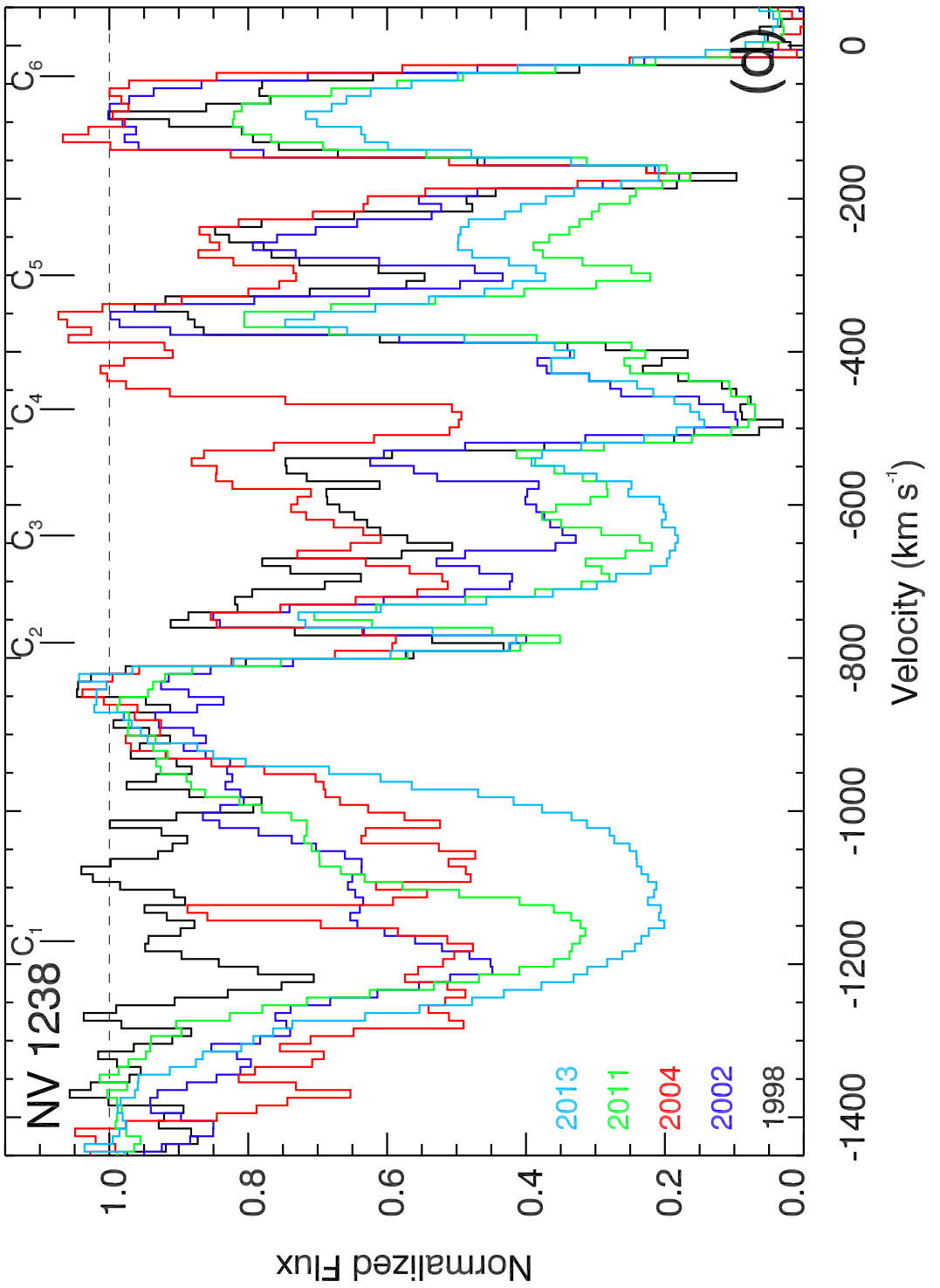

Figure A.3: *continued*

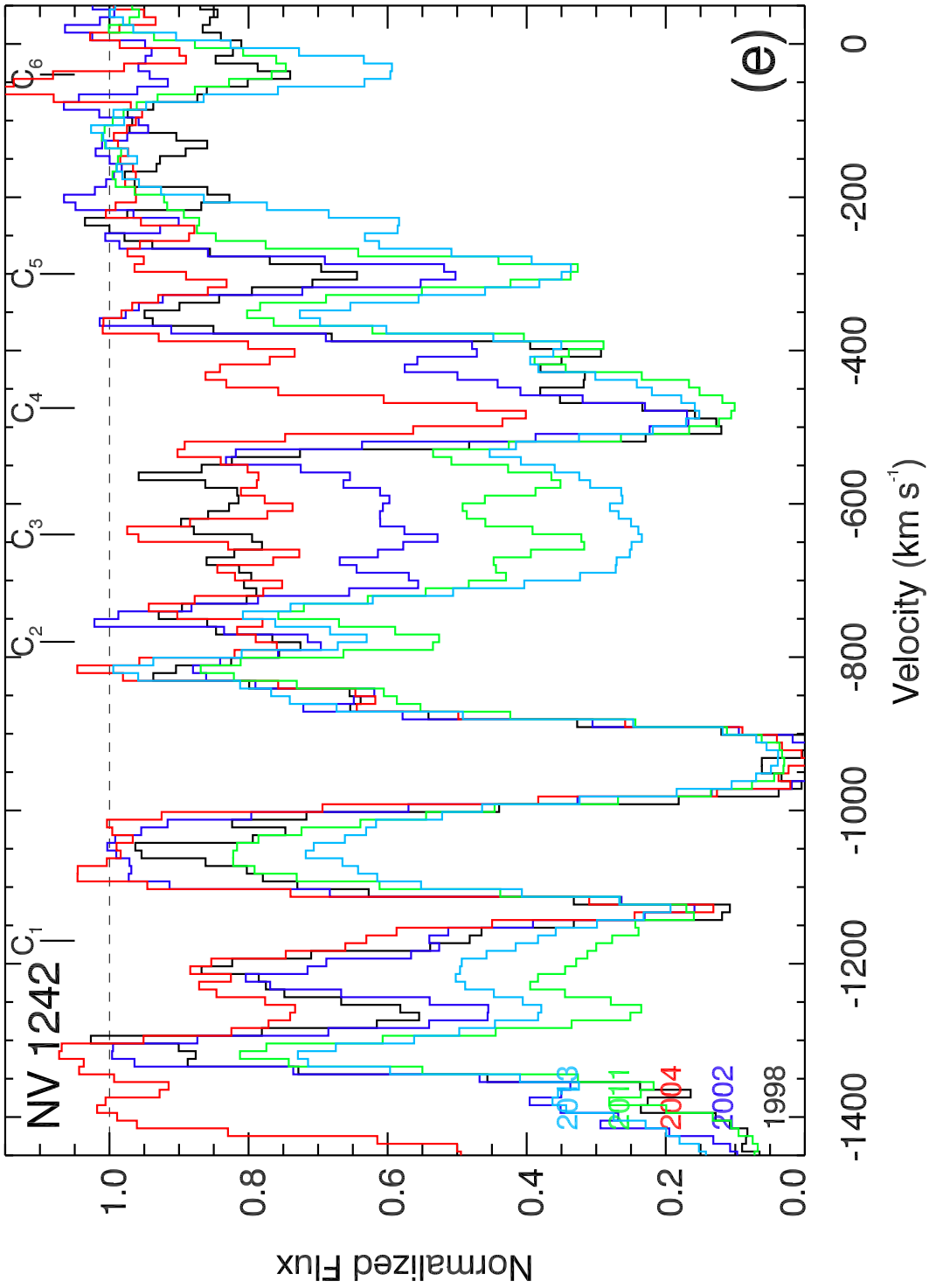

Figure A.3: *continued*

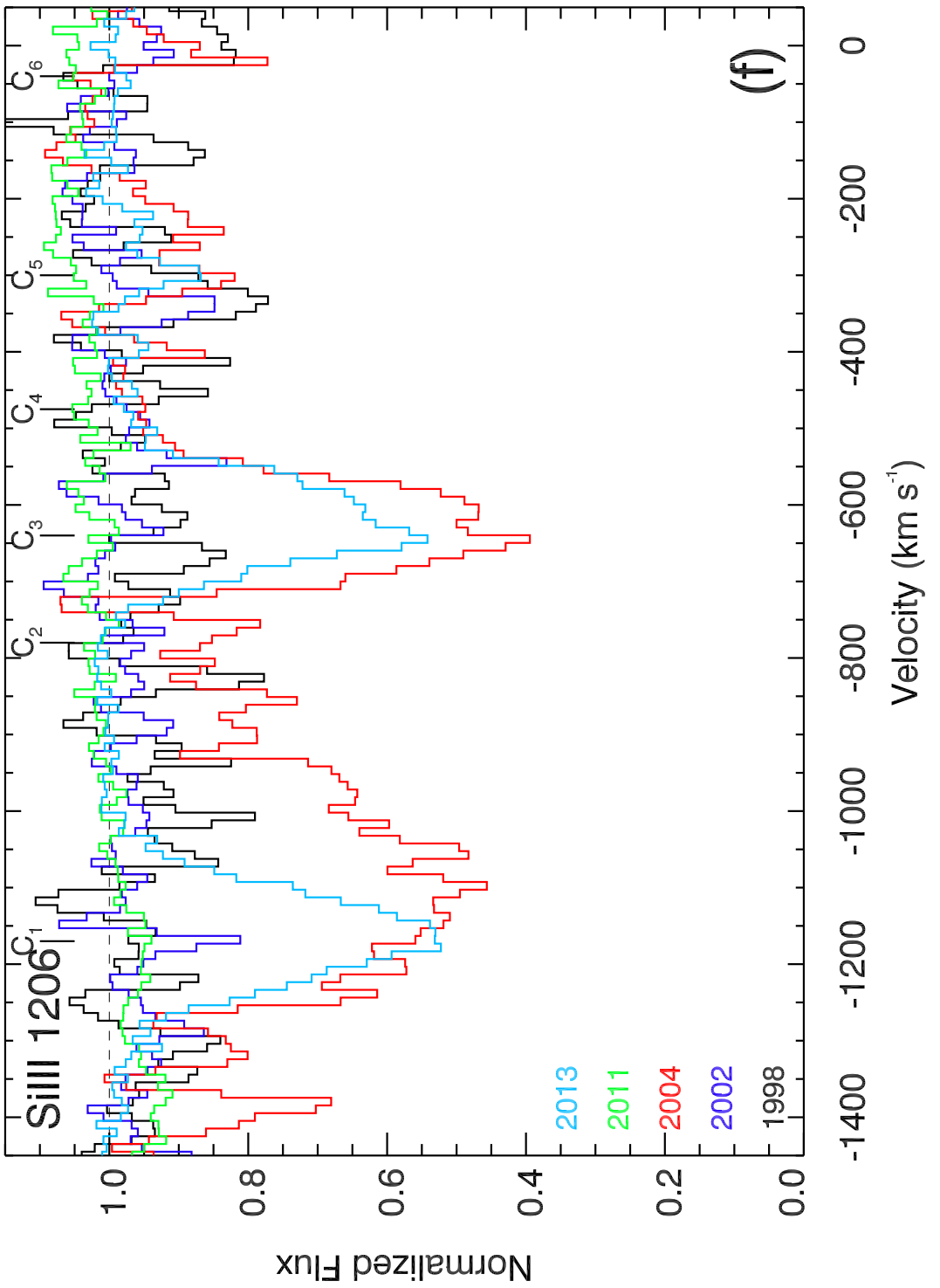

Figure A.3: *continued*

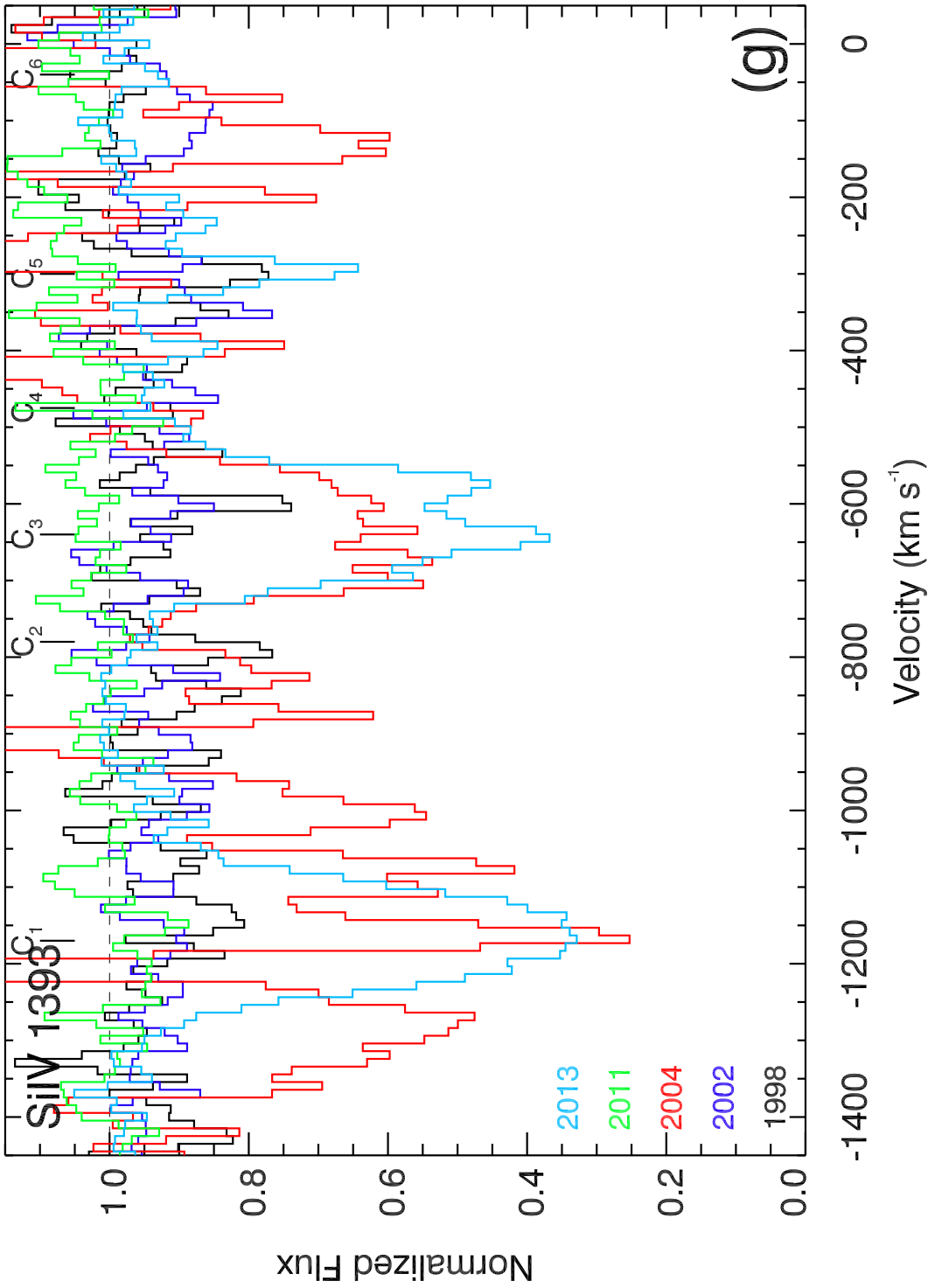

Figure A.3: *continued*

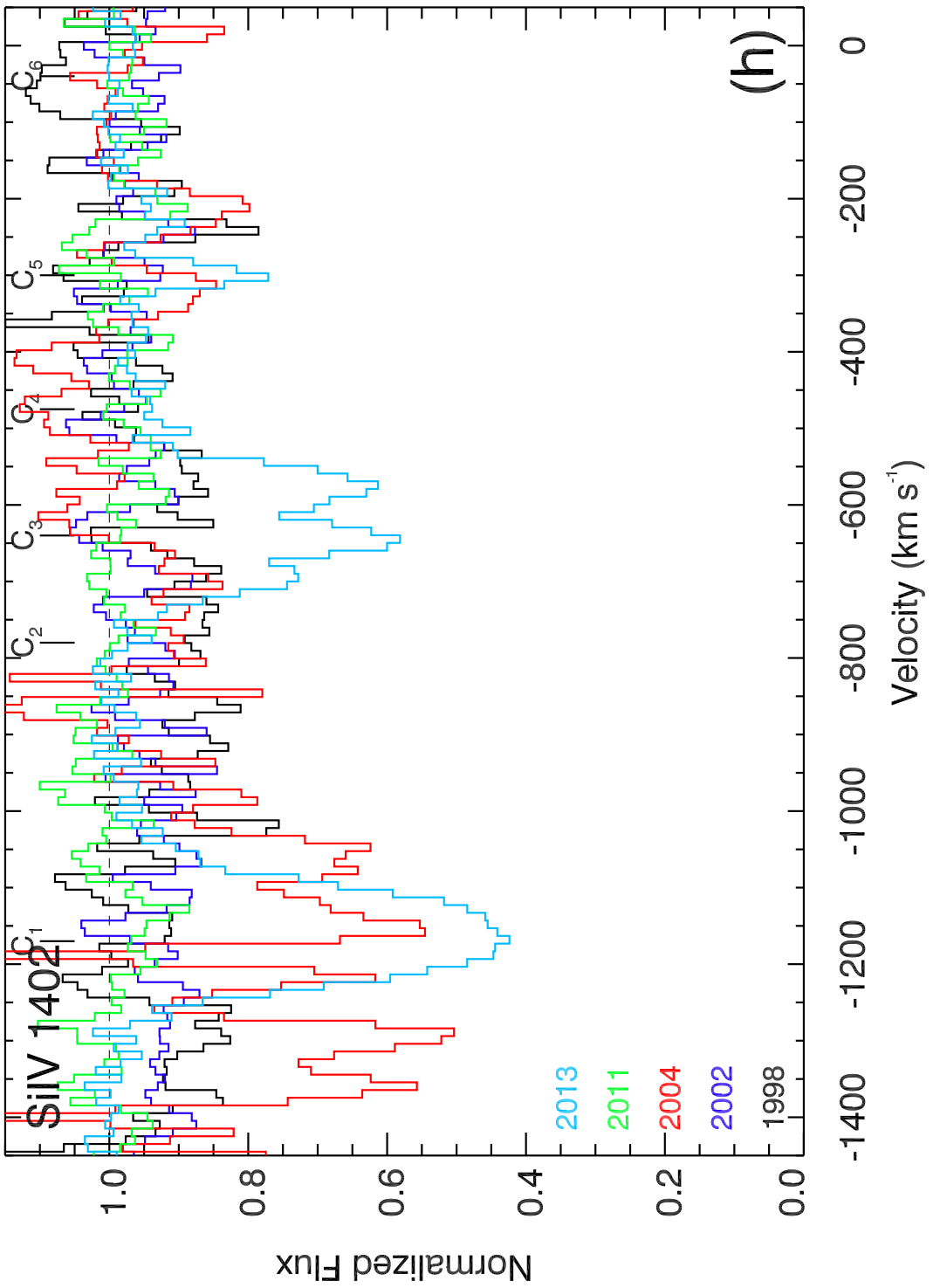

Figure A.3: *continued*